KU LEUVEN

ARENBERG DOCTORAL SCHOOL
Faculty of Science

Deformation and mixing of co-existing shapes in the neutron-deficient polonium isotopes

Nele Kesteloot

Supervisor:
Prof. dr. P. Van Duppen
Prof. dr. M. Huyse, co-supervisor

Dissertation presented in partial
fulfillment of the requirements for the
degree of Doctor in Science

March 2015

Deformation and mixing of co-existing shapes in the neutron-deficient polonium isotopes

Nele KESTELOOT

Examination committee:
Prof. dr. C. Van Haesendonck, chair
Prof. dr. P. Van Duppen, supervisor
Prof. dr. M. Huyse, co-supervisor
Prof. dr. G. Neyens
Prof. dr. N. Severijns

Prof. dr. K. Heyde
(Universiteit Gent)
dr. B. Bastin
(GANIL, Caen, France)
dr. L. Popescu
(SCK•CEN, Mol)

Dissertation presented in partial
fulfillment of the requirements for
the degree of Doctor
in Science

March 2015

Uitgegeven in eigen beheer, Nele Kesteloot, Celestijnenlaan 200D bus 2418, B-3001 Heverlee (Belgium)

Dit werk kwam mede tot stand met steun van het

Fonds voor Wetenschappelijk Onderzoek (FWO) Vlaanderen

&

Studiecentrum voor Kernenergie - Centre d'Étude de l'Énergie Nucléaire
(SCK•CEN, Mol)

Dankwoord

Mijn eerste woorden van dank gaan naar mijn promotors Mark en Piet. Bedankt om me de kans te geven om vier jaar onderzoek te doen in de spectroscopiegroep en om mee te draaien in het internationale onderzoek. Van jullie heb ik ongelofelijk veel geleerd. Bedankt ook voor de aangename sfeer en de interesse, niet alleen voor fysica, maar ook voor de andere belangrijke dingen in het leven!

A special thank you goes to the members of the examination committee; Beyhan, Gerda, Lucia, Nathal, Prof. dr. Chris Van Haesendonck and Prof. dr. Kris Heyde. Thank you for the careful revision and evaluation of my manuscript and the inspiring discussions during the preliminary defense.

This work would not have been possible without two post docs in the Coulex field; Kasia and Liam. It was an honour for me to share the office with you. You helped me through all the phases of my PhD work: doing experiments together at ISOLDE, looking at spectra and writing all kinds of codes together and last but definitely not least our endless GOSIA discussions. I could not have dreamed of a better team *café Coulex* and I truely hope we will stay in contact, even though we will be scattered troughout Europe.

Mezelf goed voelen op het werk en graag komen werken waren cruciaal om dit werk tot een goed einde te brengen. Jan en Nick, bedankt voor het warme welkom op het IKS, al vanaf het maken van mijn masterthesis. Het zal moeilijk zijn om ooit collega's te vinden die het aantal grappen en grollen per minuut tijdens een gemiddelde werkdag dat jullie behaalden, te evenaren. Bedankt Céline, Jytte, Lars en Simon voor de kaartmiddagen, babbelpauzes en spelletjesavonden. Dat er nog veel gezellige momenten mogen volgen!

Thank you to all members of IKS, especially to the spectroscopy group, for the nice atmosphere. Isabelle, Sally, Martine, Fabienne en Danielle, bedankt voor de hulp bij alle praktische zaken die ik moest regelen. Ook een woord van dank aan Luc en Bert om steeds paraat te staan voor eerste hulp bij ICT problemen.

Dan wil ik ook mijn vrienden buiten het werk bedanken om te zorgen voor ontspanning en een uitlaatklep als ik het nodig had. Bedankt aan de fysicavrienden, vriendinnen van het Spijker, al de Amuse vrienden en natuurlijk de vriendinnen van de Plussers. Jullie zijn met te veel om bij naam te noemen maar ik hoop dat onze vriendschappen stuk voor stuk blijven bestaan.

Bedankt aan mijn familie en schoonfamilie, voor de altijddurende steun en interesse voor de onbekende kernfysicawereld. Mama en papa, oneindig hard bedankt! Bedankt om me de kans te geven om te studeren, om me de exact-wetenschappelijke genen door te geven en voor de onvoorwaardelijke liefde.

Bedankt Stijn voor de ontelbare kleine dingen van elke dag, om er altijd voor me te zijn en vooral om achter me te staan en me te steunen in alles wat ik doe. Samen zijn we het beste team!

Dank je, lieve kleine zoon. Ik ken je nog niet maar deze tekst hebben we wel samen geschreven. Ik hoop dat je later ook iets vindt waar je met zoveel passie aan kan werken en daar zal ik je onvoorwaardelijk in steunen.

Nele

Preface

This thesis describes two Coulomb-excitation campaigns with neutron-deficient ^{196,198,200,202}Po beams that were performed at the REX-ISOLDE facility in CERN. The aim of these experiments was to characterize the deformation and mixing of co-existing shapes in the studied isotopes. Chapter 1 provides an introduction to the nuclear many-body problem and to deformation of nuclei and motivates why the neutron-deficient polonium isotopes are interesting to study. The technique of Coulomb excitation is introduced in Chapter 2 and in Chapter 3, experimental details related to the setup and data analysis are given. Chapter 4 is the main chapter of this thesis that starts with the full version of the detailed paper in which the results of this thesis will be published:

N. Kesteloot, B. Bastin, K. Auranen, C. Bauer, M. Bender, V. Bildstein, A. Blazhev, S. Bönig, N. Bree, E. Clément, T.E. Cocolios, A. Damyanova, I. Darby, H. De Witte, D. Di Julio, J. Diriken, C. Fransen, L.P. Gaffney, J.E. García-Ramos, R. Gernhäuser, T. Grahn, P.-H. Heenen, H. Hess, K. Heyde, M. Huyse, J. Iwanicki, U. Jakobsson, J. Konki, T. Kröll, B. Laurent, N. Lecesne, R. Lutter, J. Pakarinen, P. Peura, E. Piselli, L. Próchniak, P. Rahkila, E. Rapisarda, P. Reiter, M. Scheck, M. Seidlitz, M. Sferrazza, B. Siebeck, M. Sjodin, H. Tornqvist, E. Traykov, J. Van De Walle, P. Van Duppen, M. Vermeulen, D. Voulot, N. Warr, F. Wenander, K. Wimmer, K. Wrzosek-Lipska, and M. Zielińska.
Deformation and mixing of co-existing shapes in neutron-deficient polonium isotopes
Physical Review C (2015)

Next to that, Chapter 4 provides more details related to the data analysis and the analysis using the Coulomb-excitation analysis code GOSIA. In Chapter 5, the extracted results are summarized and three different nuclear models and a phenomenological two-state mixing model used to compare to the data. Finally, Chapter 6 concludes on the results that were achieved in this thesis and provides an outlook into the future.

Summary

The neutron-deficient polonium isotopes, with only 2 protons outside the $Z = 82$ shell closure, are situated in an interesting region of the nuclear chart. In the neighboring lead ($Z = 82$) and mercury ($Z = 80$) isotopes, experimental and theoretical efforts identified evidence of shape coexistence. Shape coexistence is the remarkable phenomenon in which two or more distinct types of deformation occur in states of the same angular momentum and similar excitation energy in a nucleus. The neutron-deficient polonium isotopes have also been studied intensively, experimentally as well as theoretically. The closed neutron-shell nucleus ^{210}Po ($N = 126$) manifests itself as a two-particle nucleus where most of the excited states can be explained by considering the degrees of freedom of the two valence protons outside of ^{208}Pb. The near-constant behavior of the yrast 2^+_1 and 4^+_1 states in the isotopes with mass $200 \leq A \leq 208$ can be explained by coupling the two valence protons to a vibrating lead core. ^{200}Po seems to mark the end of this regular seniority-based character, with a sudden downsloping trend of almost all the excited states in the lighter isotopes with mass $A < 200$. The observed characteristics in the lightest polonium isotopes have been interpreted as evidence for an interplay between intruder structures and the regular structure.

The transitional region between the regular seniority-based behavior in the heavier polonium isotopes and the shape coexistence regime in the lighter isotopes is studied in this thesis with the technique of Coulomb excitation. This powerful technique allows to extract information about the deformation and mixing of co-existing shapes in a model-independent way. Recently, the Coulomb-excitation study of $^{182-188}$Hg led to the interpretation of mixing between a weakly-deformed oblate-like band and a more-deformed prolate-like band.

A reaction is classified as Coulomb excitation when the collision between an incident projectile beam and a target nucleus leads to the excitation of one of the collision partners. At beam energies below the so-called “safe value”, the reaction is purely electromagnetic. Semi-classical perturbation theory can then be applied to describe the Coulomb-excitation process. The cross section for Coulomb excitation is related to the reduced electric quadrupole matrix elements coupling the populated states in the excited nucleus.

Two Coulomb-excitation experimental campaigns with neutron-deficient ^{196,198,200,202}Po beams were performed at the REX-ISOLDE facility in CERN (Geneva, Switzerland). Beams were produced and post-accelerated to an energy of 2.85 MeV per nucleon and made to collide with a ^{104}Pd and a ^{94}Mo target, both of 2.0 mg/cm^2 thickness. A double-sided silicon-strip detector was placed inside the collision chamber to detect the scattered particles. Surrounding the target chamber was a position-sensitive germanium detector array to detect the de-excitation γ rays.

Conditions related to timing and kinematic properties were applied to distinguish the Coulomb-excitation events from the background events. The background-subtracted and Doppler-corrected γ-ray spectra showed that the 2_1^+ state was populated in all isotopes. Furthermore, in ^{196,198}Po multi-step Coulomb excitation was observed and populated the 4_1^+, 0_2^+ and 2_2^+ states. The relatively large uncertainties on the de-excitation yields of the 0_2^+ and 2_2^+ states are due to the indirect observation of the $E0$ transitions through characteristic polonium X rays. For future experiments, a direct way of observing $E0$ transitions by the electron spectrometer SPEDE is discussed.

The extracted results have been interpreted in the framework of three different nuclear models: the beyond-mean-field model, the interacting-boson model and the general Bohr Hamiltonian model. Next to that, a deformation parameter that can be extracted from the Coulomb-excitation results was compared to a deformation parameter, deduced from charge radii measurements. Finally, a phenomenological two-state mixing model was applied and hinted towards the spin-independent mixing of a spherical with a more deformed structure. Overall, the comparison to theory could benefit from improved uncertainty of the experimental data. This could be achieved with the higher-energy beams that will be available at the HIE-ISOLDE facility.

Nederlandstalige samenvatting

De neutronarme poloniumisotopen, met 2 protonen buiten de $Z = 82$ schilsluiting, bevinden zich in een interessant gebied van de kernkaart. In de naburige lood- ($Z = 82$) en kwikisotopen ($Z = 80$), hebben resultaten van experimenteel en theoretisch onderzoek geleid tot het waarnemen van vormcoëxistentie. Vormcoëxistentie is het opmerkelijke fenomeen waarbij twee of meer toestanden van dezelfde spin en vergelijkbare excitatie-energie voorkomen met een verschillend intrinsiek vervormingstype. De neutronarme poloniumkernen zijn ook uitvoerig bestudeerd, zowel op experimenteel als theoretisch gebied. De kern ^{210}Po, met een gesloten neutronschil ($N = 126$), vormt een schoolvoorbeeld van een kern waarin de geëxciteerde toestanden kunnen verklaard worden door de vrijheidsgraden van de twee valentieprotonen, buiten ^{208}Pb, in rekening te brengen. De bijna constante energie van de 2_1^+ en 4_1^+ toestanden in de isotopen met massa $200 \leq A \leq 208$ kan verklaard worden door deze twee valentieprotonen te combineren met een vibrerende loodkern. ^{200}Po lijkt de laatste kern te zijn met deze senioriteitskenmerken, vermits een plotse daling van de excitatie-energie is waargenomen voor bijna alle geëxciteerde toestanden in de isotopen met massa $A < 200$. De waargenomen eigenschappen van de lichtste poloniumisotopen worden geïnterpreteerd als bewijs voor een wisselwerking tussen indringstructuren en de normale structuur.

De overgangsregio tussen het normale, senioriteitskarakter voor de zwaardere poloniumisotopen en het regime met kenmerken van vormcoëxistentie in de lichtere isotopen wordt in deze thesis bestudeerd met de techniek van Coulombexcitatie. Met deze krachtige techniek kan, op een modelonafhankelijke manier, informatie over de vervorming en de menging tussen verschillende vormen worden verkregen. Recent nog leidde een Coulombexcitatie-experiment van de neutronarme $^{182-188}$Hg isotopen tot de vaststelling dat een oblaatachtige band met kleine vervorming en een sterker vervormde prolaatachtige band mengen in deze isotopen.

Men spreekt van Coulombexcitatie als de botsing tussen een projectiel- en een trefschijfkern ervoor zorgt dat één van deze twee kernen geëxciteerd wordt. Wanneer deze reactie gebeurt bij bundelenergieën onder de zogenaamde “veilige waarde”, dan is de reactie volledig elektromagnetisch en kan semiklassieke perturbatietheorie toegepast worden om het Coulombexcitatieprocess te beschrijven. De botsingsdoorsnede van Coulombexcitatie is afhankelijk van de gereduceerde $E2$ matrixelementen die die bevolkte toestanden verbinden.

Twee Coulombexcitatiecampagnes werden uitgevoerd aan de REX-ISOLDE faciliteit in CERN (Genève, Zwitserland) met neutronarme ^{196,198,200,202}Po bundels. De bundels werden geproduceerd en naversneld tot een energie van 2.85 MeV per nucleon en botsten met een ^{104}Pd en een ^{94}Mo trefschijf, beiden 2.0 mg/cm^2 dik. Binnenin de botsingskamer bevond zich een dubbelzijdige siliciumstrip detector om de verstrooide deeltjes te detecteren. De botsingskamer werd omringd door een positiegevoelige germaniumdetector die diende voor de waarneming van de uitgestuurde γ-stralen.

Een onderscheid tussen de Coulombexcitatiegebeurtenissen en de achtergrondgebeurtenissen werd gemaakt door voorwaarden te stellen voor de kinematische en tijdskarakteristieke eigenschappen van de geregistreerde gebeurtenissen. De energiespectra van de γ-stralen, die werden gecorrigeerd voor het Dopplereffect en waarvan de achtergrond werd afgetrokken, toonden dat de 2^+_1-toestand in alle isotopen bevolkt werd. In de experimenten met ^{196,198}Po werden ook de 4^+_1, 0^+_2 en 2^+_2 toestanden bevolkt in een meerstapsproces. De relatief grote onzekerheid op de intensiteit van de deëxcitatie van de 0^+_2 en de 2^+_2 toestand is te wijten aan de onrechtstreekse manier waarop $E0$-overgangen werden waargenomen, via karakteristieke polonium X-stralen. Voor experimenten in de toekomst kan de electrondetector SPEDE een oplossing bieden om $E0$-overgangen rechtstreeks waar te nemen.

De resultaten die bekomen werden in deze thesis, werden geïnterpreteerd in het kader van drie verschillende theoretische kernmodellen: het *beyond-mean-field* model, het *interacting-boson* model en het *general Bohr Hamiltonian* model. Daarnaast werd een vervormingsparameter bepaald op basis van de resultaten van de Coulombexcitatie-experimenten en vergeleken met een vervormingsparameter die verkregen werd uit de meting van ladingsstralen van de poloniumisotopen. Tot slot werd een fenomenologisch twee-niveau-mengingsmodel gebruikt dat leidde tot de interpretatie van een sferische structuur die mengt met een meer vervormde structuur. Over het algemeen zou de vergelijkende studie van de resultaten met de theoretische modellen meer informatie kunnen opleveren als de experimentele resultaten een kleinere onzekerheid hadden. Deze betere precisie zou kunnen bereikt worden met de bundels van hogere energie die geproduceerd zullen worden aan de HIE-ISOLDE faciliteit.

Contents

1 Introduction

The atomic nucleus is a strongly interacting quantum system of A nucleons. As a consequence, the nucleus can appear in a variety of shapes. This thesis aims to quantify the deformation and mixing of co-existing configurations in the neutron-deficient polonium isotopes, using the technique of Coulomb excitation. This chapter introduces the nuclear many-body problem and nuclear deformation. The theory presented here is largely based on the textbooks by Rowe and Wood [1], Casten [2] and Heyde [3], to which the reader is referred for more details. In the final section, an overview of the state-of-the-art experimental and theoretical information on the neutron-deficient polonium isotopes is given.

1.1 The nuclear many-body problem

The wave functions of the nuclear states of a nucleus can be obtained by solving the many-body Schrödinger equation

$$H\Psi = E\Psi \tag{1.1}$$

where the Hamiltonian H is given by a sum over the kinetic-energy terms $\sum\limits_{i=1}^{A} \frac{p_i^2}{2m_i}$ and the nucleon-nucleon two-body interactions of all nucleons in the nucleus $\sum\limits_{i<j=1}^{A} V(i,j)$. In the most general case, this proves to be a formidable task.

For very light nuclei ($A < 12$), one can start from modern descriptions of the nucleon-nucleon interaction (two-body and even higher-order terms, which are derived from nucleon-nucleon scattering data), using an ab-initio approach [4–6]. For heavier nuclei (beyond ^{12}C), one approximates the general A-body problem (basing on experimental evidence) into A one-body problems that describe the motion of individual nucleons in an average potential

$$H_0 = \sum_{i=1}^{A} \left(\frac{\overrightarrow{p_i}^2}{2m_i} + U(\overrightarrow{r_i}) \right) \tag{1.2}$$

and a remaining part describing the residual interaction

$$H_1 = \sum_{i<j=1}^{A} V(i,j) - \sum_{i=1}^{A} U(\overrightarrow{r_i}). \tag{1.3}$$

The average potential can be derived using self-consistent Hartree-Fock (HF) methods or the Hartree-Fock-Bogoliubov (HFB) approach, when also including the pairing correlations amongst the nucleons. The Schrödinger equation $H\Psi = E\Psi$ ($H = H_0 + H_1$) can then be solved, within a basis defined by the independent particle motion, described by the solutions of the one-body problems:

$$h_0 \psi_i(\overrightarrow{r_i}, \overrightarrow{\sigma_i}) = \varepsilon_i \psi_i(\overrightarrow{r_i}, \overrightarrow{\sigma_i}) \tag{1.4}$$

with ε_i the single-particle energies. Thus,

$$H_0 \mathcal{A} \prod_{i=1}^{A} \psi_i(\overrightarrow{r_i}, \overrightarrow{\sigma_i}) = E_0 \mathcal{A} \prod_{i=1}^{A} \psi_i(\overrightarrow{r_i}, \overrightarrow{\sigma_i}) \tag{1.5}$$

with $E_0 = \sum_{i=1}^{A} \varepsilon_i$ the corresponding energy eigenvalue and $\mathcal{A}$ the antisymmetrization operator leading to a Slater determinant. This can be the starting point to treat the residual interaction H_1 and solve the corresponding Schrödinger equation in the basis $\Phi(1, 2, ...A) = \mathcal{A} \prod_{i=1}^{A} \psi_i(\overrightarrow{r_i}, \overrightarrow{\sigma_i})$.

1.2 Nuclear deformation

Using the spherical shell model as a starting point, one can describe many nuclear properties, based on the characteristics of the two-body nucleon-nucleon interaction and its single-particle energies. The nuclear shell model by now has shown that collective properties can result from its calculations (see e.g. detailed large-scale shell-model studies in the sd and fp shell [7, 8]). Such excitations have been described before, starting from a collective description of the atomic nucleus, considering the nucleus as a charged, liquid drop and studying its dynamics [1, 9, 10]. The nucleus can then exhibit various excitation modes: vibrational motion around a spherical shape, rotational motion of a deformed nucleus and more complex collective modes (e.g. anharmonicities, coupling between modes,...). Here, we give a concise description of the harmonic vibrator model in section 1.2.2 and the rigid rotor model of a deformed nucleus in section 1.2.3. Using the concept of a deformed shape, one can introduce the idea of independent particles moving in a deformed potential, which, if taken as a deformed harmonic oscillator, is known as the Nilsson model [11]. This gives rise to possibilities to describe nuclear collective properties, starting from a microscopic basis.

The nuclear surface $R(\theta, \phi)$ can be expanded in terms of a set of multipole λ deformation coordinates $\alpha_{\lambda\mu}$:

$$R(\theta,\phi) = R_0 \left(1 + \sum_{\lambda\mu} \alpha^*_{\lambda\mu} Y_{\lambda\mu}(\theta,\phi) \right) \tag{1.6}$$

where R_0 is the radius of a spherical nucleus with the same volume, λ represents the multipole order and $Y_{\lambda\mu}(\theta,\phi)$ are the spherical harmonics. In this thesis, only quadrupole degrees of freedom $\lambda = 2$ will be considered which means that the Hamiltonian is written and solved in a five-dimensional configuration space, spanned by the quadrupole deformation coordinates $\alpha_{2\mu}$ where $\mu = -2, -1, 0, 1, 2$.

The five quadrupole deformation coordinates $\alpha_{2\mu}$ can alternatively be written in terms of the three Euler angles and two intrinsic coordinates β_2 and γ that are defined as (with $\alpha_{21} = \alpha_{2-1} = 0$):

$$\begin{cases} \alpha_{20} = \beta_2 \cos\gamma \\ \alpha_{22} = \alpha_{2-2} = \frac{1}{\sqrt{2}}\beta_2 \sin\gamma. \end{cases} \tag{1.7}$$

The variable β_2 expresses a measure of the quadrupole deformation and is limited to positive values (including 0) while γ represents the degree of axial symmetry. To avoid multiple equivalent descriptions of one shape, γ is limited as well: $0 \leq \gamma \leq \frac{\pi}{3}$. Both variables are illustrated geometrically on Figure 1.1. The following limits of the intrinsic variables define known shapes of an ellipsoid:

- $\beta_2 = 0$: spherical shape
- $\beta_2 > 0, \gamma = 0$: prolate deformation
- $\beta_2 > 0, \gamma = \pi/3$: oblate deformation
- $\beta_2 > 0, 0 < \gamma < \pi/3$: triaxial shape.

A triaxial shape is characterized by an unequal length of the three axes, compared to the cases with axial symmetry where always two of the three axes are equal.

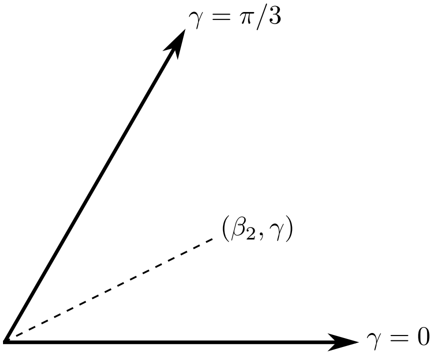

Figure 1.1: Geometric representation of the intrinsic deformation variables β_2 and γ, as defined in the text.

1.2.1 Experimental observables

The deformation and degree of collectivity of a nucleus can be probed through various experimental techniques (e.g. scattering, Coulomb excitation, lifetime measurements, ...). This section introduces the main observables that will appear in this thesis.

The reduced transition probability of multipole order $E\lambda$ (electric λ pole) or $M\lambda$ (magnetic λ pole) offers a quantitative measure of the transition strength and is evaluated from

$$B(\lambda; I_i \to I_f) = \frac{1}{2I_i + 1} \left| \langle I_f || \hat{O}(\lambda) || I_i \rangle \right|^2 \tag{1.8}$$

where I refers to the angular momentum of the state and the Wigner-Eckart theorem is used to define the reduced matrix element

$$\langle I_f M_f | \hat{O}(\lambda, \mu) | I_i M_i \rangle = (-1)^{I_f - M_f} \begin{pmatrix} I_f & \lambda & I_i \\ -M_f & \mu & M_i \end{pmatrix} \langle I_f || \hat{O}(\lambda) || I_i \rangle \tag{1.9}$$

and where $\hat{O}(\lambda)$ is the λ-pole operator. Reduced transition probabilities are frequently expressed in Weisskopf units (W.u.), which express the single-particle estimate for the transition rate. The Weisskopf units for electric and magnetic transitions are given, respectively, by

$$B(E\lambda)_{\text{W.u.}} = \frac{e^2}{4\pi} \left(\frac{3}{\lambda + 3} \right)^2 R^{2\lambda} \tag{1.10}$$

and

$$B(M\lambda)_{\text{W.u.}} = \frac{10}{\pi} \left(\frac{e\hbar}{2mc} \right)^2 \left(\frac{3}{\lambda + 3} \right)^2 R^{2\lambda - 2} \tag{1.11}$$

with $R = r_0 A^{1/3}$ the nuclear radius with $r_0 = 1.2\,\mathrm{fm}$. The reduced transition probability that will be used most frequently in this thesis, is the $B(E2)$ value, for which the Weisskopf unit is

$$B(E2)_{\mathrm{W.u.}} = 5.940 \times 10^{-6} A^{4/3} e^2 b^2. \tag{1.12}$$

$B(E2)$ values close to unity in W.u. point to single-particle behavior while transitions in collective nuclei can have large $B(E2)$ values in Weisskopf units.

The electric quadrupole moment gives a good measure of the deviation from spherical symmetry. For an axially symmetric charge distribution with angular momentum I, the quadrupole moment is defined as

$$Q(IM) = \int \rho^{(e)}_{IM}(\mathbf{r}) \left(3z^2 - r^2\right) d\mathbf{r} \tag{1.13}$$

where $\rho^{(e)}_{IM}(\mathbf{r})$ describes the nuclear charge distribution [12]. Alternatively, the quadrupole moment can be written in a spherical tensor basis:

$$Q(IM) = \sqrt{\frac{16\pi}{5}} \sum_{i=1}^{A} e(i) \langle IM | r^2(i) Y_{20}(\hat{\mathbf{r}}(i)) | IM \rangle. \tag{1.14}$$

The expectation value in equation 1.14 depends on the projection quantum number M of the angular momentum. The *spectroscopic* quadrupole moment Q_s, which is observed in experiments, is defined as the expectation value in the state $M = I$ [12]:

$$Q_s \equiv Q(I, M = I) = \sqrt{\frac{I(2I-1)}{(2I+1)(2I+3)(I+1)}} \sqrt{\frac{16\pi}{5}} \langle I || \hat{O}(E2) || I \rangle. \tag{1.15}$$

which is deduced by applying the Wigner-Eckart theorem of equation 1.9. The spectroscopic quadrupole moment is thus proportional to the reduced diagonal $E2$ matrix element $\langle I || \hat{O}(E2) || I \rangle$, which can be extracted from Coulomb-excitation experiments (see later in this thesis, section 2.1.4). From equation 1.15, it is clear that the spectroscopic quadrupole moment of a nuclear state with spin $I = 0$ or $I = 1/2$ vanishes. Although a state with spin $I = 0$ or $I = 1/2$ can possess an intrinsic deformation, this deformation can not be extracted from measurements of the quadrupole moment Q_s.

Consider the axially symmetric charge distribution in Figure 1.2, of which the symmetry axis z' makes an angle β with the laboratory z axis. The spectroscopic quadrupole moment, defined in the laboratory system, can then be related to an *intrinsic* quadrupole moment Q_0, defined with respect to the symmetry axis of the charge distribution:

$$Q_s = \frac{1}{2}\left[3\cos^2\beta - 1\right] \int \rho^{(e)}_{IM}(\mathbf{r'}) \left(3z'^2 - r^2\right) d\mathbf{r'} = \frac{1}{2}\left[3\cos^2\beta - 1\right] Q_0. \tag{1.16}$$

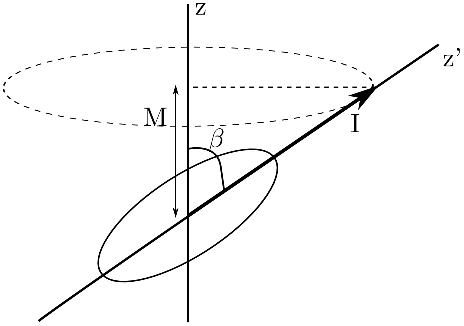

Figure 1.2: Axially symmetric charge distribution with symmetry axis z', which makes an angle β with the laboratory z axis. The angular momentum I and its projection on the laboratory z axis, M, are also shown.

In the rotational model (section 1.2.3) the intrinsic quadrupole moment can be related to the deformation of the nucleus.

1.2.2 The harmonic vibrator model

In a coordinate representation, using the quadrupole deformation parameters as collective coordinates, the harmonic vibrator Hamiltonian $\hat{H}_{HV}$ is given by

$$\hat{H}_{HV} = \frac{B}{2} \sum_{\mu} \left| \frac{d\alpha_{2\mu}}{dt} \right|^2 + \frac{C}{2} \sum_{\mu} |\alpha_{2\mu}|^2 \tag{1.17}$$

where B is a mass parameter and C is a restoring force. This Hamiltonian describes the five-dimensional harmonic oscillator, with the $\alpha_{2\mu}$ undergoing oscillations with frequency $\omega = \sqrt{C/B}$ and vibrational energy $\hbar\omega$.

A different representation can be obtained for a vibrator, using the formalism of second quantization. In this approach, operators are defined that create and annihilate vibrational quanta. The Hamiltonian is then rewritten in terms of these operators:

$$\hat{H}_{HV} = \hbar\omega \sum_{\mu} \left(\hat{b}^{\dagger}_{2\mu} \hat{b}_{2\mu} + \frac{1}{2} \right) \tag{1.18}$$

where $\hat{b}^{\dagger}_{2\mu}$ is the operator which creates an oscillator quantum, called the quadrupole phonon ($\lambda = 2$, $\mu = 2$), while $\hat{b}_{2\mu}$ annihilates a phonon. Using the definitions of these operators, it can be shown that the operator $\hat{b}^{\dagger}_{2\mu}\hat{b}_{2\mu}$ counts

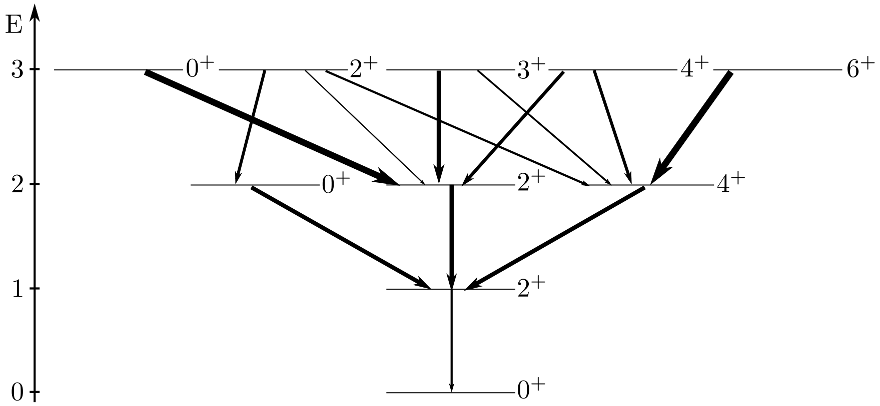

Figure 1.3: Schematic representation of the level energies and spins of an harmonic vibrator. The numbers on the left represent the number of phonons N_{ph} involved in the excited state defining the energy of the state. The $E2$ transition probabilities are represented by black arrows of which the width represents the relative strength.

the number of phonons. This implies that, for N_{ph} phonons, the energy of the system is given by:

$$E_{HV} = \hbar\omega\left(N_{ph} + \frac{5}{2}\right) \tag{1.19}$$

Equation 1.19 shows that the energy levels of an harmonic vibrator display an equidistant pattern. The allowed angular momenta in a vibrational band can be derived by combining the number of phonons N_{ph}, taking care of the fact that the wave function must be symmetric. A one-phonon state gives rise to a state with angular momentum 2 and positive parity, the coupling of two quadrupole phonons gives rise to three degenerate states with spins $0^+, 2^+$ and 4^+, etc. The resulting typical low-energy spectrum of an harmonic vibrator is shown schematically in Figure 1.3.

Figure 1.3 also illustrates the reduced $E2$ transition probabilities between the states. These transition probabilities can be derived by calculating the matrix elements of the $E2$ operator, which is defined as follows in the harmonic vibrator model:

$$\hat{O}(E2,\mu) = \frac{3}{4\pi}ZeR_0^2\left(\frac{\hbar}{2\omega B_\lambda}\right)^{1/2}\left[\hat{b}^\dagger_{2\mu} + (-1)^\mu \hat{b}_{2,-\mu}\right]. \tag{1.20}$$

From the definition of $\hat{O}(E2,\mu)$ it follows that only transitions with $\Delta N_{ph} = \pm 1$ are allowed, inhibiting thereby e.g. transitions between the two-phonon 2_2^+

state and the 0_1^+ ground state. Transitions between a two-phonon state and the one-phonon state are twice as probable as the transition between the one-phonon 2^+ state and the 0^+ ground state:

$$B(E2; J_{N_{ph}=2} \rightarrow J_{N_{ph}=1}) = 2B(E2; 2_1^+ \rightarrow 0_1^+). \tag{1.21}$$

Similarly, the summed transitions between a three-phonon state and all the possible two-phonon states are three times as probable:

$$\sum_{J_{N_{ph}=2}} B(E2; J_{N_{ph}=3} \rightarrow J_{N_{ph}=2}) = 3B(E2; 2_1^+ \rightarrow 0_1^+). \tag{1.22}$$

Another important conclusion from the selection rule $\Delta N_{ph} = \pm 1$ is that the quadrupole moments of vibrational states must vanish. Indeed, a quadrupole moment represents a transition for which $\Delta N_{ph} = 0$, which is forbidden in the harmonic vibrator model that is presented here.

Identifying an harmonic vibrator nucleus

In principle, nuclei can be classified relatively easy as harmonic vibrators by studying the level systematics and transition probabilities. Equi-spaced multiplets, hindered multi-phonon transitions and vanishing quadrupole moments are fingerprints of an harmonic vibrator. Experimentally, only very few nuclei are identified as candidates for harmonic vibrators. Until now, the level energies of ^{106,108,110}Pd and ^{112,114,118}Cd seem to follow the rules, derived in section 1.2.2, reasonably well. However, it is clear that the systematics are disturbed, rendering e.g. large non-zero quadrupole moments for the 2_1^+ states in the Pd isotopes. Also in the Cd isotopes, the harmonic vibrator behavior was disputed when Coulomb-excitation experiments revealed transition probabilities that did not fit at all with harmonic vibrator behavior [13]. Garrett and Wood point to the importance of experimentally deduced transition probabilities for the explanation of low-energy characteristics in nuclei.

In general, two experimental difficulties can be identified. At first, $E2$ decay transition rates contain a factor E_γ^5 which strongly enhances the forbidden, but high energy, transitions. This can lead to the non-observation of the allowed transitions, with large transition probability but small energy. Secondly, multiple causes exist that can distort the harmonic vibrator systematics. The degeneracy of the multiplets of an harmonic vibrator is lifted when going to anharmonic vibrator behavior. Next to that, in nuclei near closed shells intruder states can appear amidst the vibrator states. Intruder states represent a specific excitation across a closed shell that is lowered in energy because of the attractive proton-neutron interaction. Distinguishing between a vibrator state and an intruder state is not trivial and is one of the active topics in the study of the neutron-deficient polonium isotopes.

(Near-)harmonic vibration is very rare in the nuclear chart. It only takes a few valence protons and/or neutrons to make the nucleus more soft against deformation and leave the path of the simple spherical harmonic vibrator model.

1.2.3 The rigid rotor model

The rigid rotor model is the limit of the collective model that studies nuclei with a permanent deformation. Non-spherical nuclei can rotate about an axis perpendicular to the symmetry axis but they can also show vibrational motion. The rigid rotor model only considers the rotational motion. Vibrational-rotational coupling is possible in the framework of the collective model but is not discussed here. The rigid rotor Hamiltonian $\hat{H}_{rot}$ is given by

$$\hat{H}_{rot} = \frac{\hbar^2}{2} \sum_{i=1}^{3} \frac{\hat{I}_i^2}{J_i} \tag{1.23}$$

where $\hat{I}_i$ is the angular momentum relative to the body-fixed axes and J_i is the moment of inertia relative to the same axes. In general, the rotor Hamiltonian has no analytical solutions. However, the exception occurs in the case of axial symmetry, i.e. when the nucleus becomes a symmetric rotor with [14]:

$$J_1 = J_2 = J. \tag{1.24}$$

The rotational Hamiltonian can then be written as

$$\hat{H}_{rot} = \frac{\hbar^2}{2J} \left[\hat{I}^2 - \hat{I}_3^2 \right] \tag{1.25}$$

where $\hat{I}$ is the total angular momentum operator and with energy eigenvalues given by [1, 15, 16]

$$E_{KI} = \frac{\hbar^2}{2J} \left[I(I+1) - K^2 \right] \tag{1.26}$$

where K is the component of the angular momentum along the symmetry axis in the body-fixed frame. For even-even isotopes, with ground-state spin $I = 0$, the ground-state band has $K = 0$. The energies of the ground-state rotational band are then given by

$$E_I = E_0 + \frac{\hbar^2}{2J} \left(I(I+1) \right) \tag{1.27}$$

with E_0 the energy of the ground state. Note that the rotational band, in contrast to a vibrator, does not show equidistant energy levels but a characteristic $I(I+1)$ energy sequence. The $K=0$ rotational bands show the spin sequence $I=0,2,4,6,...$ i.e. only even spins are allowed. Rotational bands where $K\neq 0$ show odd and even spins: $I=K,K+1,K+2,....$ The absence of odd spins in $K=0$ bands is due to the reflection symmetry of the nuclear rotor in a plane perpendicular to its symmetry axis [16].

A rotor band is characterized by an intrinsic quadrupole moment Q_0 which is constant throughout the band and related to the spectroscopic quadrupole moment:

$$Q_s(I,K)=\frac{3K^2-I(I+1)}{(I+1)(2I+3)}Q_0 \tag{1.28}$$

where Q_0 is defined in the body-fixed frame of the nucleus (equation 1.16). In the case where $K=0$ and $I=2$, the spectroscopic and intrinsic quadrupole moment are related trough the following expression: $Q_s=-2/7\;Q_0$. Note that in this case, the spectroscopic and intrinsic quadrupole moment differ in sign. Only the intrinsic quadrupole moment reflects the nuclear charge deformation β_2, which can be written as [17]:

$$Q_0=\frac{3}{\sqrt{5\pi}}ZR^2\beta_2 \tag{1.29}$$

with $R=r_0A^{1/3}$ the radius of the nuclear charge distribution (with $r_0=1.2\,\mathrm{fm}$), Z the number of protons in the nucleus and β_2 as defined in 1.7.

The reduced $E2$ transition rates of a rotational band are related to the intrinsic quadrupole moment:

$$B(E2;I_iK\rightarrow I_fK)=\frac{5}{16\pi}\left(I_iK,20|I_fK\right)^2e^2\left|Q_0(K)\right|^2 \tag{1.30}$$

where $(I_iK,20|I_fK)$ is a Clebsch-Gordan coefficient. Equation 1.30 provides interesting relations which apply to rotational bands. It can be used to relate the $B(E2;2^+\rightarrow 0^+)$ value to the intrinsic quadrupole moment of the rotational band:

$$B(E2;2^+\rightarrow 0^+)=\frac{1}{16\pi}\left|Q_0\right|^2 \tag{1.31}$$

which can be translated in terms of reduced matrix elements, to give

$$\langle 0^+||E2||2^+\rangle=\frac{-7}{2}\begin{pmatrix}2 & 2 & 2\\ -2 & 0 & 2\end{pmatrix}\langle 2^+||E2||2^+\rangle \tag{1.32}$$

giving an expression for the diagonal matrix element of the 2^+ state in a rotational band

$$\left|\langle 2^+||E2||2^+\rangle\right|=1.195\left|\langle 0^+||E2||2^+\rangle\right|. \tag{1.33}$$

In the derivation of expression 1.32, the definition of the $B(E2)$ value (equation 1.8), the relationship between the intrinsic and spectroscopic quadrupole moment (equation 1.28) and the Wigner-Eckart theorem (equation 1.9) are used. The reduced transition probabilities within one rotational band are also related to each other through the constant intrinsic quadrupole moment:

$$B(E2; I^+ \to (I-2)^+) = \frac{15I(I-1)}{2(2I-1)(2I+1)} B(E2; 2^+ \to 0^+). \tag{1.34}$$

This provides us with another frequently used relation: $B(E2; 4^+ \to 2^+) = 1.429 \times B(E2; 2^+ \to 0^+)$.

Experimentally, rotational characteristics have been identified throughout the nuclear chart, especially in open-shell regions. However, deviations from the $I(I+1)$ energy sequence are observed frequently, pointing towards the need for additional degrees of freedom in the rotational model [1]. Section 5.4.2 explains the basics of the variable moment of inertia (VMI) model, which applies to soft rotor nuclei. Also, by combining rotational and vibrational degrees of freedom, the applicability of the collective model is enhanced [1, 2].

1.3 The neutron-deficient Po isotopes

The neutron-deficient polonium isotopes ($Z = 84$), with only two protons outside the closed $Z = 82$ shell, are situated in an interesting region of the nuclear chart. The interest in this region has been triggered by the discovery of evidence of shape coexistence in the light-lead region. These included, amongst others, the large odd-even staggering in the charge radii of the neutron-deficient mercury isotopes [18] and the observation of three low-lying 0^+ states with different deformation within an energy span of only 700 keV in the ^{186}Pb nucleus [19]. Nuclear shape coexistence is the phenomenon in which states at similar excitation energy exhibit a different intrinsic deformation. By now, it is established to appear throughout the whole nuclear landscape, in light, medium and heavy nuclei [20].

Polonium isotopes have two protons outside a closed proton shell configuration ($Z = 84$) and an open neutron shell. The two-proton particle degree of freedom, coupled to the core of 82 protons, will play an important role in the level systematics. The residual interaction between these two protons and the valence neutrons might be a driving force towards collective effects and deformation.

1.3.1 Available experimental information

In the last decades, a variety of experimental techniques have been used to study the nuclear structure of the neutron-deficient polonium isotopes. Studies employing techniques of α-, β- and in-beam γ-decay spectroscopy, laser spectroscopy and lifetime measurements revealed information on level systematics, spins, ground-state properties and transition probabilities. Compared to the relatively well-studied platinum, mercury and lead isotopes where various studies reach isotopes across neutron mid-shell $N \leq 104$, the information related to the neutron-deficient polonium isotopes is limited to $N > 104$. The small production cross sections are a challenge to the experimental nuclear physicist. This is reflected in the relative scarceness of information available for the lightest polonium isotopes.

Energy spectra

The band structure of the neutron-deficient even-even polonium isotopes has been studied extensively. The energy systematics resulting from these studies for the $^{190-204}$Po isotopes are shown in Figure 1.4.

Several in-beam γ-ray spectroscopic studies have been performed, producing the neutron-deficient polonium isotope of interest through fusion-evaporation reactions. Low production cross sections, competing with a dominant fission channel make these experiments challenging. The recoil-decay-tagging technique (RDT), in which characteristic decay products (e.g. α particles) from the fusion products are used to resolve the prompt γ rays emitted at the target, has provided a new tool to extract information from in-beam experiments. These in-beam experiments were performed at various facilities, including the Hahn-Meitner Institut [21–23], the ATLAS facility [24–27] and the Accelerator Laboratory of the University of Jyväskylä [28–33] and led to the assignment of several level energies, spins and parities.

Next to that, α and β-decay studies at the ISOLDE (CERN, Geneva), LISOL (Louvain-la-Neuve), JYFL (Jyväskylä) and SHIP (GSI, Darmstadt) facilities revealed additional information and led to the identification of 0_2^+ states [31, 34–45].

The closed neutron-shell nucleus ^{210}Po ($N = 126$) offers a textbook example of a “two-proton nucleus”: most of the excited levels can be understood in the framework of two-proton excitations in the orbitals above $Z = 82$. When going down in neutron number, the 2_1^+ and (to a lesser extent) the 4_1^+ state are suddenly lowered in energy. The energy of the 2_1^+ state remains rather constant for mass $200 \leq A \leq 208$, as can be seen on the energy systematics shown in

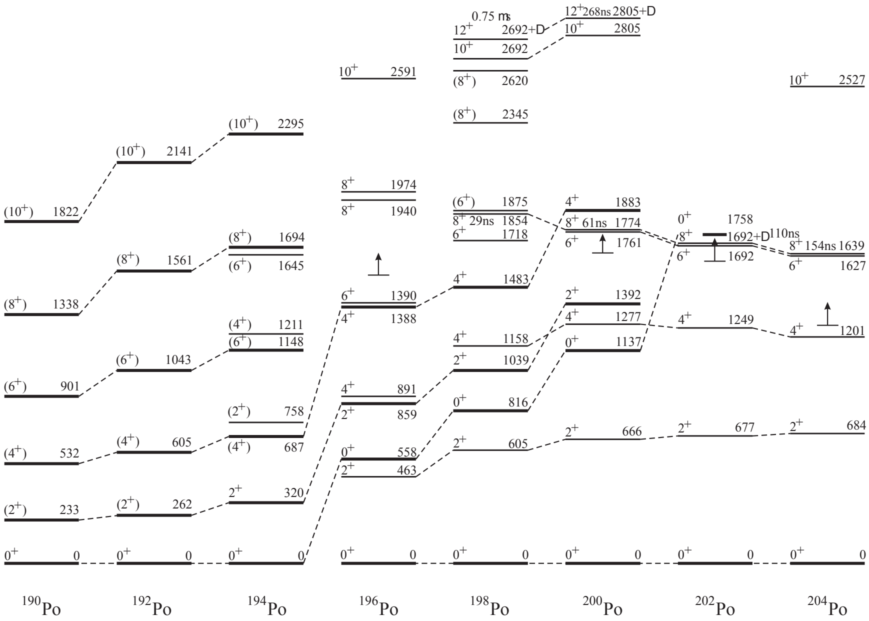

Figure 1.4: Energy level systematics of the excited states in the neutron-deficient even-mass Po isotopes. Dashed lines connect states that are assumed to have a similar structure. The 8^+ isomers are indicated by their half-lives. Figure is taken from [20].

Figure 1.4. ^{200}Po seems to mark somehow the end of a “regular” structure, with the observation of a downsloping trend for nearly all states from ^{198}Po onwards.

Electromagnetic properties

Reduced transition probabilities (e.g. $B(E2)$ values) provide a measure of collectivity as explained in section 1.2.1. One way of determining these reduced transition probabilities is by measuring the lifetime of levels, which has been done for the low-lying states in ^{194,196}Po [46, 47]. Next to that, lifetimes and g factors of isomeric 8^+, 11^- and 12^+ states were determined in an in-beam γ-ray spectroscopic study [21]. Early inelastic scattering studies of ^{210}Po provided information on the $B(E2; 2^+ \to 0^+)$ value at the neutron shell closure [48]. Overall, the information regarding reduced electric quadrupole transition probabilities is limited in the neutron-deficient polonium isotopes.

Another method of determining these transition probabilities is the technique of Coulomb excitation, as will be explained in Chapter 2.

Ground-state properties

Recently, in-source resonant ionization laser spectroscopy studies of the neutron-deficient polonium isotopes were performed at the ISOLDE facility [49, 50]. The results of the measurement of changes in mean-square charge radii $\delta\langle r^2\rangle$ in a wide range of polonium isotopes, displayed in Figure 1.5, point to an onset of deviation from sphericity around ^{198}Po . Comparison of the mean-square charge radii of the polonium isotopes with their isotones below $Z = 82$, as shown in Figure 1.5, suggests that the deviation from sphericity of the ground states sets in earlier above $Z = 82$ [50]. Extending the results towards the more neutron-deficient radon ($Z = 86$) and radium ($Z = 88$) isotopes would be interesting to confirm or refute this hypothesis [51]. The platinum isotopes with $Z = 78$ show a similar early, but smaller in magnitude, onset of deviation from sphericity as the polonium isotopes [52, 53].

1.3.2 Theoretical considerations

The experimental information was complemented by theoretical studies applying different nuclear models. In a first approach the observed level energies were explained by considering two protons coupled to a vibrating lead core in the Particle-Core model (PCM) [54–56]. A general seniority-based behavior, where the first broken pair produces the first excited state at a constant excitation energy, was also applied to describe the near-constant energy of the 2_1^+ state in the $^{200-208}$Po isotopes [57].

Different theoretical frameworks have been used for the study of the lighter polonium isotopes with mass $A < 200$. The experimentally observed trends could be reproduced by using the particle-core coupling approach. However, the proton-core coupling interaction strength needs to be increased sharply to do so [54]. Bernstein et al. also attributed the excited states in the lighter polonium isotopes to an anharmonic vibrator and explained the increasingly collective behavior by a larger role of the $\nu i13/2$ orbital and its overlap with the $\pi 1h9/2$ orbital [24]. Later, it was concluded that one cannot describe the energy systematics of the $^{192-198}$Po isotopes using an anharmonic vibrator framework by keeping the PCM parameters in a physically meaningful range [56].

Although vibrational characteristics can be identified in the level systematics of the polonium isotopes, the observation of the downsloping trend of the 0_2^+

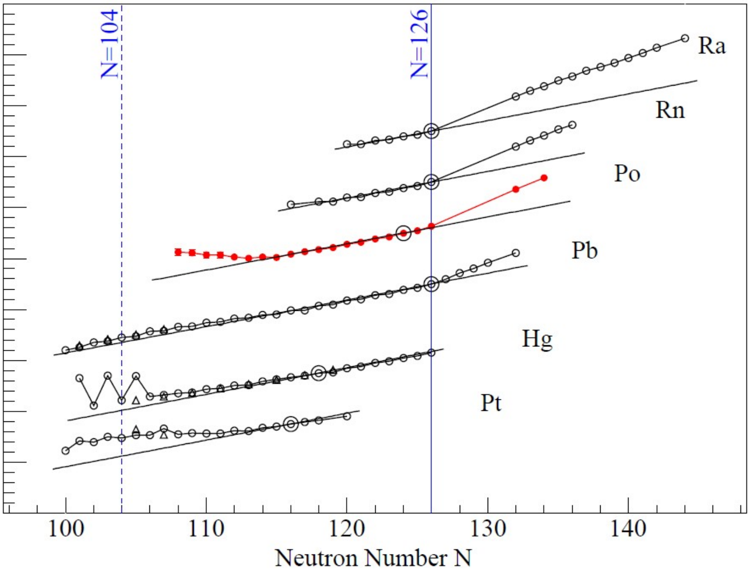

Figure 1.5: Systematics in the changes in mean-square charge radii $\delta\langle r^2\rangle$ for the even-Z platinum ($Z = 78$), mercury ($Z = 80$), lead ($Z = 82$), polonium ($Z = 84$) (in red), radon ($Z = 86$) and radium ($Z = 88$) isotopes. The large circles indicate the reference isotope for each chain. The solid line represents the prediction of the spherical droplet model. The figure is taken from [49].

states in $^{196-202}$Po is hard to be understood within the particle-core coupling description. In a different approach, the energy systematics of the 0_2^+ states were studied within the phenomenological Pairing Vibration Model, suggesting that these states are of $4p-2h$ structure [56]. Particle-hole excitations across the $Z = 82$ shell closure were also incorporated in calculations using the Interacting Boson Model (IBM) [56, 58].

Early Nilsson-Strutinsky calculations already predicted the appearance of deformed shapes at low energy in the lightest polonium isotopes with mass $A \leq 192$ [59]. Later studies also performed potential energy surface calculations [56, 60]. Self-consistent mean-field methods and beyond mean-field studies of the polonium isotopes were also performed to study the different structures in the polonium isotopes [61, 62]. A common conclusion of all the theoretical studies, except for the vibrator-based studies, was the presence of shape coexistence in the lightest polonium isotopes and possibilities of mixing of the deformed configurations [20, 56, 61, 62].

In this thesis the results from Coulomb-excitation studies of the neutron-deficient $^{196-202}$Po isotopes are shown. The extracted transition probabilities provide new information about the transition from a two-particle, seniority-based, behavior for the heavier polonium isotopes to a picture in the lighter isotopes where shape coexistence and mixing of different configurations gains importance.

2 | Coulomb excitation

When the electromagnetic interaction between a colliding projectile and target nucleus causes one of the two nuclei to get excited, the process is called Coulomb excitation ("Coulex"). At incident energies low enough that the Coulomb repulsion prevents the intrusion of the nuclei into each other, the process can be studied without taking into account nuclear interactions. This chapter aims to give a brief description of the basic aspects of the theory of Coulomb excitation and the Coulomb-excitation analysis code GOSIA. Extended review articles and books have been published on the subject. For more detailed information the reader is referred to [63–65].

2.1 Theoretical description

2.1.1 Semi-classical approach

Figure 2.1 represents the scattering process of an incoming projectile nucleus on a stationary target schematically. The motion of the projectile in the Coulomb field of the target nucleus can be characterized by the dimensionless Sommerfeld parameter η, which is defined as the ratio of half of the distance of closest approach, a, to the reduced de Broglie wave length, $\frac{\lambda}{2\pi}$ [66]:

$$\eta = \frac{a}{\lambda/(2\pi)} = \frac{Z_p Z_t e^2}{\hbar v} \tag{2.1}$$

where $Z_p e$ and $Z_t e$ are the charge of the projectile and target nucleus respectively and v is the velocity of the incident particle at a large distance from the target nucleus. Large values of the parameter η ($\gg 1$) correspond to conditions in which the reduced wavelength is small compared to the distance of closest approach, i.e. the two nuclei do not penetrate into the region where the strong

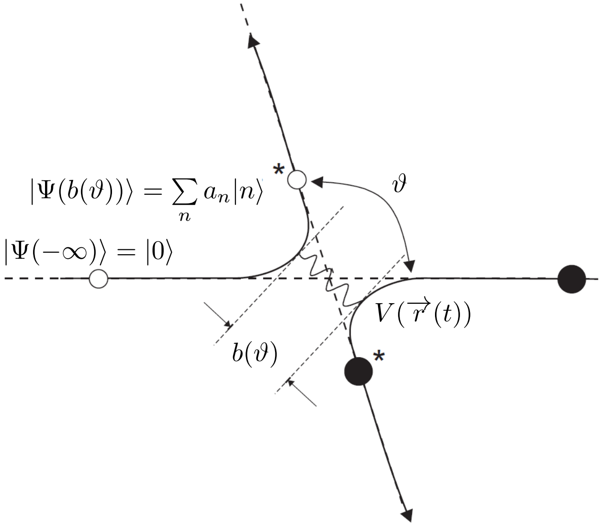

Figure 2.1: Schematic representation of the scattering process of an incident projectile on a stationary target nucleus, in the reference system where the center-of-mass is at rest. ϑ represents the scattering angle in the centre-of-mass frame and $b(\vartheta)$ is the distance of closest approach [67].

interaction plays a role. In that case the scattering process can be described semi-classically and the Coulomb-excitation process is considered to be "safe". For example, a 559 MeV ^{196}Po projectile, incident on a ^{104}Pd target, yields an η parameter of 362 which is well above 1.

In terms of the classical picture, the condition for safe Coulomb excitation can also be formulated using the distance of closest approach. Nuclear reactions are shown to be conservatively below 1 % of the total excitation when the nuclei are separated by a distance of at least 5 fm [65]:

$$b \geq 5 + R_t + R_p = 5 + r_0\left(A_t^{1/3} + A_p^{1/3}\right) \tag{2.2}$$

where R_t and R_p are the radii of the target and projectile nucleus respectively and $A_{t(p)}$ is the nucleon number of the target (projectile) nucleus.

In order for the excitation to have negligible influence on the motion of the particles, a further condition is that all possible excitation probabilities are small. The adiabaticity parameter ξ, which is the ratio of the collision time

τ_{coll} to the nuclear period τ_{nucl}, must be much less than 1 [68]:

$$\xi = \frac{\tau_{coll}}{\tau_{nucl}} = \frac{a}{v}\frac{\Delta E}{\hbar} = \frac{Z_p Z_t e^2}{\hbar v}\frac{\Delta E}{2E} \ll 1 \tag{2.3}$$

where ΔE is the excitation energy of the excited nucleus and E is the incident energy of the projectile. The cases studied in this thesis also satisfy the second requirement since typical excitation energies are of the order of 1 MeV compared to the incident energy of the projectiles that exceeds 550 MeV, giving rise to $\xi \approx 0.2$ for the projectile-target combinations of this thesis.

2.1.2 First-order perturbation theory

Since the condition in equation 2.3 is satisfied, a first-order perturbation theory approach can be applied. The differential cross section for Coulomb excitation $\frac{d\sigma}{d\Omega}$ can then be written as

$$\frac{d\sigma}{d\Omega} = P\frac{d\sigma_R}{d\Omega} \tag{2.4}$$

where P is defined as the probability that one of the two nuclei gets excited during the collision and $\frac{d\sigma_R}{d\Omega}$ is the differential cross section for (elastic) Rutherford scattering. In the semi-classical description the projectile moves on a hyperbolic orbit in the repulsive Coulomb field of the target. The differential Rutherford cross section at angle ϑ is described by:

$$\frac{d\sigma_R}{d\Omega} = \frac{a^2}{4\sin^4\left(\frac{\vartheta}{2}\right)} \tag{2.5}$$

with $a = \frac{Z_p Z_t e^2}{m_0 v^2}$ the distance of closest approach in which m_0 is the reduced mass of the projectile and target nucleus. The Rutherford cross section peaks at small scattering angles in the centre-of-mass system. The probability for Coulomb excitation P depends on the spin of the initial nuclear state I_i and contains a sum over the magnetic quantum numbers of the initial and final states:

$$P = \frac{1}{2I_i + 1}\sum_{M_i M_f} |b_{if}|^2 \tag{2.6}$$

with b_{if} the amplitude for a transition from the initial nuclear level i to the various final states f. As the probability for excitation in a single encounter is very small, first-order perturbation theory can be applied to describe the excitation amplitudes b_{if}:

$$b_{if} = \frac{1}{i\hbar}\int_{-\infty}^{+\infty} \langle f|H|i\rangle \exp^{i\frac{E_f - E_i}{\hbar}t}\, dt \tag{2.7}$$

where H is the interaction energy.

If only electric excitations are considered, the interaction energy H_E, which is the Coulomb energy, can be expanded in its multipole components:

$$H_E(t) = 4\pi Z_p e \sum_{\lambda=1}^{\infty} \sum_{\mu=-\lambda}^{+\lambda} \frac{1}{2\lambda+1} r^{-\lambda-1} Y_{\lambda\mu}(\vartheta,\varphi)\hat{O}(E\lambda,\mu) \tag{2.8}$$

where $Y_{\lambda\mu}(\vartheta,\varphi)$ are the normalized spherical harmonics evaluated at the polar coordinates ϑ and φ in the centre-of-mass system and $\hat{O}(E\lambda,\mu)$ are the electric multipole moment operators of the nucleus ondergoing the excitation [63]. The classical expression for these operators is given by

$$\hat{O}(E\lambda,\mu) = \int r^{\lambda} Y_{\lambda\mu}(\vartheta,\varphi)\rho_n(\overrightarrow{r})d\tau \tag{2.9}$$

and when applied to the atomic nucleus as a collection of A individual nucleons with $\rho_n(\overrightarrow{r}) = \sum\limits_k e_k \delta(\overrightarrow{r} - \overrightarrow{r_k})$; one obtains the quantum mechanical expression for the operator to be used in equation 2.8 [63]:

$$\hat{O}(E\lambda,\mu) = \sum_k e_k r_k^{\lambda} Y_{\lambda\mu}(\vartheta_k,\varphi_k). \tag{2.10}$$

Expression 2.8 holds if the projectile remains outside of the zone where the strong interaction is active, which is valid in all cases studied in this thesis. The differential cross section for electric Coulomb excitation can then be evaluated as:

$$\frac{d\sigma_E}{d\Omega} = \sum_{\lambda=1}^{\infty} \frac{d\sigma_{E\lambda}}{d\Omega} \tag{2.11}$$

with

$$\frac{d\sigma_{E\lambda}}{d\Omega} = \frac{4\pi^2 Z_p^2 e^2 a^2}{\hbar^2} \frac{1}{\sin^4\left(\frac{\vartheta}{2}\right)} \frac{B(E\lambda)}{(2\lambda+1)^3} \sum_{\mu} |S_{E\lambda,\mu}|^2, \tag{2.12}$$

where $B(E\lambda)$ is the reduced $E\lambda$ transition probability as defined in 1.8. In order to write the cross section in this compact form, the orbital integrals $S_{E\lambda,\mu}$ are introduced [63]:

$$S_{E\lambda,\mu} = \int_{-\infty}^{+\infty} \exp^{i\frac{E_f-E_i}{\hbar}t} Y_{\lambda\mu}(\vartheta,\varphi) r^{-\lambda-1} dt. \tag{2.13}$$

For electric excitations, the usual parity selection rule for electric multipole radiation is valid: an electric excitation of multipole order λ involves a parity change of $(-1)^{\lambda}$. Excitations of opposite parity $((-1)^{\lambda+1})$ are produced by the magnetic field. However, the cross section for magnetic excitation $d\sigma_{M\lambda}$ is small compared to electric excitation as the magnetic Coulomb-excitation cross section $d\sigma_{M\lambda}$ has an additional factor $(v/c)^2$, compared to $d\sigma_{E\lambda}$. For "safe" Coulomb-excitation reactions the projectile velocity is small compared to the speed of light, giving rise to a reduction of the magnetic Coulomb-excitation cross section, compared to the electric cross section $d\sigma_{E\lambda}$, by 3 orders of magnitude in the cases studied. On top of that, magnetic nuclear matrix elements are generally smaller than electric matrix elements.

The cross section for excitation and the lifetime of a radiative decay transition are linked by a simple relation. The probability for a decay transition to happen is given by

$$T = \frac{8\pi(\lambda+1)}{\lambda\hbar\left[(2\lambda+1)!!\right]^2}\left(\frac{\omega}{c}\right)^{2\lambda+1} B(\lambda, I_f \to I_i). \tag{2.14}$$

In this expression the reduced transition probability $B(\lambda, I_f \to I_i)$ for the decay is related by

$$B(\lambda, I_f \to I_i) = \frac{2I_i+1}{2I_f+1} B(\lambda, I_i \to I_f) \tag{2.15}$$

to the reduced transition probability relevant for the excitation process.

2.1.3 Higher-order effects

Even though first-order perturbation theory can be used, in some cases, especially in heavy-ion reactions, the probability P for excitation can become appreciably large with respect to the elastic scattering process. In that case higher-order effects can not be neglected.

The excitation probability of a state f can be written as

$$P_f = P_f^{(1)} + P_f^{(1,2)} + P_f^{(2)} \tag{2.16}$$

where $P_f^{(1)}$ is the first-order excitation probability which can conveniently be written as the product of a strength function and a radial function:

$$P_f^{(1)} = \sum_\lambda |\chi^\lambda_{i\to f}|^2 R^2_\lambda(\vartheta, \xi) \tag{2.17}$$

where the summation runs over the possible multipolarities of the transition [67]. The function $R^2_\lambda(\vartheta, \xi)$ contains the dependence on the scattering angle ϑ and on the adiabaticity parameter ξ, which is related to the incident particle energy and the nuclear excitation energy (see equation 2.3). The strength function $\chi^\lambda_{i\to f}$ describes the excitation probability for a λ-pole excitation to the state f in the case where $\vartheta = \pi$ and $\xi = 0$ [63].

The second term in equation 2.16 is the interference between first and second-order effects and the third term contains the effects of second order. In the higher-order terms $P_f^{(1,2)}$ and $P_f^{(2)}$, a summation occurs over all possible intermediate states z as illustrated in panel A) of Figure 2.2. Terms involving highly-excited intermediate states vanish so the sum can be limited to states in the low-lying spectrum which are strongly coupled to the ground state.

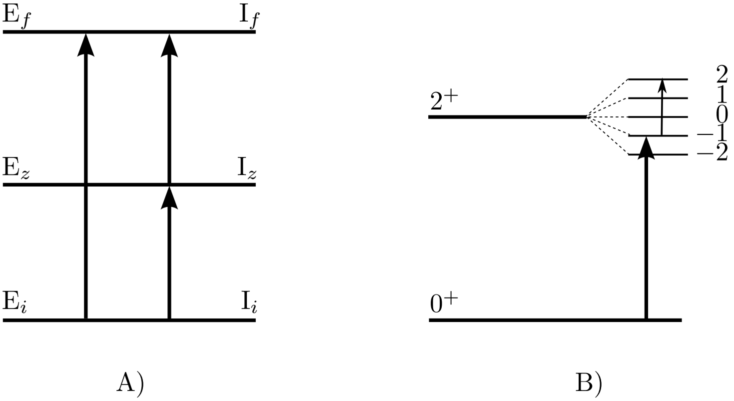

Figure 2.2: A) Excitation of the final state with spin I_f can proceed in one step or in a two-step process, through the intermediate state with spin I_z. Note that the intermediate state can also lie above the final state, in that case $\mathrm{E}_z > \mathrm{E}_f$. B) Excitation of a 2^+ state from a 0^+ ground state can proceed through the magnetic substates of the 2^+ state. This special case of a two-step excitation is called the reorientation effect.

The interference effects contained in $P_f^{(1,2)}$ include the reorientation effect related to the influence of the quadrupole moment of the excited state. Excitations that can not proceed through a one-step process or where the first-order process is weak, are called double excitations. These two effects are discussed in the case where only one intermediate state is of importance. This idealized situation is applicable to the reactions studied in this thesis.

Two-step excitations

A pure double excitation only occurs when the direct excitation probability $I_i \rightarrow I_f$ is small or vanishing:

$$\chi_{i\rightarrow f} \ll \chi_{i\rightarrow z}\chi_{z\rightarrow f}. \tag{2.18}$$

A first example of such a process is the excitation of an excited 0^+ state through the intermediate 2_1^+ state. As the direct transition $0_1^+ \rightarrow 0_2^+$ is not possible in that case, a pure double excitation takes place to populate the 0_2^+ state. Another frequently occurring double excitation is involved in the excitation of a 4^+ state. In this case the direct excitation is not forbidden but can only proceed through an $E4$ interaction which is usually quite weak.

However, also a strong competition between the one-step process and the excitation through the intermediate state can occur. In a heavy even-even nucleus like polonium, a second excited 2_2^+ state often occurs at low excitation energy. The direct excitation $0_1^+ \rightarrow 2_2^+$ competes strongly with the double excitation through the 2_1^+ state ($0_1^+ \rightarrow 2_1^+ \rightarrow 2_2^+$). The total excitation probability of the 2_2^+ state can then be written as

$$P_{2_2^+} = |\chi^2_{0_1^+\rightarrow 2_2^+}|^2 R_2^2(\vartheta,\xi)\,[1 + y \cdot c(\vartheta,s,\xi)] \tag{2.19}$$

with

$$y = \frac{\chi_{0_1^+\rightarrow 2_1^+}\chi_{2_1^+\rightarrow 2_2^+}}{\chi_{0_1^+\rightarrow 2_2^+}} = \chi_{0_1^+\rightarrow 2_1^+}\frac{1}{\sqrt{5}}\frac{\langle 2_1^+||E2||2_2^+\rangle}{\langle 0_1^+||E2||2_2^+\rangle} \tag{2.20}$$

and where $c(\vartheta,s,\xi)$ contains the dependence on scattering angle, adiabaticity parameter and on the parameter s which is the ratio of energy differences: $s = \frac{E_z - E_i}{E_f - E_i}$ [64]. Note that the excitation probability $P_{2_2^+}$ depends on the relative sign of the $E2$ matrix elements related to the 2_2^+ state. This relative sign is independent of the phase convention of the nuclear wave functions (see later in section 2.1.4). The contribution of the three-step process is small in most cases. However, in the heavy even-even isotopes that are studied in this thesis, three-step excitation of the 2_2^+ state through $0_1^+ \rightarrow 2_1^+ \rightarrow 0_2^+ \rightarrow 2_2^+$ can occur.

Reorientation effect

A special case of a two-step excitation, shown in panel B) of Figure 2.2 for the excitation of a 2^+ state from a 0^+ ground state, occurs when the intermediate state is a magnetic substate of the initial or final state. In an even-even nucleus, the 0^+ ground state has no magnetic substates. Yet, the electric and magnetic fields involved in the collision of the highly-charged projectile and target nucleus, make the 2^+ state split up. The interference effect describing the influence of the magnetic substates of the 2^+ state on the excitation probability of the 2^+ state is called the reorientation effect [64]. The excitation probability in this case is a special case of equation 2.19 with $2_1^+ = 2_2^+$:

$$P_{2_1^+} = P_2^{(1)}\,[1 + q \cdot K(\vartheta,\xi)] \tag{2.21}$$

in which $P_2^{(1)}$ is the first-order excitation probability and

$$q = \frac{A_p \Delta E \langle 2_1^+ || E2 || 2_1^+ \rangle}{Z_p (1 + A_p/A_t)}. \tag{2.22}$$

The excitation energy ΔE is given in MeV and the function $K(\vartheta, \xi)$ expresses the dependence on the adiabacity parameter and scattering angle [64]. Sensitivity to the diagonal matrix element of the 2_1^+ state can thus be obtained by either varying in projectile-target combination (e.g. by using two targets with different mass) or in scattering angle. The latter approach is used in this work, where the particle detector (described in Chapter 3) is divided in annular strips in order to gain position sensitivity. By comparing relative cross sections for Coulomb excitation in different angular regions of the centre-of-mass system, the diagonal matrix element of the 2_1^+ state can be determined. An example of the sensitivity to the reorientation effect is illustrated in Figure 2.3 for the reaction of a ^{200}Po projectile on a ^{104}Pd target.

The transitional matrix element $\langle 0_1^+ || E2 || 2_1^+ \rangle$ could be determined in the region at low centre-of-mass scattering angles where the influence of the reorientation effect is negligible. However, with the geometry of the current experimental setup that was used, as described in Chapter 3, this angular range is not feasible. As a consequence, the reorientation effect has to be taken into account throughout the whole angular range.

2.1.4 Experimental sensitivity to higher order effects

The cross section for Coulomb excitation depends in first order on the matrix element coupling the ground state to the first excited state, which is $\langle 0_1^+ || E2 || 2_1^+ \rangle$ for the even-even polonium isotopes that were studied in this thesis. The influence of higher-order effects, e.g. the influence of the quadrupole moment of the 2_1^+ state and the contribution of various excitation paths in the case of multi-step Coulomb excitation, varies with scattering angle, as shown in equations 2.19 and 2.21. The use of differential measurements of the Coulomb-excitation cross section at different scattering angles is a powerful tool to gain sensitivity on these subtle higher-order effects.

In this thesis, the data is divided into subsets corresponding to different ranges of scattering angles. The number of subdivisions is a compromise between the level of statistics in each subdivision and the increase in number of independent data points for the Coulomb-excitation analysis and is explained in Chapter 4 for each isotope individually. The six different ranges, expressed in centre-of-mass angles, that were covered by the differential measurements in the ^{200}Po experiment, are shown in Figure 2.3.

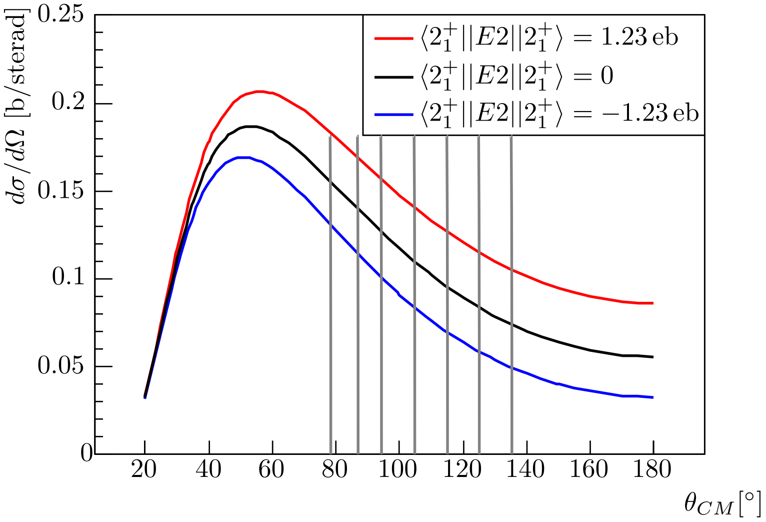

Figure 2.3: Differential cross section for Coulomb excitation of a 570 MeV ^{200}Po projectile scattered on a $2.0\,\mathrm{cm}^2$ thick ^{104}Pd target, for three different values of the diagonal matrix element of the 2_1^+ state, as a function of the scattering angle in the centre-of-mass system θ_{CM}. The adopted value for the transitional matrix element $\langle 0_1^+||E2||2_1^+\rangle$ in ^{200}Po is the result determined in this work, $\langle 0_1^+||E2||2_1^+\rangle = 1.03\,\mathrm{eb}$. The diagonal matrix element $\langle 2_1^+||E2||2_1^+\rangle$ is fixed at $-1.23\,\mathrm{eb}$, $0\,\mathrm{eb}$ and $1.23\,\mathrm{eb}$. The negative and positive values are the limits, calculated using the rotational model (using equation 1.33), related to the value for the transitional matrix element that was extracted in this work. The grey vertical lines represent the ranges in the centre-of-mass frame that were covered by the differential measurements.

Figure 2.4 is an illustration of the changing contribution of different excitation paths with centre-of-mass scattering angle in the experiment of ^{196}Po on ^{104}Pd. Population of the 4_1^+ state is only possible through a two-step process $0_1^+ \rightarrow 2_1^+ \rightarrow 4_1^+$ while the 2_1^+ state is populated in one step. At higher centre-of-mass scattering angles and thus smaller impact parameters the probability for multi-step Coulomb excitation is enhanced as is evident from the increased intensity of the $4_1^+ \rightarrow 2_1^+$ transition, relative to the $2_1^+ \rightarrow 0_1^+$ intensity.

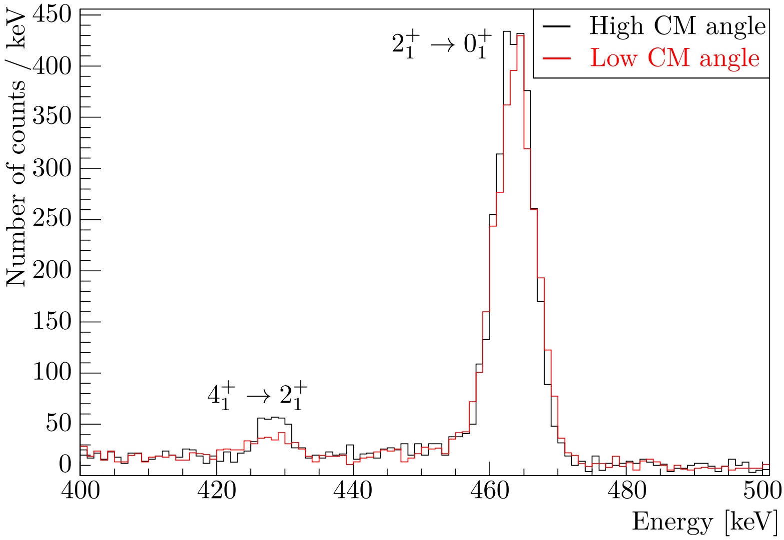

Figure 2.4: Zoom of background-subtracted and projectile Doppler-corrected γ spectrum showing the Coulomb excitation of ^{196}Po on a ^{104}Pd target. The spectrum in red is constructed by gating on the low centre-of-mass region ($66° < \theta_{CM} < 93°$), while the spectrum in black represents the high centre-of-mass region $93° < \theta_{CM} < 128°$. The spectra are normalized to the area underneath the $2_1^+ \rightarrow 0_1^+$ peak.

Sensitivity to signs of matrix elements

The cross section for Coulomb excitation is sensitive to both the magnitude and relative sign of the excitation paths contributing to the population of a certain state. These signs are related to the relative signs of the individual matrix elements. As the excitation amplitude for a certain path is proportional to the product of the matrix elements that are involved, the relative sign of the matrix elements can be deduced from a Coulomb-excitation experiment. Equations 2.19 and 2.20 show the dependence on the relative sign of $\langle 2_1^+||E2||2_2^+\rangle$ and $\langle 0_1^+||E2||2_2^+\rangle$ in the case where the population of the 2_2^+ state is studied.

As the phase of a wave function is arbitrary, it is recommended to fix the phases of certain states following a logical convention. In the present work, the signs of the wave functions of the excited nuclear states have been chosen in such a way that all $E2$ matrix elements for transitions within a band are positive. Next to

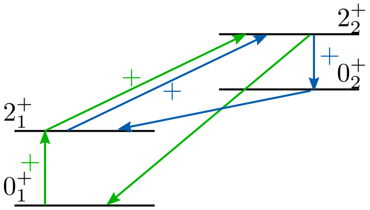

Figure 2.5: Schematic picture of typical level scheme of low-lying 0^+ and 2^+ states in a heavy even-even nucleus like the isotopes studied in this thesis. The arrows indicate the two loops that can be formed when studying the population of the 2_2^+ state. Following the convention explained in the text, the matrix elements taken to be positive: $\langle 0_1^+||E2||2_1^+\rangle$, $\langle 2_1^+||E2||2_2^+\rangle$ and $\langle 0_2^+||E2||2_2^+\rangle$ are denoted with a positive sign. The two loops are depicted with a different color.

that, the sign of the interband matrix element $\langle 2_1^+||E2||2_2^+\rangle$ was also taken to be positive. The signs of the remaining matrix elements should be, in principle, physical observables [69]. These signs were varied relative to the fixed signs by carefully adopting various initial values.

As an example of the implementation of the convention related to the determination of the relative signs of the matrix elements, the population of the 2_2^+ state in ^{196,198}Po is examined. In this case, five transitional matrix elements are involved in the population of the 2_2^+ state: $\langle 0_1^+||E2||2_1^+\rangle, \langle 2_1^+||E2||2_2^+\rangle, \langle 0_1^+||E2||2_2^+\rangle, \langle 0_2^+||E2||2_2^+\rangle$ and $\langle 2_1^+||E2||0_2^+\rangle$. In practice, the relative signs of these matrix elements can be represented as the sign of two different loops of matrix elements, called interference terms. The loops that are involved in this case are depicted schematically in Figure 2.5. The sign of a loop is defined as the product of the signs of the matrix elements that are involved in the loop, i.e. the sign of the green loop in Figure 2.5 is the sign of $\langle 0_1^+||E2||2_1^+\rangle \times \langle 2_1^+||E2||2_2^+\rangle \times \langle 0_1^+||E2||2_2^+\rangle$. Following the convention, $\langle 0_1^+||E2||2_1^+\rangle, \langle 0_2^+||E2||2_2^+\rangle$ and $\langle 2_1^+||E2||2_2^+\rangle$ are taken to be positive. This means that the sign of the green loop is determined by the sign of $\langle 0_1^+||E2||2_2^+\rangle$ and the sign of $\langle 2_1^+||E2||0_2^+\rangle$ renders the sign of the blue loop. In total, four combinations of relative signs of these matrix elements are possible. It is important to notice that the adopted sign convention does not influence the extracted physics result. The observable is the sign of a loop of matrix elements. This means that one can choose to change the sign of an individual matrix element. However, as a consequence, this will also change other signs of matrix elements in order to keep the sign of the loop unaltered.

2.2 The GOSIA code

The unknown matrix elements coupling the low-lying states in the polonium isotopes affect the Coulomb-excitation cross section in a complex way. In order to determine these matrix elements, the coupled-channels code GOSIA [70, 71] is used. GOSIA is a least-squares fitting code that calculates the de-excitation γ-ray yields based on a set of matrix elements coupling the relevant states and compares them to the experimental γ-ray yields. Semi-classical perturbation theory is used to calculate the Coulomb-excitation probabilities based on the kinematics of the reaction. From that the γ-ray yields are determined by taking into account the position and geometry of the germanium detectors and the relative detection efficiencies at the relevant energies. The total yields result finally from integration over the particle scattering range and the energy of the incoming projectile, taking into account the energy loss in the target.

The integration of the yields over scattering angle and bombarding energy, with up to 30 meshpoints and 50 sub-meshpoints for the angular and energy range, is time consuming. However, the fitting procedure is sped up by calculating the yields at average values of energy and angle. These average yields are called the "point yields", $Y_{\text{point}}\left((I_i \rightarrow I_f), E, \theta_p\right)$, and are related to the integrated yields by a constant correction factor. Only if the matrix elements diverge significantly, the full integrated yield calculation has to be repeated to recalculate the correction factors:

$$Y_{\text{int}}\left(I_i \rightarrow I_f\right) = \int_{E_{min}}^{E_{max}} \frac{1}{dE/dx} dE \int_{\theta_{p,min}}^{\theta_{p,max}} Y_{\text{point}}\left((I_i \rightarrow I_f), E, \theta_p\right) \sin\left(\theta_p\right) d\theta_p. \tag{2.23}$$

In this, dE/dx are the electronic and nuclear stopping powers, describing the energy loss in the target. To be able to compare the experimental γ-ray yields to the average point yields, the experimental yields are transformed according to:

$$Y^c_{\text{exp}}\left(I_i \rightarrow I_f\right) = Y_{\text{exp}}\left(I_i \rightarrow I_f\right) \frac{Y_{\text{point}}(I_i \rightarrow I_f)}{Y_{\text{int}}(I_i \rightarrow I_f)} \tag{2.24}$$

where the superscript c stands for the "corrected" value. The calculated γ-ray yields are corrected for effects such as: internal conversion, the energy-dependent efficiency of the γ-ray detectors and the angular distribution of the emitted radiation.

A minimization is performed varying the unknown matrix elements until convergence is reached. The convergence of the fit can be improved by adding known spectroscopic data, e.g. γ-ray branching ratios, lifetime values, known matrix elements or mixing amplitudes. All experimental data, and their uncertainties, are used to construct a least-squares statistic. The minimum of this statistic determines the solution, while its behavior in the vicinity of the minimum defines the uncertainties on the fitted matrix elements. The least-squares statistic is defined as

$$S = \frac{1}{N}\left[\sum_{i=1}^{N_{\mathrm{exp}}} w_i \sum_{k=1}^{N_{\gamma(i)}} \left(\frac{C_i Y_k^{\mathrm{calc}} - Y_k^{\mathrm{exp}}}{\sigma_k}\right)^2 + \sum_{j=1} w_j \sum_{n_j} \left(\frac{d_{n_j}^{\mathrm{calc}} - d_{n_j}^{\mathrm{exp}}}{\sigma_{n_j}}\right)^2 \right.$$
$$\left. + \sum_{k} \left(\frac{Y_k^c}{Y_n^c} - u_{i,\gamma}\right)^2 \frac{1}{u^2(i,\gamma)}\right]$$

where N is the number of data points, N_{exp} is the number of experiments defined in the GOSIA input and $N_{\gamma(i)}$ is the number of γ-ray transitions for experiment i. Y_k represents the γ-ray yield for each measured transition in each experiment i, the superscripts "exp" and "calc" stand for the experimental and calculated values respectively, while σ is the uncertainty on the yield. The weights, w_i, ascribed to the various experiments that are defined, can be set independently by the user. The second summation runs over the number of independent spectroscopic data (γ-ray branching ratios, lifetime values, known matrix elements or mixing amplitudes) where d represents the value and σ represents the uncertainty. The user-defined weights, w_j, are common for a given group of spectroscopic data. The last contribution to the least-squares statistic is related to the user-defined "observation limit". An experiment and detector-dependent upper limit of γ-ray yields, $u_{i,\gamma}$, is expressed as a fraction of the normalization transition which is specified by the user (usually this corresponds to the strongest observed transition, i.e. $2_1^+ \to 0_1^+$ in even-even nuclei). If the calculated yield of any unobserved γ-ray transition, divided by the yield of the normalizing transition, Y_n^c, exceeds the upper limit, then it is included in the calculation of the least-squares statistic S. The last summation extends over the calculated γ-ray transitions which are not defined as experimentally observed, provided that the upper limit has been exceeded. A proper set of upper limits prevents one from finding unphysical solutions yielding production of γ-ray transitions that were not observed in the experiment. The least-squares statistic is very similar to χ^2 with the exception that it is normalized to the total number of data points, instead of the number of degrees of freedom. The number of data points N in this definition takes into account:

- every experimental yield that is provided to gosia as input
- every spectroscopic data point that is included.

This means that if a γ-ray transition is determined in multiple experiments, then all these yields are taken into account in the number of data points. Even data points with an infinite error bar or a user-defined weight of zero in the χ^2 function are included.

Depending on the number of populated levels and the richness of available spectroscopic information, different strategies are used in the analysis of Coulomb-excitation experiments with GOSIA [72]. The strategies that are used for the GOSIA analysis in this thesis are described in detail in Chapter 4.

3 Experimental setup

The Coulomb-excitation experiments described in this thesis were performed at the radioactive ion-beam facility REX-ISOLDE at CERN (Geneva, Switzerland) [73]. The experimental campaign was divided in two parts: a feasibility test was performed with a ^{200}Po beam in 2009. After this successful test the main part of the experimental campaign took place in 2012 when beams of ^{196,198,200,202}Po were produced and post-accelerated to perform the spectroscopic study of these nuclei through Coulomb excitation. This chapter provides the essential information about the beam production, the post-acceleration and the detection setup that was used. More details are provided on a selection of topics that were crucial for the analysis of the data.

3.1 The REX-ISOLDE facility

At the REX-ISOLDE facility, radioactive ion beams are produced with the Isotope Separation On Line (ISOL) technique and can be post-accelerated up to 2.85 MeV/u. A multitude of isotopes are produced by impinging 1.4 GeV protons on a thick UC_x target. The produced isotopes diffuse out of the target, which is kept at a high temperature (T $\approx$ 2000 °C) in order to facilitate the diffusion process and to avoid sticking of atoms to the walls of the target-ion source system. In the Resonant Ionization Laser Ion Source (RILIS) hot cavity the polonium isotopes are resonantly ionized with a three-step laser ionization scheme that ensures the isotopic selection (Z) [74]. After extraction from the target-ion source system by a 30 kV potential, the wanted 1^+-charged isotope is selected by the High Resolution Separator (HRS). The drawback of the high temperature of the target-ion source system is isobaric contamination stemming from surface ionization of elements with a low ionization potential. In this case it gives rise to isobaric contamination from thallium isotopes ($Z = 81$, IP = 6.108 eV) [75]. The average beam intensities and purities, together with other

Table 3.1: Properties of the beams that were used in the experiment. $I_{\mathrm{Po,av}}$ represents the average polonium beam intensity measured at the Miniball setup. The purity P is defined as the fraction of polonium isotopes in the beam and was determined using the scattered particles on the DSSSD (see below) during laser ON/OFF runs. θ_{CM} represents the range in centre-of-mass scattering angle that was covered and T_{exp} is the total measurement time.

A	$T_{1/2}$ [s]	$I_{\mathrm{Po,av}}$ [pps]	P [%]	Target	θ_{CM} [°]	T_{exp} [min]	Year
196	5.8(2)	$2.3(2).10^4$	59.51(7)	^{104}Pd	66-128	1687	2012
198	106(2)	$4.6(7).10^4$	95.97(19)	^{94}Mo	66-128	1235	2012
200	691(5)	$2.54(17).10^5$	97.90(4)	^{104}Pd	77-136	2424	2009
202	$26.8(2).10^2$	$6.6(7).10^4$	98.3(2)	^{104}Pd	66-128	196	2012
202	$26.8(2).10^2$	$4.6(9).10^4$	98.1(2)	^{94}Mo	66-128	170	2012

relevant properties, are summarized in Table 3.1. The average intensity of the beam at Miniball is extracted by using the known cross section for Coulomb excitation of the target. Section 3.2.3 explains in detail how the purity of the beam was extracted.

The low-energetic, isobaric and singly-charged beam, containing the polonium isotope of interest together with the thallium contamination, is then fed to the REX postaccelerator [73]. First, the beam is injected into a Penning trap (REXTRAP) to cool and bunch the continuous beam. The bunches are then charge bred in the Electron Beam Ion Source (EBIS) to transform the 1^+ ions to 48^+ ions (49^+ in the case of ^{202}Po) to make the post-acceleration process more efficient. After passing another analyzing magnet the ions are post-accelerated to 2.85 MeV/u by the REX linear accelerator and finally delivered at the Miniball detection setup [76].

3.2 The Miniball detection setup

A secondary thin target is placed in the middle of the Miniball target chamber to induce Coulomb excitation. Two different targets were used during the experiments for this thesis: a 2.0 mg/cm^2 thick ^{104}Pd target for the measurements on ^{196,200,202}Po and a 2.0 mg/cm^2 thick ^{94}Mo target for the measurements on ^{198,202}Po. The beam energy for each projectile-target combination was well below the “safe value” (see equation 2.2) ensuring a purely electromagnetic interaction between the colliding nuclei. States up to 4_1^+ and

2_2^+ were populated. The choice of the respective target for each isotope (see Table 3.1) was made based on a comparison of the γ-ray energies de-exciting the 2_1^+ states in beam and target, to avoid an overlap, and on the excitation probability of the target nucleus. The scattered particles are detected with a double-sided-silicon-strip detector (DSSSD) which is also mounted in the target chamber and is divided into 24 secular strips and sixteen annular strips to ensure position sensitivity. The distance between target and DSSSD was 32.5 mm during the experiment in 2009 and 26.5 mm in 2012, yielding an angular coverage of $15.5° < \theta_{\mathrm{LAB}} < 51.6°$ and $18.8° < \theta_{\mathrm{LAB}} < 57.1°$ respectively. The γ rays are detected with the Miniball γ-ray detector array that surrounds the target chamber in close geometry. The Miniball detector array consists of eight cluster detectors of which only seven were operational during both experimental campaigns. Each cluster contains three individually encapsulated HyperPure Germanium (HPGe) crystals which are in turn divided, by segmentation of the outer electrode, into six segments and a central electrode. The high granularity of the Miniball detectors assures position sensitivity for the γ-ray detection as well.

3.2.1 Absolute efficiency of the Miniball γ-ray detector

A combination of a ^{152}Eu and ^{133}Ba calibration source is used to determine the absolute detection efficiency of Miniball over the full relevant energy range. The ^{133}Ba source is added because of three low-energy transitions (at 53.161(1) keV and a doublet at 80.9(3) keV) in order to ensure a good description of the absolute photon detection efficiency in the polonium X-ray region. A list of absolute detection efficiencies at various energies, ranging from 40 keV (the europium K_α X-ray energy) to 1408 keV, is extracted by employing the coincidence method described in reference [77]. An absolute efficiency curve is then obtained by fitting the absolute efficiency points with their corresponding error bars to the function

$$\varepsilon\left(E\right) = \exp\left(\sum_{i=0}^{4} p_i \log\left(\frac{E}{E_0}\right)^i\right) \tag{3.1}$$

where ε is the absolute detection efficiency at energy E in keV and p_i are the parameters of the fit. The factor E_0 is included to decrease the relative error on the offset parameter p_0 by bringing the “zero point” (the intercept with the vertical axis) closer to the data points. The value that is chosen for E_0 does not influence the relative error on the absolute efficiency if E_0 is chosen in a reasonable way, i.e. somewhere in the range of the data points. The propagated error on the absolute efficiency at a certain energy E includes the uncertainty on the fit parameters and the correlation between the different parameters of the fit.

Table 3.2: Absolute γ-ray detection efficiencies in the relevant energy range for the analysis of the Coulomb-excitation experiments analyzed in this thesis, together with the extracted uncertainty. The absolute efficiencies for both experimental campaigns are listed: ε_{2009} and ε_{2012} are the absolute efficiencies for the 2009 and 2012 campaign respectively.

E [keV]	ε_{2009}	ε_{2012}
80	0.189(8)	0.177(5)
200	0.176(3)	0.181(4)
500	0.1093(2)	0.111(2)
1000	0.0769(4)	0.080(2)

In general, the total propagated error bar of a function f that depends on n parameters x_i is calculated as

$$\Delta f = \sqrt{\sum_{i=1}^{n}\sum_{j=1}^{n}\left[\frac{\partial f}{\partial x_i}\frac{\partial f}{\partial x_j}\mathrm{cov}(x_i, x_j)\right]} \tag{3.2}$$

where $\mathrm{cov}(x_i, x_j)$ is the covariance between parameters x_i and x_j, with $\mathrm{cov}(x_i, x_j) = \sigma_i$ when $i = j$ (with σ_i the uncertainty on parameter p_i). Applying this to the function describing the efficiency in equation 3.1, leads to the following expression for the total propagated error on the absolute efficiency at energy E:

$$\Delta\varepsilon = \varepsilon\left(E\right)\sqrt{\sum_{i=0}^{4}\sum_{j=1}^{4}\left[\log\left(\frac{E}{E_0}\right)^{i}\log\left(\frac{E}{E_0}\right)^{j}\mathrm{cov}(p_i, p_j)\right]}. \tag{3.3}$$

The resulting absolute-efficiency curve, extracted for the data in 2012, is shown in Figure 3.1 together with the data points from the ^{133}Ba and ^{152}Eu source and the extracted total error. Throughout the relevant energy range the relative error on the absolute efficiency, $\Delta\varepsilon/\varepsilon$, is almost constant as can be seen on panel B of Figure 3.1. The absolute-efficiency curve extracted for the 2009 data looks similar. A list of absolute detection efficiencies in the relevant energy range for the Coulomb-excitation experiments is shown in Table 3.2, for the experimental campaigns of 2009 and 2012.

3.2.2 Data taking at Miniball

At Miniball, particle-γ ray coincidences (“p-γ events”) are essential to select the physically interesting events (Coulomb-excitation events) among the background

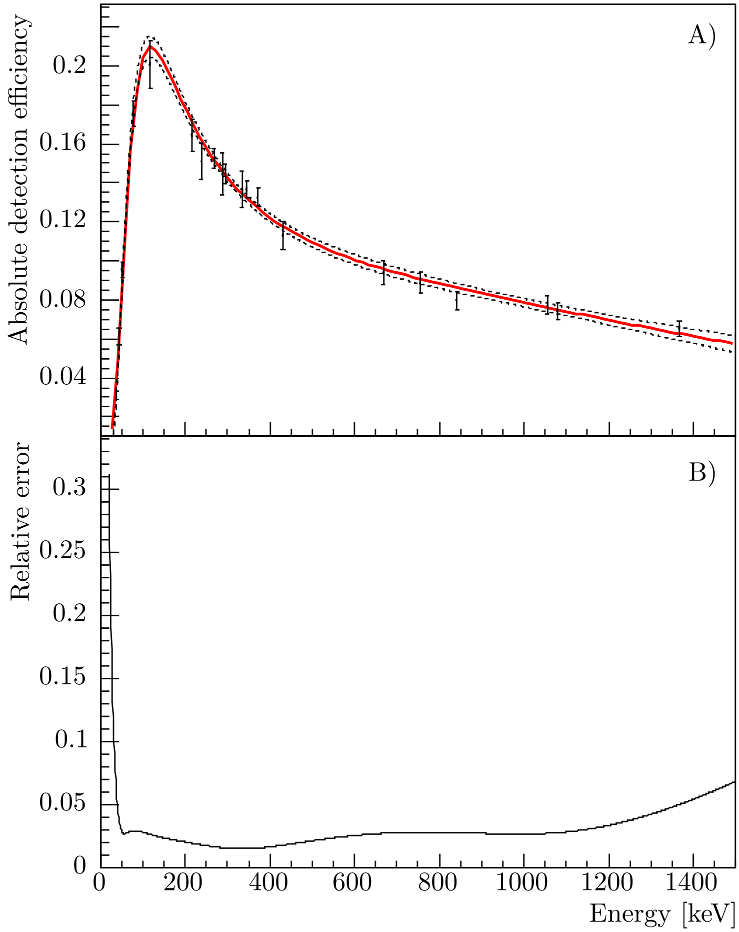

Figure 3.1: A) Absolute photon detection efficiency ε as a function of energy E in keV, extracted for the experimental campaign in 2012. The experimental data points, extracted from a combination of a ^{133}Ba and ^{152}Eu calibration source, are shown in black with the deduced uncertainty. The curve in red shows the absolute detection efficiency, the lower and upper error on the absolute efficiency are shown with black dashed lines. B) Relative error $\Delta\varepsilon/\varepsilon$ on the absolute detection efficiency as a function of the energy in keV. The relative error is extracted employing equation 3.3.

radiation. The γ-ray background originates from room background, decay radiation from the radioactive beam and X rays from the accelerator while the particle background is essentially due to the elastic scattering process. Therefore a specific coincidence scheme is developed for the data system (see Fig. 16 of [76]). A 800 ns wide coincidence gate is defined for each γ ray that is detected in the Miniball array. Particles that are detected within this window are considered as coincident with the γ ray and treated as p-γ events. In case of high beam intensities at the Miniball secondary target, the particles that do not fall inside the 800 ns coincidence gate can be downscaled. This means that all the coincident particles are registered, but only 1 in 2^N particles without coincident γ ray is accepted (with N the downscaling factor), thus reducing the dead time of the particle-detection electronics due to elastically scattered particles. This downscaling method was applied for all polonium isotopes (with downscaling factor $N = 4$) but ^{196}Po, where the beam intensity was significantly lower (see Table 3.1). However, during the 2012 experimental campaign the p-γ coincidence gate was not set correctly for two of the four quadrants of the DSSSD. This gave rise to downscaling of the p-γ coincidences instead of the particles without coincident γ rays for half of the data.

Still within the 800 ns coincidence gate around the γ ray, some of the p-γ events are "true" coincidences while others are random coincidences giving rise to background. The Coulex events are selected among this background by applying a selection based on the kinematic and timing properties of the particles and γ rays. The procedure is explained in the next sections. Next to that, the specific logic of the analysis codes is explained in detail. The logic is designed carefully to assure a correct background subtraction. This is especially crucial for a correct determination of the number of X rays as there is a lot of background in the X-ray region.

Selection of events based on kinematic properties

As the influence of the excitation on the scattering process is negligible (see section 2.1.1), the kinematics of the reaction can be studied in a classical way, including the effect of energy loss in the target. In order to ensure a good Doppler correction of the Doppler broadened γ-ray energies, a correct identification of the scattering partners in the collision is crucial. Simulations of the reaction kinematics show that the lighter scattering partner, the target nucleus in the case of inverse kinematics, is scattered throughout the entire detection range of the particle detector. The trajectory of the heavier partner, the projectile nucleus, is not changed as drastically as that of the target nucleus. As a consequence, the projectile nuclei are detected only at small laboratory scattering angles.

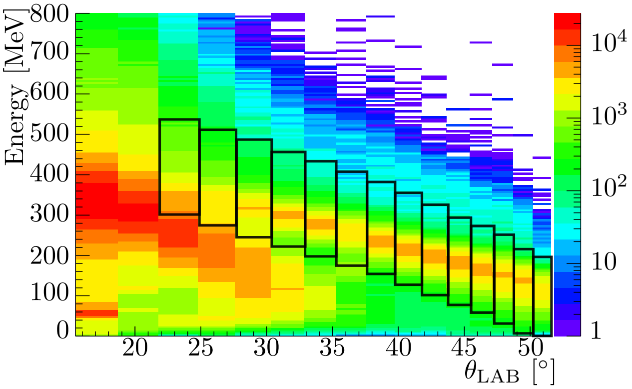

Figure 3.2: Particle energy versus scattering angle in the laboratory frame of reference for ^{200}Po on ^{104}Pd. The color scale on the vertical axis represents the number of counts in each bin. Only particles that are coincident with at least one γ ray are shown. The gates to select the ^{104}Pd recoil are shown in black. The two innermost strips are not taken into account as it is not possible to distinguish between the beam and the recoil particles there.

The recoiling target atoms (further called "recoils") therefore provide an excellent probe to "scan" the range of the particle detector. Good p-γ events (based on kinematic properties) are selected by demanding the detection of a recoil in the DSSSD. The corresponding γ-ray energy can then be Doppler corrected with the knowledge that the detected particle was a target nucleus. In principle, the opposite procedure, following the scattered projectile nuclei through the DSSSD, is also possible. However, the correct particle identification is more difficult giving rise to a Doppler correction of poorer quality.

The detected particle energy in the DSSSD as a function of the scattering angle in the laboratory frame of reference for ^{200}Po on ^{104}Pd is shown in Figure 3.2. As explained before, a distinction is made between a beam particle and a recoil, based on the energy-versus-scattering angle characteristics. Detected particles in the DSSSD related to the scattering of beam on target are selected by "following" the recoils through the range of the DSSSD. For each isotope that was studied in this thesis, specific E-versus-θ gates were adopted to select the recoils scattered in the particle detector. As an example, the gates that were used for ^{200}Po on ^{104}Pd can be seen in Figure 3.2. The two innermost strips of the particle detector were excluded from the analysis because in this region of the detector, the beam and recoil particles are not separable. The range of centre-of-mass scattering angles that was covered by applying this method is

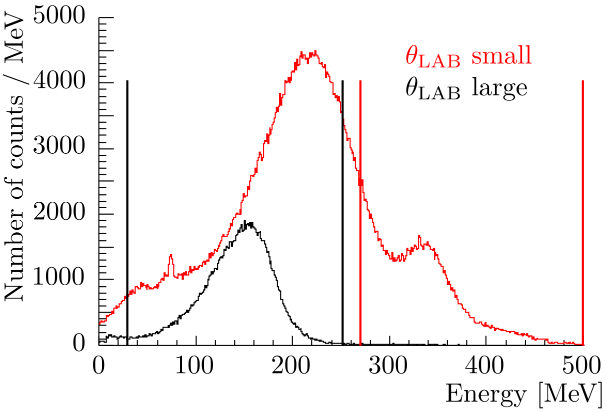

Figure 3.3: Detected energy of the particles scattered in the DSSSD at small laboratory scattering angles ($24.8° < \theta_{\rm LAB} < 27.5°$) in red and at large laboratory scattering angles ($47.1° < \theta_{\rm LAB} < 48.7°$) in black. The data shown here are the 2009 data of ^{200}Po scattered on a ^{104}Pd target. The gates that were used to select the recoil particle are illustrated with solid lines, in black for the large scattering angles and in red for the small scattering angles.

shown for each reaction in Table 3.1.

At large scattering angles in the laboratory frame, the recoil peak is easily selected. However, at small laboratory angles, the recoil and projectile peak overlap in energy. This difference is clear from Figure 3.3, where the detected particle energy is shown for small and large scattering angles. At large $\theta_{\rm LAB}$, it is relatively easy to choose gates, making sure that the total recoil-particle peak is included. The doubly-peaked structure at small values of $\theta_{\rm LAB}$ complicates the selection of the recoiling particle. The way that the gates are chosen (as shown in Figures 3.2 and 3.3 for the 2009 data of ^{200}Po on ^{104}Pd), has two consequences. The first is that at small values of $\theta_{\rm LAB}$, a contribution of the projectile peak is included in the gate. This does not cause a problem however, as the Doppler correction for these events will be wrong. Indeed, it is wrong to assume for these events that the recoil is detected in the DSSSD. A faulty Doppler correction removes the γ-ray energies from the central peak and only contributes to the background. A second consequence of the applied gates is that at small $\theta_{\rm LAB}$, not all recoils are included in the gate. As the Coulomb-excitation data of the projectile is analyzed relatively to the Coulomb-excitation data of the target, this also does not harm the analysis. Indeed, the projectile Coulex cross section is normalized to the target Coulex cross section. In both

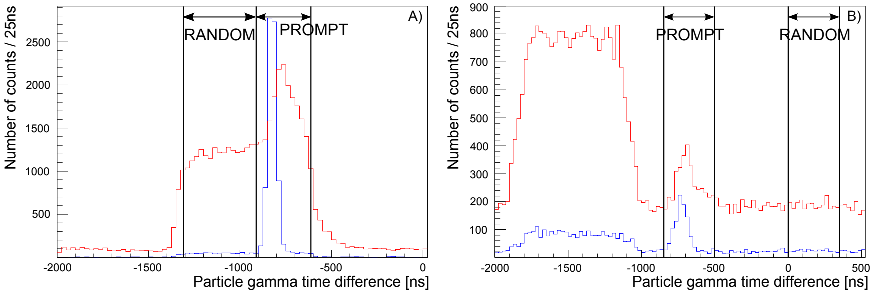

Figure 3.4: Time difference between particle and γ ray, gated on the polonium $2_1^+ \to 0_1^+$ γ-ray transition in blue and gated on polonium X rays in red. The prompt and random coincidence windows that were used are shown in black. A) Sum of particle-γ ray timing information of all quadrants (2009 data of ^{200}Po on ^{104}Pd). B) Particle-γ ray timing information for quadrants 1 and 2 where the downscaling was not properly set (2012 data of ^{198}Po on ^{94}Mo).

cases, exactly the same kinematic selection rules are applied.

Selection of events based on timing properties

A second selection that is applied to the detected events, is a selection based on timing properties. The "true" particle-γ ray coincidences represent the inelastic scattering events where the detected γ ray is truly correlated to the detected particle. Random coincidences between an elastically scattered particle and a background γ ray (originating from decay radiation of the radioactive ion beam, room background or X rays from the accelerator) also occur, giving rise to background p-γ events. The true p-γ events are said to be in "prompt" coincidence with each other while the background consists of "random" p-γ coincidences. As the flow of background radiation is constant in time, the random p-γ events constitute a constant background which needs to be subtracted from the prompt events.

Figure 3.4 shows the time difference between a particle and a γ ray that were detected during the Coulomb-excitation experiments of ^{200}Po on ^{104}Pd in panel A and ^{198}Po on ^{94}Mo in panel B. The different structure of the data on ^{198}Po can be explained by the problem with the downscaling in 2012 as explained earlier. In the "normal" situation of the 2009 data, none of the events in the prompt peak are downscaled. However the mistake in the settings for the p-γ coincidence window in 2012 gave rise to the downscaling of the prompt p-γ

Table 3.3: Definition of prompt and random windows used for the different experiments. Q_i denotes the ith quadrant of the DSSSD. The problem with the downscaling technique occurred in 2012 in quadrants 1 and 2. p/r is the scaling factor that was used to scale the random events before subtracting them from the prompt events.

Year	Q_1 and Q_2		Q_3 and Q_4		p/r
	Prompt [ns]	Random [ns]	Prompt [ns]	Random [ns]	
2012	$[-850, -500]$	$[0, 350]$	$[-900, -550]$	$[-1250, -900]$	1
2009	$[-915, -615]$	$[-1315, -915]$	$[-915, -615]$	$[-1315, -915]$	0.75

events. This leads to a significant loss of useful data for these two quadrants of the DSSSD.

A difference in time behavior is observed between the Coulomb-excitation γ rays (de-exciting the 2_1^+ state in the polonium isotope) and the low-energy polonium X rays. This is due to the energy dependence of the response of the Ge detectors which leads, for the X rays, to a shift of the centroid and a broadening. The prompt particle-γ ray coincidence window is defined broad enough to include the slower charge collection of the low-energetic X rays. Random p-γ coincidences are selected in a second time window. In the normal case of the 2009 data on ^{200}Po, the random window is chosen within the region where the events are not downscaled. This allows to scale the prompt and random events using the difference in length of the two respective windows. The data with the wrongly downscaled events were treated in a slightly different way. As the prompt p-γ events fall inside the downscaled region in this case, the random window is also selected among the downscaled events. Details on the prompt and random windows that were used for all isotopes can be found in Table 3.3.

Finally, it is also possible to have p-$\gamma\gamma$ events, in which a particle is coincident with two γ rays in a cascade. Based on the $\gamma\gamma$ timing spectra, a 350 ns coincidence window is defined for the coincidences between two γ rays. These p-$\gamma\gamma$ events will be useful to clear up the Coulex γ-ray spectra as shown in Chapter 4.

Logic of data sorting

The raw data collected by the particle and γ-ray detectors is transformed into a Coulex γ-ray energy spectrum in three steps of which Figure 3.5 shows a schematic flowchart. Events are created by the event builder in the first step of

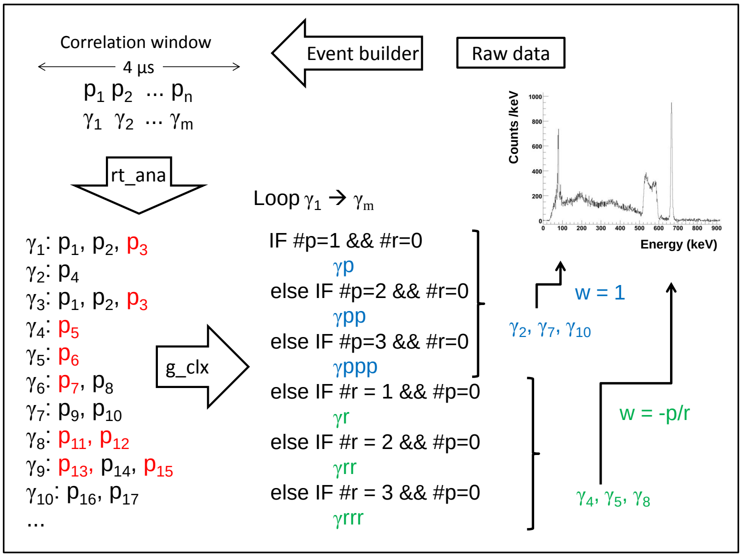

Figure 3.5: Schematic flowchart of the logic of the data sorting that is applied. The raw data is translated into histograms in .root files through the event builder, the rt_ana code and finally the g_clx code. The particles (represented as p_i) in black (red) are in prompt (random) coincidence with the γ ray (represented as γ_i). In the last step, the blue events are prompt p-γ coincidences which are the interesting Coulex events. The events in green are random p-γ coincidences and thus treated as background. The weight with which the events are added in the final Coulex spectrum, is given by the factor w.

the process. A $4\,\mu$s correlation window is opened by a particle and contains all the particles and γ rays that are detected within $4\,\mu$s after the detection of the first particle. At this stage, each event contains a list of coincident particles and γ rays. $\gamma\gamma$ coincidences have to be treated at this moment in the data-treatment process as the γ rays will be stored independently from the next step onwards.

The rt_ana code treats every detected γ ray independently and pairs them with the respective coincident particles. Each particle is being labeled as prompt (particles in black in Figure 3.5) or random (particles in red in Figure 3.5) based on the selection rules shown in Table 3.3. Notice that p-$\gamma\gamma$ events are split up into two entries, e.g. γ_1 and γ_3 in Figure 3.5. In the last step, the g_clx code loops over all the detected γ rays and decides whether or not to include them in the final Coulex spectrum. In order to perform a correct background subtraction, only the “purely prompt” and “purely random” events are included, i.e. the events with only prompt or random particles respectively. The majority of the events, ranging from 95.5 % of the ^{202}Po events to 97.1 % of the ^{196}Po events, are pure so only a fraction of the events is disregarded in this way. The prompt p-γ events (the blue events in Figure 3.5) are included in the Coulex spectrum with weight $w = 1$ while the random events (the green events in Figure 3.5) are given a weight factor of $w = -p/r$, where p and r are the lengths of the prompt and random coincidence windows respectively. The scaling factor $-p/r$ takes into account the lengths of the prompt and random time windows, which are defined in Table 3.3.

3.2.3 Determination of beam purity

The purity of the beam is extracted based on data acquired when the laser ON/OFF mode was applied. In this mode the laser ionization is switched periodically on and off using the supercycle of the Proton Synchrotron Booster as the time base for the periodicity. Data, acquired in this way, contains an equal measurement time and conditions with the lasers switched on (thus resonantly ionizing polonium plus the isobaric contaminant thallium) as with the lasers blocked (only the isobaric contaminant thallium in the beam). During the laser ON/OFF runs the purity of the beam can be determined exactly. A comparison of the number of scattered particles on the DSSSD during the laser ON and laser OFF periods, taking into account the difference in Rutherford cross section for polonium ($Z = 84$) and thallium ($Z = 81$), renders the purity P of the beam [67]:

$$P = \frac{1}{r_{\mathrm{ON/OFF}} + 1} \tag{3.4}$$

where

$$r_{\mathrm{ON/OFF}} = \frac{I_{\mathrm{Tl}}}{I_{\mathrm{Po}}} = \frac{\sigma_{\mathrm{Po}}}{\sigma_{\mathrm{Tl}}} \frac{1}{\frac{N_{\mathrm{ON}}^{\mathrm{DSSSD}}}{N_{\mathrm{OFF}}^{\mathrm{DSSSD}}} - 1} \tag{3.5}$$

where $\frac{\sigma_{\mathrm{Po}}}{\sigma_{\mathrm{Tl}}} = \left(\frac{Z_{\mathrm{Po}}}{Z_{\mathrm{Tl}}}\right)^2$ is the ratio of the Rutherford cross section of Po to Tl on the respective target and $N_{\mathrm{ON(OFF)}}^{\mathrm{DSSSD}}$ is the number of scattered particles on the DSSSD when the lasers are switched ON(OFF). I_{Tl} gives the beam intensity of the thallium contaminant which is incident on the secondary Miniball target while I_{Po} represents the incident polonium beam intensity, both in the laser ON periods of the laser ON/OFF runs and expressed in particles per second. The beam purities for the experiments with ^{198,200,202}Po, listed in Table 3.1, have been acquired this way.

As the thallium contaminant was substantial at mass 196, the data on ^{196}Po is treated in a more detailed way. Data was taken in laser ON/OFF mode regularly during the ^{196}Po experiment. The average beam purity during these runs can be extracted using equations 3.4 and 3.5, giving $\mathrm{P}_{\mathrm{ON/OFF}} = 59.51(7)\,\%$. In between the laser ON/OFF runs, laser ON runs were also performed to gain statistics on the Coulomb excitation of ^{196}Po. Fluctuations in laser power and ionization efficiency can cause the beam purity to shift throughout the experiment. The beam purity can thus not simply be assumed to remain constant during the laser ON runs. A comparison of the intensity of the γ-ray transitions following Coulomb excitation of ^{196}Po and ^{196}Tl is used to deduce the r_{ON} factor during a laser ON run, which can be translated into the beam purity P using equation 3.4 and is defined as [67]:

$$r_{\mathrm{ON}} = \frac{N^{\mathrm{Tl}}_{\gamma,\mathrm{ON}}}{N^{\mathrm{Po}}_{\gamma,\mathrm{ON}}} \cdot \frac{\sigma_{\mathrm{Po}}\varepsilon_{\mathrm{MB,Po}}}{\sigma_{\mathrm{Tl}}\varepsilon_{\mathrm{MB,Tl}}} \tag{3.6}$$

where $N^{\mathrm{Tl(Po)}}_{\gamma,\mathrm{ON}}$ is the intensity of the γ-ray transition after Coulomb excitation of ^{196}Tl ($1^- \rightarrow 2^-$ at 253 keV) and ^{196}Po ($2^+_1 \rightarrow 0^+_1$ at 463 keV) respectively and $\varepsilon_{\mathrm{MB,Tl(Po)}}$ is the absolute detection efficiency of the Miniball detector array at the respective de-excitation energy in ^{196}Tl (^{196}Po). The ratio of the cross section for Coulomb excitation to the populated state in ^{196}Po and ^{196}Tl, $\frac{\sigma_{\mathrm{Po}}}{\sigma_{\mathrm{Tl}}}$, is unknown because of the unknown matrix elements coupling the ground state to the populated state in these isotopes. As the beam purity of the laser ON/OFF runs can be extracted with the two described methods (equation 3.5 and equation 3.6), the unknown ratio can be determined using the result for $r_{\mathrm{ON/OFF}}$, demanding the two methods to give consistent results. That way, the beam purity during the laser ON runs is determined by scaling to the result obtained with the laser ON/OFF data. The obtained result, $\mathrm{P}_{\mathrm{ON}} = 46\,\binom{6}{4}\,\%$ has a larger relative error bar compared to the result from the laser ON/OFF data. This is due to the limited statistics in the Coulex lines compared to the number of particles scattered on the DSSSD.

Figure 3.6 shows the evolution of the beam purity during the experiment on ^{196}Po. This graph shows the extracted beam purities (using equation 3.5 for laser ON/OFF runs and equation 3.6 for laser ON runs) for every run, together with the average beam purities for the laser ON/OFF runs and laser ON runs separately. The average quality of the ^{196}Po beam was better during the laser ON/OFF runs then during the laser ON runs, which is reflected in a significantly higher average beam purity for the laser ON/OFF runs. The detailed information on the evolution of the beam purity is not needed for the analysis of the total spectra, only a time-integrated value is essential. The measuring time and statistics acquired during the different runs is included in the average values for the beam purity.

The resulting beam purity is taken into account in the determination of the intensity of the de-excitation γ-ray transition in the target. As both the polonium

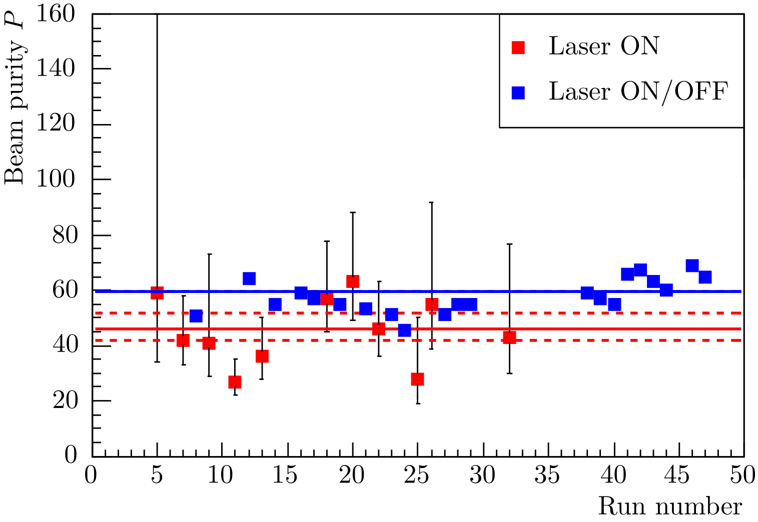

Figure 3.6: Beam purity P in percentage as a function of run number, showing all the runs performed on the Coulomb excitation of ^{196}Po on ^{104}Pd. The blue squares show the beam purity during laser ON/OFF runs, while the red squares represent the beam purity, extracted during the laser ON runs. The blue line shows the average beam purity for all laser ON/OFF runs (error bar is smaller than the width of the line). The average beam purity during the laser ON runs is depicted by the red line, with upper and lower error bar in dashed lines.

isotope and the thallium contaminant that are present in the beam can excite the target, the beam purity is employed to calculate the target excitation yield caused by the polonium isotope:

$$I^T_{Po} = I^T_{Total} \cdot P \tag{3.7}$$

where I^T_{Total} is the total intensity of the target de-excitation γ ray, I^T_{Po} is the intensity of the target de-excitation caused by the polonium nuclei in the beam and P is the extracted beam purity. The target excitation yields for the ^{196}Po data are extracted separately for the laser ON/OFF data and the laser ON data, taking into account the respective beam purity.

4 Coulomb excitation of ^{196,198,200,202}Po

The data analysis, analysis using GOSIA and results of the two Coulomb-excitation campaigns performed at the REX-ISOLDE facility in CERN, were submitted for publication in Physical Review C. The full text of this paper is the main part of this chapter. Next to that, additional details related to the data and GOSIA analysis are provided.

4.1 Deformation and mixing of co-existing shapes in neutron-deficient polonium isotopes: submitted for publication in *Physical Review C*

Deformation and mixing of co-existing shapes in neutron-deficient polonium isotopes

N. Kesteloot[1,2], B. Bastin[1,3], K. Auranen[4,5], C. Bauer[6], M. Bender[7,8], V. Bildstein[9], A. Blazhev[10], S. Bönig[6], N. Bree[1], E. Cléement[3], T.E. Cocolios[1,11,12], A. Damyanova[13], I. Darby[1,4,5], H. De Witte[1], D. Di Julio[14], J. Diriken[1,2], C. Fransen[10], L.P. Gaffney[1,15], J.E. García-Ramos[16], R. Gernhäuser[9], T. Grahn[4,5], P.-H. Heenen[17], H. Hess[10], K. Heyde[18], M. Huyse[1], J. Iwanicki[19], U. Jakobsson[4,5], J. Konki[4,5], T. Kröll[6], B. Laurent[20], N. Lecesne[3], R. Lutter[21], J. Pakarinen[4,5], P. Peura[4,5], E. Piselli[11], L. Próchniak[19], P. Rahkila[4,5], E. Rapisarda[1,11], P. Reiter[10], M. Scheck[6,15,22,23], M. Seidlitz[10], M. Sferrazza[24], B. Siebeck[10], M. Sjodin[3], H. Tornqvist[11], E. Traykov[3], J. Van De Walle[11], P. Van Duppen[1], M. Vermeulen[25], D. Voulot[11], N. Warr[10], F. Wenander[11], K. Wimmer[9], K. Wrzosek-Lipska[1,19] and M. Zielińska[19,20]

[1] *KU Leuven, Instituut voor Kern- en Stralingsfysica, B-3001 Leuven, Belgium*
[2] *Belgian Nuclear Research Centre SCK•CEN, B-2400 Mol, Belgium*
[3] *GANIL CEA/DSM-CNRS/IN2P3, Boulevard H. Becquerel, F-14076 Caen, France*
[4] *University of Jyväskylä, Department of Physics, P.O. Box 35, FI-40014 Jyväskylä, Finland*
[5] *Helsinki Institute of Physics, PO Box 64, FI-00014 Helsinki, Finland*
[6] *Institut für Kernphysik, Technische Universität Darmstadt, D-64289 Darmstadt, Germany*
[7] *Université Bordeaux, Centre d'Etudes Nucléaires de Bordeaux Gradignan, UMR5797, F-33175 Gradignan, France*
[8] *CNRS/IN2P3, Centre d'Etudes Nucléaires de Bordeaux Gradignan, UMR5797, F-33175 Gradignan, France*
[9] *Physics Department E12, Technische Universität München, D-85748 Garching, Germany*
[10] *Institut für Kernphysik, Universität zu Köln, 50937 Köln, Germany*
[11] *ISOLDE, CERN, CH-1211 Geneva 23, Switzerland*
[12] *School of Physics & Astronomy, The University of Manchester, Manchester, M13 9PL, United Kingdom*
[13] *Université de Genève, 24, Quai Ernest-Ansermet, CH-1211 Genève 4, Switzerland*
[14] *Physics Department, University of Lund, Box 118, SE-221 00 Lund, Sweden*
[15] *Oliver Lodge Laboratory, University of Liverpool, Liverpool L69 7ZE, United Kingdom*
[16] *Departamento de Física Aplicada, Universidad de Huelva, 21071 Huelva, Spain*
[17] *Physique Nucléaire Théorique, Université Libre de Bruxelles, B-1050 Bruxelles, Belgium*
[18] *Department of Physics and Astronomy, Ghent University, Proeftuinstraat 86, B-9000 Gent, Belgium*
[19] *Heavy Ion Laboratory, University of Warsaw, PL-02-093 Warsaw, Poland*
[20] *IRFU/SPhN, CEA Saclay, F-91191 Gif-sur-Yvette, France*
[21] *Ludwig-Maximilians-Universität-München, Schellingstraße 4, 80799 München, Germany*
[22] *School of Engineering, University of the West of Scotland, Paisley PA1 2BE, United Kingdom*
[23] *SUPA, Scottish Universities Physics Alliance, Glasgow G12 8QQ, United Kingdom*
[24] *Département de Physique, Faculté des Sciences, Université Libre de Bruxelles (ULB), Boulevard du Triomphe, 1050 Brussels, Belgium*
[25] *Department of Physics, The University of York, York YO10 5DD, United Kingdom*

(Submitted 19 January 2015)

Abstract

Coulomb-excitation experiments were performed with post-accelerated beams of neutron-deficient ^{196,198,200,202}Po isotopes at the REX-ISOLDE facility. A set of matrix elements, coupling the low-lying states in these isotopes, was extracted. In the two heaviest isotopes, ^{200,202}Po, the transitional and diagonal matrix element of the 2_1^+ state were determined. In ^{196,198}Po multi-step Coulomb excitation was observed, populating the $4_1^+, 0_2^+$ and 2_2^+ states. The experimental results were compared to the results from the measurement of mean-square charge radii in the polonium isotopes, confirming the onset of deformation from ^{196}Po onwards. Three different model descriptions were used to compare to the data. Calculations with the beyond-mean-field model, the interacting boson model and the general Bohr Hamiltonian model show partial agreement with the experimental data. Finally, calculations with a phenomenological two-level mixing model hint towards mixing of a spherical structure with a weakly-deformed rotational structure.

PACS numbers: 25.70.De,23.20.Js,23.20.-g,25.60.-t

I. INTRODUCTION

Nuclear shape coexistence is the remarkable phenomenon in which states at similar excitation energy exhibit a different intrinsic deformation. By now it is established to appear throughout the whole nuclear landscape, in light, medium and in heavy nuclei [1]. A substantial amount of data has been gathered in the neutron-deficient lead region, providing clear evidence for the coexistence of shapes in these nuclei from an experimental as well as a theoretical point of view. Experimentally, shape coexistence is well established in the mercury isotopes ($Z = 80$) around neutron mid-shell, e.g. the large odd-even staggering and large isomer shift in the measured charge radii [2]. Despite the relatively constant behavior of the 2_1^+ energy and of the reduced transition probabilities $B(E2; 2_1^+ \to 0_1^+)$, a recent Coulomb-excitation study of the neutron-deficient, even-even $^{182-188}$Hg isotopes led to the interpretation of mixing between two different structures that coexist at low excitation energy [3]. Mixing between a weakly-deformed oblate-like band and a more-deformed prolate-like band is proposed to gain importance when going towards neutron mid-shell nuclei. This mixing between two configurations is also predicted in recent theoretical efforts studying the neutron-deficient mercury isotopes in the framework of the interacting boson model with configuration mixing [4].

The ^{186}Pb nucleus ($Z = 82$) is a unique case of shape coexistence since three 0^+ states with different deformation have been observed within an energy span of 700 keV [5]. Also, many other lead isotopes display signs of shape coexistence [6]. However, the ground states of the neutron-deficient lead isotopes are found to stay essentially spherical while different shapes appear at low excitation energy [7, 8].

In the polonium isotopes, above $Z = 82$, low-lying intruder states have also been identified. Early theoretical studies concluded that the ground state of the heavier $^{194-210}$Po isotopes remains spherical, with the first (oblate-like) deformed ground state appearing in ^{192}Po [9]. A prolate deformation in the ground state was suggested for the lightest polonium isotopes with mass $A \leq 190$. These findings were supported by a series of experimental studies of the polonium isotopes employing a range of techniques that include α-, β- and in-beam γ-decay studies e.g., see Ref. [6, 10]. The intrusion of the deformed state, becoming the ground state, is an unexpected result as in the even-even mercury isotopes, which "mirror" the polonium isotopes with respect to $Z = 82$, the intruding 0^+ deformed state never becomes the ground-state structure.

Recent results from the measurement of changes in mean-square charge radii $\delta\langle r^2\rangle$ in a wide range of polonium isotopes point to an onset of deviation from sphericity around ^{198}Po [8, 11], which is significantly earlier, when going towards lighter mass, than previously suggested e.g. in [6]. Comparison of the mean-square charge radii of the polonium isotopes with their isotones below $Z = 82$ as shown in Figure 4.1, suggests that the deviation from sphericity of the ground state sets in earlier above $Z = 82$ [8]. Extending the results towards the more neutron-deficient radon ($Z = 86$) and radium ($Z = 88$) isotopes could confirm this hypothesis [12]. The platinum isotopes with $Z = 78$ show a similar early, but less pronounced, onset of deviation from sphericity as the polonium isotopes [13, 14].

The band structure of the neutron-deficient even-even polonium isotopes has been studied extensively. The relevant results of these studies are summarized in the energy systematics of $^{190-210}$Po shown in Figure 4.1. Lifetime measurements on ^{194,196}Po [15, 16] and inelastic scattering studies of ^{210}Po [17] provided information on reduced transition probabilities. The level structure of the polonium isotopes was interpreted as an anharmonic vibrator in e.g. [18]. Although vibrational characteristics can be identified in the level systematics of the polonium isotopes, the observation of the downsloping trend of the 0_2^+ states in $^{196-202}$Po is hard to fit into the vibrational picture. Recent literature and theoretical efforts provided more evidence that points toward the importance of intruder structures [9, 16, 19].

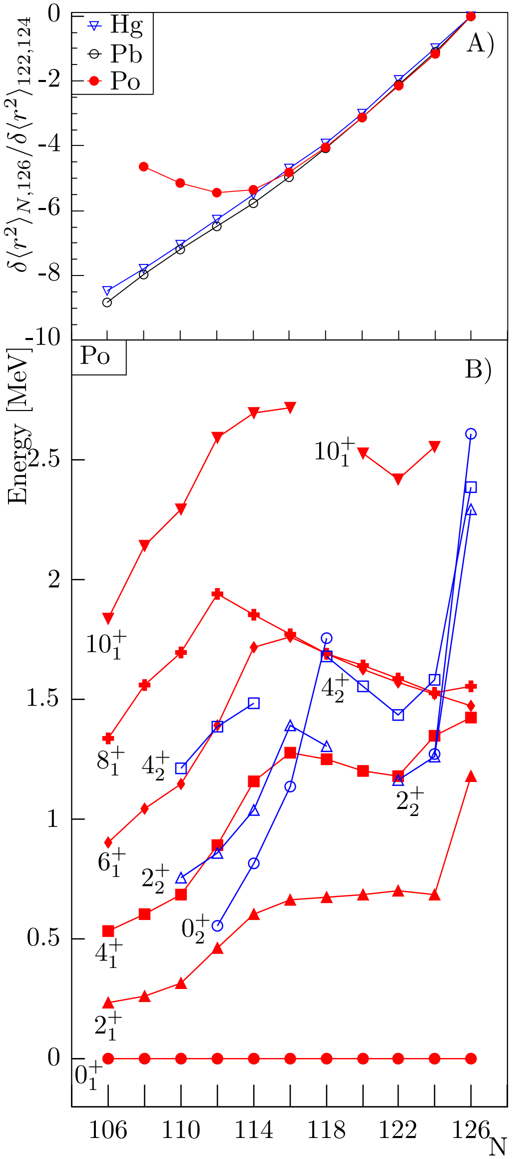

Figure 4.1: (Color online) A) Relative $\delta\langle r^2\rangle$ for the even-A $_{80}$Hg, $_{82}$Pb and $_{84}$Po isotopes [8]. The changes in charge radii, relative to $N = 126$, are normalized to the difference in charge radius between $N = 122$ and 124. B) Energy level systematics of the positive-parity states for the neutron-deficient even-mass polonium isotopes. The full symbols in red show the yrast levels, while the non-yrast levels are indicated with open, blue symbols. Data are taken from Nuclear Data Sheets.

Studies within the interacting boson model point out that the energy systematics in the platinum isotopes conceal the presence of two different structures, which are reproduced with the inclusion of configuration mixing [20]. Also in the polonium isotopes, an increasing admixture of deformed configurations in the ground and isomeric states is proposed based on in-beam, α-decay and lifetime studies [15, 21, 22]. Recent beyond mean-field studies of the polonium isotopes result in potential-energy surfaces that are soft for the heavier polonium isotopes ($A > 198$) pointing toward the possibility of triaxial structures [19].

Theoretical descriptions, such as phenomenological shape-mixing calculations [23-26], contemporary symmetry-guided models [4] and beyond mean-field approaches [19], can reproduce the global trends that are deduced from experiments in the light-lead region. However, more subtle experimental information on the nature of the quadrupole deformation and on the mixing between the co-existing states is missing for most of the isotopes in the region. Coulomb excitation is a unique tool to study nuclear quadrupole deformation in a model-independent way [27]. It provides access to transitional and diagonal matrix elements, which are good fingerprints for shape coexistence [1]. The recent Coulomb-excitation results on $^{182-188}$Hg that were interpreted in the framework of a phenomenological two-level-mixing model provide the first detailed information on mixing in this region [3].

In this paper, we report on two Coulomb-excitation experiments with neutron-deficient $^{196-202}$Po beams, that were performed at the REX-ISOLDE facility at CERN. Part II contains details about the production and post-acceleration of the beams and the specific experimental conditions during the two campaigns. The offline data analysis is described in detail in section III, while section IV elaborates on the analysis using the Coulomb-excitation analysis code GOSIA. In section V the experimental data are compared to different theoretical nuclear models and finally, part VI summarizes and formulates conclusions.

II. EXPERIMENTAL DETAILS

A. Production, post-acceleration and Coulomb excitation of polonium beams at REX-ISOLDE

The radioactive ion beams of polonium were produced and post-accelerated by the REX-ISOLDE facility at CERN [28] during two experimental campaigns in 2009 and 2012. A multitude of isotopes are produced by impinging 1.4 GeV protons, at an average current of 1.6 μA, on a UC$_x$ target. The produced isotopes diffuse out of the target material, which is kept at a high temperature ($T \approx 2000\,^\circ$C) in order to facilitate the diffusion process and to avoid sticking

Table 4.1: Properties of the beams, associated targets, kinematics characteristics and running period of the experiments. $I_{Po,av}$ represents the average polonium beam intensity measured at the Miniball setup. The purity is defined as the fraction of polonium isotopes in the beam and was determined using the scattered particles on the DSSSD during laser ON/OFF runs. θ_{CM} represents the range in centre-of-mass scattering angle that was covered and T_{exp} is the total measurement time.

A	$T_{1/2}$ [s]	$I_{Po,av}$ [pps]	Purity [%]	Target	θ_{CM}[°]	T_{exp} [min]	Year
196	5.8(2)	$2.3(2) \times 10^4$	59.51(7)	^{104}Pd	66-128	1687	2012
198	106(2)	$4.6(7) \times 10^4$	95.97(19)	^{94}Mo	66-128	1235	2012
200	691(5)	$2.54(17) \times 10^5$	97.90(4)	^{104}Pd	77-136	2424	2009
202	$26.8(2) \times 10^2$	$6.6(7) \times 10^4$	98.3(2)	^{104}Pd	66-128	196	2012
202	$26.8(2) \times 10^2$	$4.6(9) \times 10^4$	98.1(2)	^{94}Mo	66-128	170	2012

of ions to the walls of the target-ion source system. In the RILIS hot cavity, the polonium isotopes are resonantly ionized with a three-step laser ionization scheme [29, 30]. After extraction from the target-ion source system by a 30 kV potential, the desired 1^+-charged isotope is selected by the High Resolution Separator (HRS). The high temperature of the target-ion source system induces surface ionization of elements with a low ionization potential, giving rise to isobaric contamination from thallium isotopes ($Z = 81$, IP $= 6.108$ eV) [31]. The average beam intensities and purities are summarized in Table 4.1. The purity of the beam is extracted based on data acquired when the laser ON/OFF mode was applied. In this mode the laser ionization is switched periodically on and off using the supercycle of the Proton Synchrotron Booster, with a typical length of 48 s, as the time base for the periodicity. Data acquired in this way contains an equal measurement time and conditions with the lasers switched on (thus resonantly ionizing polonium) as with the lasers blocked (only the isobaric contaminant thallium in the beam). A comparison of the number of scattered particles on the particle detector inside the target chamber during the laser ON and laser OFF periods of these data, taking into account the difference in Rutherford cross section for polonium ($Z = 84$) and thallium ($Z = 81$), yields the purity of the beam [32, 33]. On average, the beam purity for ^{198,200,202}Po was well above 90 %. Only at mass 196 is the Tl contamination in the beam at the same level as the polonium content.

The low-energetic, isobaric and singly-charged beam, containing the polonium isotope of interest together with the thallium contamination, is then fed into the REX post-accelerator [28]. First, the beam is injected into a Penning trap

(REXTRAP) to cool and bunch the continuous beam. The bunches are then charge bred in the Electron Beam Ion Source (EBIS) to transform the 1^+ ions to 48^+ ions (49^+ in the case of ^{202}Po), with a breeding time of $T = 255\,\text{ms}$. After passing another analyzing magnet the ions are post-accelerated to 2.85 MeV/u by the REX linear accelerator and finally delivered to the Miniball detection setup [34].

A secondary thin target (with a thickness of 2.0 mg/cm^2) is placed in the middle of the Miniball target chamber to induce Coulomb excitation. The beam energy for each projectile-target combination was well below the “safe value” ensuring a purely electromagnetic interaction between the colliding nuclei. States up to 4_1^+ and 2_2^+ were populated. The choice of the respective target for each isotope (see Table 4.1) was made considering the γ-ray energies de-exciting the 2_1^+ states in beam and target, to avoid an overlap, and on the excitation probability of the target nucleus. The scattered particles are detected with a double-sided-silicon-strip detector (DSSSD), which is also mounted in the target chamber and is divided into 48 secular strips, coupled pairwise and read out by 24 ADC channels, and sixteen annular strips to ensure position sensitivity [35]. The distance between target and DSSSD was 32.5 mm during the experiment in 2009 and 26.5 mm in 2012, yielding an angular coverage of $15.5^\circ < \theta_{\text{LAB}} < 51.6^\circ$ and $18.8^\circ < \theta_{\text{LAB}} < 57.1^\circ$ respectively. The γ rays are detected with the Miniball Ge-detector array that surrounds the target chamber in close geometry. The Miniball detector array consists of eight cluster detectors of which only seven were operational during both experimental campaigns. Each cluster contains three individually encapsulated HyperPure Germanium (HPGe) crystals, which are in turn divided by segmentation of the outer electrode into six segments and a central electrode. The high granularity of the Miniball detectors assures position sensitivity for the γ-ray detection as well. A combination of ^{152}Eu and ^{133}Ba calibration sources was used to calibrate in energy and to determine the absolute detection efficiency of Miniball over the entire relevant energy range. Caution was paid to the low-energy range as to ensure a good description of the absolute photon-detection efficiency in the polonium X-ray region [33].

B. Data taking at Miniball

The specific timing properties of REX-ISOLDE beams have an implication on the method of data taking at Miniball. As the beam delivered to the REX linear accelerator is bunched, the RF cavities are not continuously operational. Triggered by the EBIS signal, the linac is switched on during an active window with a length of 800 μs and 1 ms for the 2009 and 2012 experiment respectively. During the full 800 μs/1 ms window, the Miniball data system acquires all the information in the γ-ray and particle detectors. This window is called the “beam-on” window. To ensure a correct identification of all possible sources of background, during an equally long "beam-off" window the data acquisition system is turned on, $4 - 10\,\mathrm{ms}$ after the "beam-on" window, when no beam is coming from the linear accelerator.

Coincidences between a particle and a γ ray ("p-γ coincidences") are essential to select the interesting events (Coulomb-excitation events) among the background radiation. The γ-ray background originates from room background, decay radiation from the radioactive beam and X rays from the accelerator while the particle background is essentially due to the elastic scattering process. Therefore a specific coincidence scheme is developed for the data system (see Figure 16 of [34]). A $800\,\mathrm{ns}$ wide coincidence gate is defined about each γ ray that is detected in the Miniball array. Particles that are detected within this window are considered as coincident with the γ ray and treated as p-γ events. In case of high beam intensities at the Miniball secondary target, the particles that do not fall inside the $800\,\mathrm{ns}$ coincidence gate can be downscaled. This means that all the coincident particles are registered, but only 1 in 2^N particles with a γ ray outside of the coincidence gate is accepted (with N the downscaling factor), thus reducing the dead time of the particle-detection electronics due to elastically scattered particles. This downscaling method was applied for all polonium isotopes (with downscaling factor $N = 4$) except for ^{196}Po, where the beam intensity was significantly lower (see Table 4.1). However, during the 2012 experimental campaign the p-γ coincidence gate was not set correctly for two of the four quadrants of the DSSSD. This gave rise to downscaling of the p-γ coincidences instead of the particles without coincident γ rays for half of the data. The consequences of this uncorrect downscaling procedure are discussed in more detail in section III A 2.

III. OFFLINE DATA ANALYSIS

A. Selection of events

1. Selection based on kinematic properties

The Miniball detection setup registers a large amount of data on scattered particles and decay radiation. As the Coulomb-excitation events are hidden in this background, identifying these events of interest is a crucial step in the data analysis. The detected particle energy in the DSSSD as a function of the scattering angle in the laboratory frame of reference θ for ^{200}Po on ^{104}Pd is shown in Figure 4.2. It shows a typical inverse kinematics scattering pattern. The recoiling target atoms (further called "recoils") are scattered throughout the whole detection range of the DSSSD while the heavier beam particles are detected only at smaller scattering angles in the laboratory frame of reference.

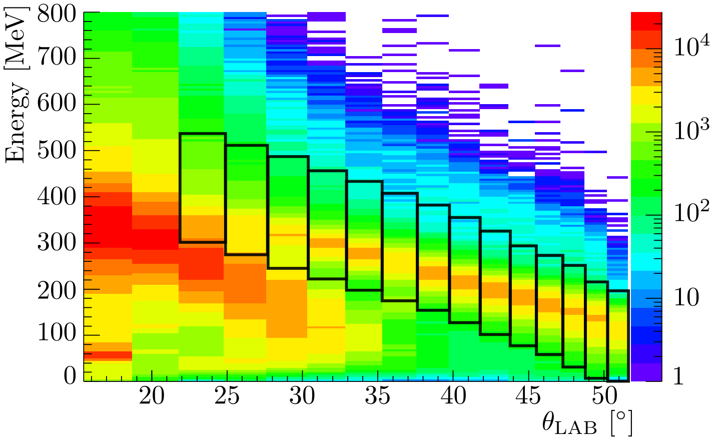

Figure 4.2: (Color online) Particle energy versus scattering angle in the laboratory frame of reference θ_{LAB} for ^{200}Po on ^{104}Pd. The color scale on the vertical axis represents the intensity in each bin. Only particles that are coincident with at least one γ ray are shown. The gates chosen to select the ^{104}Pd recoil are shown in black. The two innermost strips are not taken into account as it is not possible to distinguish between the beam and the recoil particles in this angular range.

It is thus possible to make a distinction between a beam particle and a recoil, based on the energy-versus-angle kinematics. Detected particles in the DSSSD related to the scattering of beam on target are selected by “following” the recoils through the range of the DSSSD. For each case, specific E-versus-θ gates were adopted to select the recoils scattered in the particle detector and to avoid including noise into the analysis. As an example, the gates that were used for ^{200}Po on ^{104}Pd can be seen in Figure 4.2. The two innermost strips of the particle detector were excluded from the analysis because in this region of the detector the beam and recoil particles are not separable. The range of centre-of-mass scattering angles that was covered by applying this method is shown for each reaction in Table 4.1.

2. Selection based on timing properties

Figure 4.3 shows the time difference between a particle and a γ ray that were detected during the Coulomb-excitation experiments of ^{200}Po on ^{104}Pd in panel A and ^{198}Po on ^{94}Mo in panel B. The different structure of the data on ^{198}Po

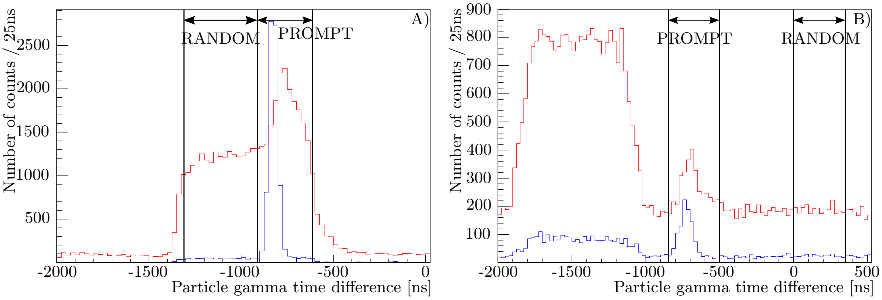

Figure 4.3: (Color online) Time difference between particle and γ ray, gated on the $2_1^+ \rightarrow 0_1^+$ γ-ray transitions in blue and gated on polonium X rays in red. The prompt and random coincidence windows that were used are shown in black. A) Sum of p-γ timing information of all quadrants (2009 data of ^{200}Po on ^{104}Pd). B) p-γ timing information for quadrants 1 and 2 where the downscaling was not properly set (2012 data of ^{198}Po on ^{94}Mo).

can be explained by a problem with the downscaling in 2012. A difference in time behavior is observed between the γ rays following Coulomb excitation (de-exciting the 2_1^+ state in the polonium isotope) and the low-energy polonium X rays and is due to the energy dependence of the time response of the Ge detectors. The prompt p-γ coincidence window is defined broad enough to include the low-energy X rays. Random p-γ coincidences are selected with a second time window. In the normal case of the 2009 data on ^{200}Po, the random window is chosen within the region where the events are not downscaled. This allows to scale the prompt and random events using the difference in length of the two respective windows. The data with the wrongly downscaled events were treated in a slightly different way. As the prompt p-γ events fall inside the downscaled region in this case, the random window is also selected among the downscaled events.

The purification power of the event selection based on kinematics and timing is highlighted in Figure 4.4, where all detected γ rays in the ^{200}Po experiment are shown in the top panel. The γ rays following Coulomb excitation are not visible yet in this γ-ray energy spectrum. By selecting the prompt p-γ coincidences that satisfy the kinematic gates and subsequently subtracting the random coincidences from it, a clean γ-ray energy spectrum, associated with events following Coulomb excitation, is obtained (lower panel in Figure 4.4). As the γ rays of interest are emitted in flight, the angular information of the detected particle and γ ray can be used to perform a Doppler correction of the detected γ-ray energy. Finally a $\gamma\gamma$-coincidence window of 350 ns is defined to check for

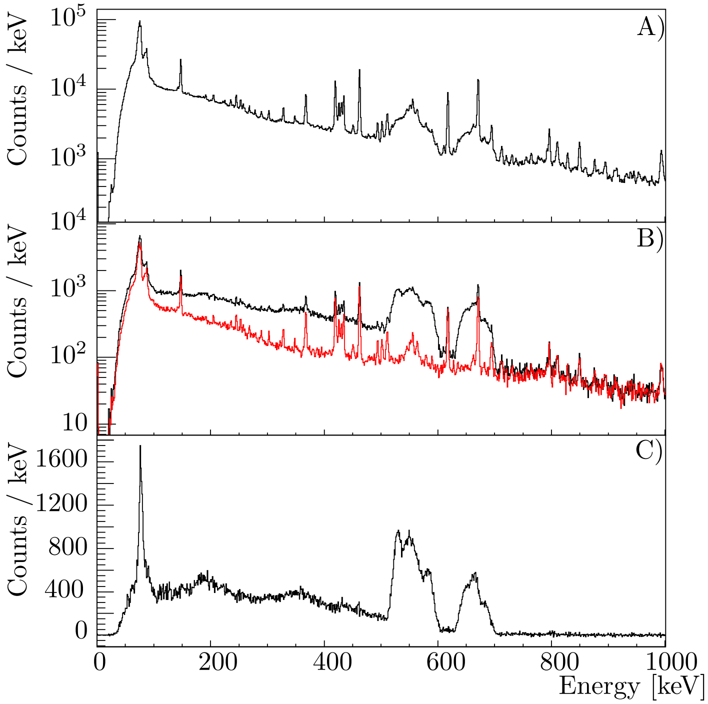

Figure 4.4: (Color online) The γ-ray energy spectra shown here display the 2009 data of ^{200}Po on the ^{104}Pd target. A) All γ rays that were detected. B) Prompt γ rays (black) and random γ rays (red) that fulfill the kinematic conditions. C) Subtracted prompt-minus-random γ spectrum.

coincidences between the emitted γ rays.

B. Polonium X rays

In addition to the γ rays following the Coulomb excitation of target and projectile, the background-subtracted γ-ray energy spectra show, for all isotopes that were studied, two peaks around 78 keV and 90 keV. These energies correspond to the polonium K_α and K_β X rays, respectively. Origins of these polonium X rays include internal conversion of observed γ rays and $E0$ transitions. An additional source of X rays that should be taken into account is the heavy-ion induced K-vacancy creation process due to atomic processes in the secondary Coulomb-excitation target [3, 36]. Theoretical

Table 4.2: The scaling factor to match the predicted and observed amount of atomically produced X rays in ^{202,206}Po. σ_{exp} is the experimentally detected K_α X-ray cross section related to the atomic effect (corrected for the X rays attributed to internal conversion), σ_{theo} is the integrated K_α X-ray cross section predicted by theory and R is the ratio of the observed versus predicted cross section. Conversion coefficients $\alpha_{2_1^+\rightarrow 0_1^+}$ are taken from [38].

Isotope	Target	$\alpha_{2_1^+\rightarrow 0_1^+}$	σ_{exp} [b]	σ_{theo} [b]	R
^{202}Po	^{104}Pd	0.01210(17)	0.16(5)	0.743(11)	0.22(6)
^{202}Po	^{94}Mo	0.01210(17)	0.13(4)	0.616(9)	0.21(7)
^{206}Po	^{104}Pd	0.01132(16)	0.15(3)	0.747(11)	0.20(4)

formulas describing the cross section for this process as a function of beam energy, target mass and ionization potential have to be scaled to match the experimentally observed cross sections. Reference [36] summarizes data on the observation of X rays in Coulomb-excitation experiments on isotopes in the light-lead region at ISOLDE. The cross section for the K-vacancy creation process is observed to be significantly higher in the polonium isotopes than in the neighboring isotopes that were studied (mercury, lead and radon). In this case, data on the Coulomb excitation of ^{202}Po and ^{206}Po (the latter being part of a different experimental campaign at ISOLDE [37]) were used to scale the theoretical predictions. As no low-lying excited 0^+ states are observed in these isotopes, the only nuclear effect giving rise to polonium X rays, is internal conversion of observed γ rays of which the cross section can be calculated using the known conversion coefficients [38]. A weighted average scaling factor of 0.20(3) results from a comparison of the number of observed and expected X rays (details in Table 4.2).

The scaling factor that is determined with the data on ^{202,206}Po is then used to rescale the predicted amount of X rays originating from the heavy-ion induced K-vacancy creation effect for all isotopes. The total number of X rays is determined using the K_α intensity, $\mathrm{K}_\alpha/\mathrm{K}_\beta$ branching ratio and the polonium fluorescence yield $\omega_{\mathrm{K}} = 0.965$ [39]. A comparison of the number of observed K_α X rays to the number of (rescaled) expected K_α X rays is shown for all studied isotopes in Figure 4.5. In the later Coulomb-excitation analysis of the ^{200}Po data the assumption is made that all the observed X rays are related to the atomic effect and the internal conversion of the $2_1^+ \rightarrow 0_1^+$ transition. The limits that can be extracted from the comparison between the number of observed and expected X rays are taken into account into the further analysis for ^{196,198}Po. Sections III D 1 and III D 2 describe how $\gamma\gamma$ coincidences are

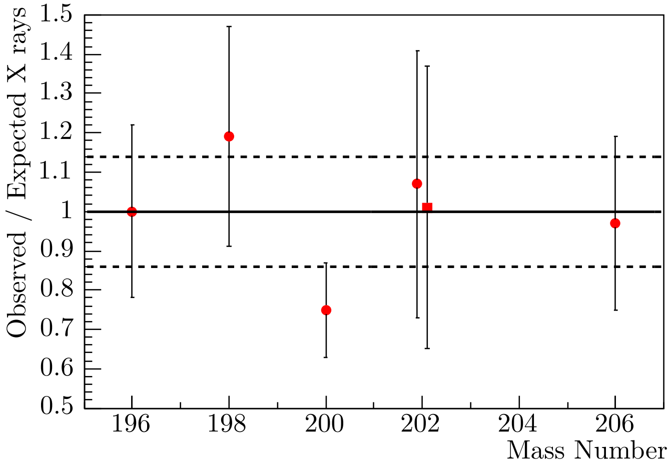

Figure 4.5: The ratio of the number of observed X rays to the number of (rescaled) expected X rays is plotted for all studied polonium isotopes. For ^{202}Po two points are drawn: the circle represents the data on ^{104}Pd, the square represents the ^{94}Mo data. The solid black line represents the scaling factor with the associated uncertainty (in dashed lines) deduced from the ^{202,206}Po data.

used to distinguish between possible E0 transitions depopulating the 0_2^+ state and the 2_2^+ state.

C. ^{94}Mo Target impurity

The Coulomb excitation of ^{198}Po and ^{202}Po was studied using a ^{94}Mo target. Based on the energies and transition probabilities of the low-lying excited states in ^{94}Mo (Figure 4.6) one γ-ray transition related to target excitation at 871 keV is expected. However, the background-subtracted γ-ray energy spectrum for ^{198}Po on ^{94}Mo in Figure 4.7 shows a second transition around 200 keV. This γ ray can be associated with Coulomb excitation of the $3/2^+$ state at 204 keV in the ^{95}Mo impurity in the target as the FWHM of the peak decreases when a Doppler correction for the target recoil trajectory is applied to the γ-ray energies. The isotopic impurity of the target was independently observed in the analysis of other Coulomb-excitation experiments that used the same target [40, 41].

Using the efficiency-corrected intensity balance between the 871 keV and 204 keV γ rays and the Coulomb-excitation cross section for ^{94}Mo and ^{95}Mo by a

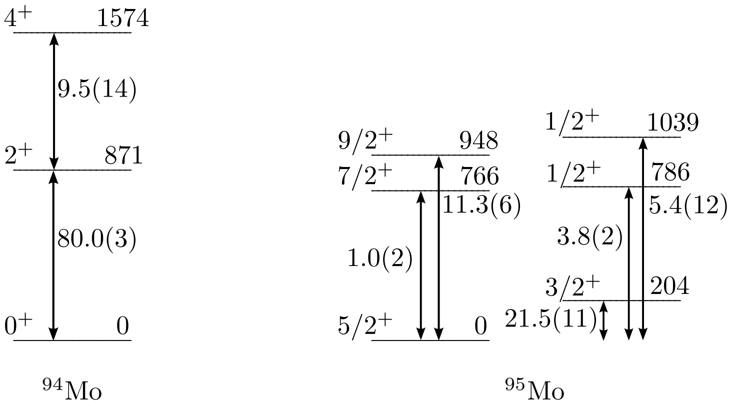

Figure 4.6: Level energies (in keV) and reduced transition probabilities $B(E2)\uparrow$ (in W.u.) of low-lying excited states in ^{94,95}Mo. Data is taken from Nuclear Data Sheets and [42, 43].

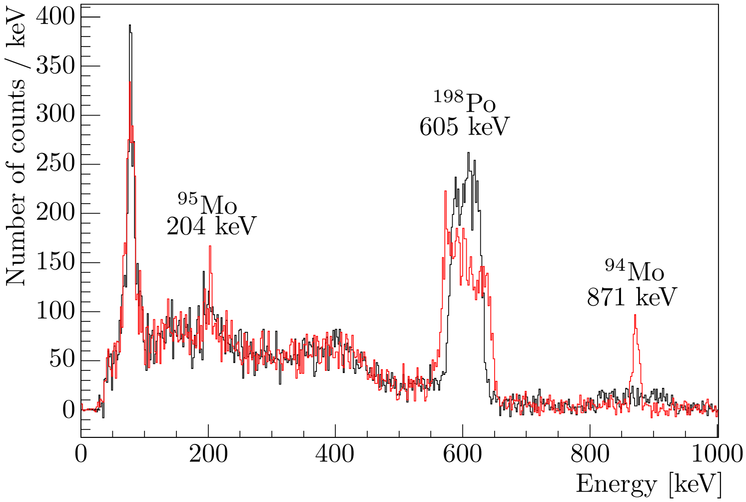

Figure 4.7: (Color online) Background-subtracted γ-ray energy spectrum for ^{198}Po on ^{94}Mo in black, Doppler corrected for the target in red.

^{198}Po projectile, the ^{94}Mo component in the target was determined to be $F_{^{94}\text{Mo}} = 95(2)\,\%$. As the absolute Coulomb-excitation cross sections in the polonium isotopes are determined by normalizing to the known Coulomb-excitation cross section for the given target nucleus (as described in section IV), the target impurity needs to be taken into account. This is done in an indirect way by correcting the number of target excitation counts:

$$N_{\gamma,^{94}\text{Mo,total}} = N_{\gamma,^{94}\text{Mo}} \left(1 + \frac{F_{^{95}\text{Mo}}}{F_{^{94}\text{Mo}}} \frac{\sigma_p\left(Z, A'\right)}{\sigma_p\left(Z, A\right)}\right) \tag{4.1}$$

where $F_{^{94(95)}\text{Mo}}$ is the fraction of $^{94(95)}$Mo in the target, $N_{\gamma,^{94}\text{Mo}}$ is the number of counts in the 871 keV peak and $N_{\gamma,^{94}\text{Mo,total}}$ is the corrected number of ^{94}Mo de-excitations. $\frac{\sigma_p\left(Z,A'\right)}{\sigma_p(Z,A)}$ is the ratio of the cross section for Coulomb excitation of the state of interest in the polonium projectile, incident on a target with mass $A' = 95$ to the Coulomb-excitation cross section of the state of interest in the polonium projectile, incident on a target with mass $A = 94$. This ratio contains the difference in Rutherford cross section and the different centre-of-mass energy at different target mass. In the case of ^{202}Po, this ratio of cross sections was determined using the projectile matrix elements that were determined with the ^{104}Pd target. In ^{198}Po however, this procedure was not possible as all the data was taken with the ^{94}Mo target. Therefore, the known ratio of Coulomb-excitation cross sections of the target (calculated with mass 94 and mass 95) was used as a first-order estimate [44].

D. Experimental data analysis

This section describes the data analysis for the four isotopes that were studied in this work. For each isotope, the background-subtracted and Doppler-corrected γ-ray energy spectrum, following the Coulomb excitation of the polonium isotope, is shown. In order to be sensitive to the second-order effect of the diagonal matrix element of the 2_1^+ state, the data is divided into a number of angular ranges. The adopted number of subdivisions per isotope depends on the statistics that were obtained in both the projectile and target yields. The total statistics that were acquired, together with the deduced Coulomb-excitation cross section σ_{CE}, are shown in Table 4.3 for all isotopes. The cross section was calculated using the integrated beam current, which was determined using the known cross section for Coulomb excitation of the target nucleus, taking into account the beam purity (see Table 4.1), the target purity and the Miniball detection efficiencies at the respective transition energies [33].

In the two heaviest isotopes that were studied, only the 2_1^+ state was populated. The γ-ray energy spectra are shown in Figure 4.8 and 4.9 for ^{202}Po and ^{200}Po

Table 4.3: Statistics obtained in the Coulomb-excitation experiments of $^{196-202}$Po on the ^{104}Pd and ^{94}Mo targets. N_γ represents the number of detected γ rays at the Miniball setup, σ_{CE} is the deduced cross section for Coulomb excitation in barn.

^{202}Po on ^{104}Pd			
Nucleus	Transition	N_γ	σ_{CE} [b]
^{202}Po	$2_1^+ \to 0_1^+$	$3.8(3) \times 10^2$	0.45(6)
^{104}Pd	$2_1^+ \to 0_1^+$	$1.04(4) \times 10^3$	
^{202}Po on ^{94}Mo			
Nucleus	Transition	N_γ	σ_{CE} [b]
^{202}Po	$2_1^+ \to 0_1^+$	$2.2(2) \times 10^2$	0.39(8)
^{94}Mo	$2_1^+ \to 0_1^+$	75(13)	
^{200}Po on ^{104}Pd			
Nucleus	Transition	N_γ	σ_{CE} [b]
^{200}Po	$2_1^+ \to 0_1^+$	$1.930(18) \times 10^4$	0.48(3)
^{104}Pd	$2_1^+ \to 0_1^+$	$4.37(3) \times 10^4$	
^{198}Po on ^{94}Mo			
Nucleus	Transition	N_γ	σ_{CE} [b]
^{198}Po	$2_1^+ \to 0_1^+$	$4.60(8) \times 10^3$	1.00(16)
	$4_1^+ \to 2_1^+$	171(39)	0.038(11)
	$0_2^+ \to 2_1^+$	78(58)	0.03(4)
	$2_2^+ \to 2_1^+$	34(40)	0.010(12)
^{94}Mo	$2_1^+ \to 0_1^+$	$5.3(3) \times 10^2$	
^{196}Po on ^{104}Pd			
Nucleus	Transition	N_γ	σ_{CE} [b]
^{196}Po	$2_1^+ \to 0_1^+$	$6.05(9) \times 10^3$	1.67(19)
	$4_1^+ \to 2_1^+$	373(41)	0.108(17)
	$2_2^+ \to 0_1^+$	79(12)	0.052(14)
	$2_2^+ \to 2_1^+$	85(35)	0.06(3)
^{104}Pd	$2_1^+ \to 0_1^+$	$5.17(8) \times 10^3$	

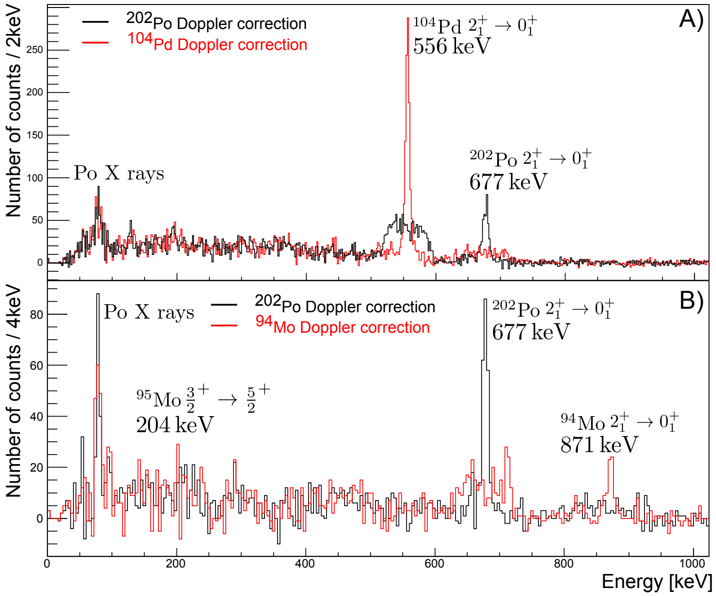

Figure 4.8: (Color online) Background-subtracted and Doppler corrected γ-ray energy spectrum following the Coulomb excitation of ^{202}Po, induced by the ^{202}Po beam impinging on the A) ^{104}Pd and on B) ^{94}Mo target. The red spectrum is Doppler corrected for the target, the black spectrum is Doppler corrected for the projectile. The observed transitions are highlighted.

respectively. As in ^{196,198}Po, multi-step Coulomb excitation was observed, additional details related to the data analysis of these two isotopes are provided below.

1. Data obtained for ^{198}Po

The background-subtracted γ-ray spectrum of ^{198}Po on ^{94}Mo is shown in panel A of Figure 4.10. While in the ^{94}Mo target only the 2_1^+ state was populated, multiple-step Coulomb excitation was observed in ^{198}Po to the 4_1^+, 0_2^+ and 2_2^+ states (see level scheme in Figure 4.15). A clearer view on the $4_1^+ \rightarrow 2_1^+$ transition results by gating on the $2_1^+ \rightarrow 0_1^+$ γ ray at 605 keV (panel B of Figure 4.10). There is only a weak indication of the transitions depopulating the 0_2^+ and 2_2^+ states, which is reflected in the size and relative error of the extracted intensities. The resulting intensities for all the observed transitions, together

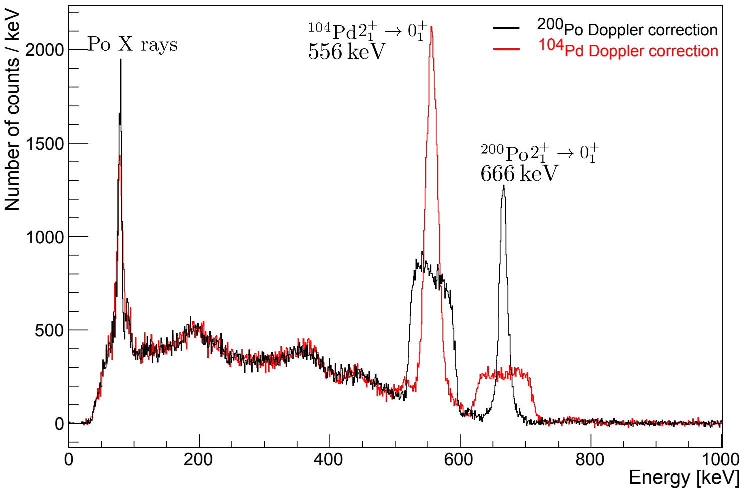

Figure 4.9: (Color online) Background-subtracted and Doppler corrected γ-ray energy spectrum following the Coulomb excitation of ^{200}Po, induced by the ^{200}Po beam impinging on the ^{104}Pd target. The red spectrum is Doppler corrected for the target, the black spectrum is Doppler corrected for the projectile. The observed transitions are highlighted.

with the statistics in the $2_1^+ \rightarrow 0_1^+$ transitions in projectile and target are shown in Table 4.3. The statistics in the $2_1^+ \rightarrow 0_1^+$ transitions in the projectile and target nuclei allowed to divide the data in five different angular ranges.

The particle-gated $\gamma\gamma$-energy spectrum also contains polonium X rays, which can be attributed to the conversion of observed coincident γ rays and to the $E0$ component of the $2_2^+ \rightarrow 2_1^+$ transition. The $4_1^+ \rightarrow 2_1^+$ transition, which is observed in both the “singles” particle-gated γ-ray energy spectrum as in the particle-gated $\gamma\gamma$ spectrum, is used to link the intensity in the $\gamma\gamma$ spectrum to the “singles” intensity. A scaling factor S is defined as

$$S = \frac{I_{4_1^+ \rightarrow 2_1^+,\text{singles}}}{I_{4_1^+ \rightarrow 2_1^+,\text{coincidences}}}, \tag{4.2}$$

which is equal to 10(4) in this case and includes the γ-ray detection efficiency of the $2_1^+ \rightarrow 0_1^+$ transition and accounts for the different coincidence conditions that were applied in the construction of the singles γ-ray energy spectrum and the $\gamma\gamma$ spectrum. The intensity of the polonium X rays in the $\gamma\gamma$ spectrum

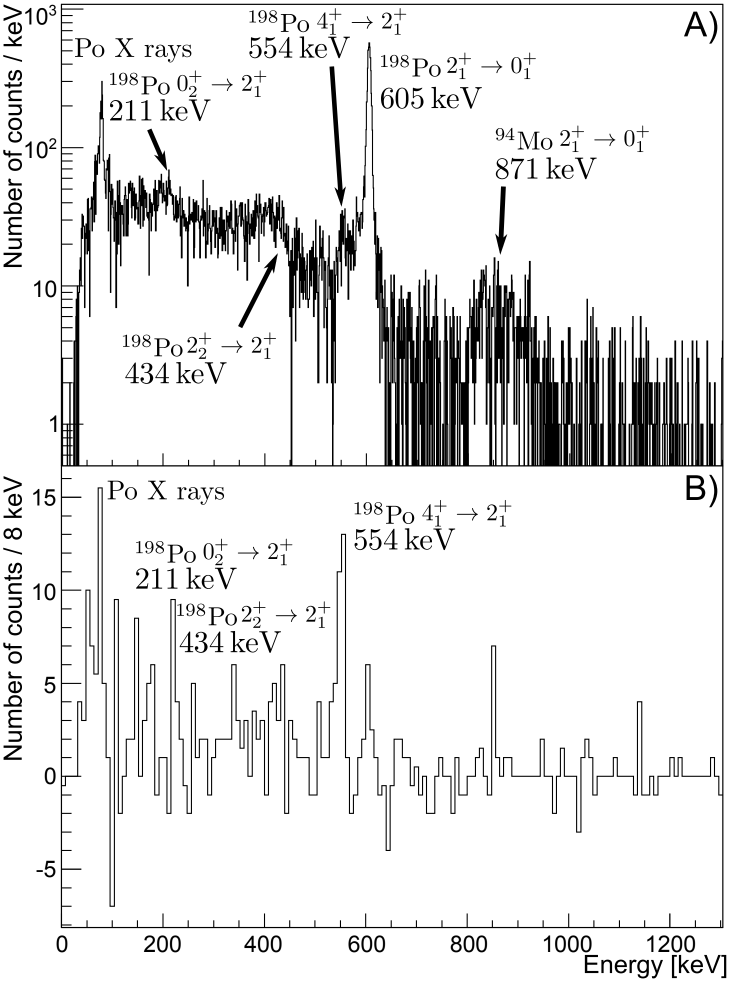

Figure 4.10: A) Background-subtracted and Doppler-corrected γ-ray energy spectrum following the Coulomb excitation of ^{198}Po, induced by the ^{198}Po beam on the ^{94}Mo target. The γ-ray energies were Doppler corrected for ^{198}Po, the target Doppler correction is shown in Figure 4.7. The observed transitions are highlighted. B) Energy of γ rays that are coincident with the $2_1^+ \to 0_1^+$ γ ray at 605 keV in ^{198}Po. The gated spectrum is background subtracted and Doppler corrected for ^{198}Po. The observed transitions in ^{198}Po are highlighted.

Table 4.4: 1σ upper limits for unobserved transitions in the Coulomb excitation of ^{198}Po on ^{94}Mo. The values for the 1σ upper limits (UPL) are determined using the method described in [46] and are not efficiency corrected. The uncertainty that is mentioned on the upper limit, represents the 1σ uncertainty on the value. F is the efficiency-corrected ratio of the 1σ upper limit to the intensity of the $2_1^+ \to 0_1^+$ transition.

Transition	Energy [keV]	UPL	F
$6_1^+ \to 4_1^+$	559	44(30)	0.92%
$2_2^+ \to 0_2^+$	223	31(50)	0.40%
$2_2^+ \to 0_1^+$	1039	17(15)	0.48%

is then corrected for conversion of other γ-ray transitions in the $\gamma\gamma$ spectrum (assuming $\delta = 1.8(5)$ [45]) and for the (small) amount of “atomic” X rays present in the $\gamma\gamma$ spectrum. From this, a total of 80(130) X rays is associated with the $E0$ component of the $2_2^+ \to 2_1^+$ transition and 150(310) X rays are attributed to the $E0$ transition between the excited 0^+ state and the ground state. Details of this calculation can be found in [33]. The large uncertainties on these numbers are due to the indirect method of determining these intensities.

Finally, following the method described in [46] 1σ upper limits were determined for the unobserved transitions. The upper limits, shown in Table 4.4, are taken into account in the Coulomb-excitation analysis that is described in section IV B 1.

2. Data obtained for ^{196}Po

The Coulomb excitation of ^{196}Po was studied on a ^{104}Pd target. The background-subtracted γ-ray energy spectrum in panel A of Figure 4.11 shows that multi-step Coulomb excitation was observed. The γ rays de-exciting the 4_1^+ and 2_2^+ states are clearly visible next to some lines that cannot be placed in the level scheme of ^{196}Po (Figure 4.15). The comparison of the Coulomb-excitation spectra, that were acquired during the laser ON and laser OFF periods of the laser ON/OFF data in panel A of Figure 4.11, shows that the unknown transitions originate from de-excitation of populated levels in the isobaric contaminant ^{196}Tl.

The beam purity, time-integrated over all the laser ON/OFF runs, was determined to be 59.51(7) %. The same method as in [32] was applied to extract the beam purity during the runs where the lasers were on continuously. In this approach, the intensity of the γ rays associated with Coulomb excitation of polonium ($2_1^+ \rightarrow 0_1^+$ at 463 keV) and thallium ($1^- \rightarrow 2^-$ at 253 keV) were taken into account, together with an extrapolation factor from the laser ON/OFF runs, yielding a total purity of 46 $\binom{6}{4}$ %. The larger relative error bar is due to the smaller statistics in the Coulomb-excitation transitions compared to the scattered particles on the DSSSD. The target de-excitation γ-ray yields were extracted in a separate analysis for the ON/OFF runs and the ON runs, employing the respective correction factors for the beam purity.

The projection of the $\gamma\gamma$-energy matrix with a gate on the 463 keV $2_1^+ \rightarrow 0_1^+$ transition is shown in panel B of Figure 4.11. From the 15(9) detected coincident K$_\alpha$ X rays, 4(2) are associated with $E2/M1$ conversion. The unknown $E2/M1$ mixing ratio of the $2_2^+ \rightarrow 2_1^+$ transition was taken into account by applying the same method as in the case of ^{198}Po. The remaining 11(9) K$_\alpha$ X rays translate, using equation 4.10 to get to a scaling factor of $S = 5.3(9)$, into 76(66) X rays that can be related to the $E0$ component of the $2_2^+ \rightarrow 2_1^+$ transition. The number of X rays originating from the $0_2^+ \rightarrow 0_1^+$ $E0$ transition, is then finally determined by subtracting the K$_\alpha$ X rays related to internal conversion (370(70)) and the estimate for the K$_\alpha$ X rays originating from the K-vacancy creation effect (700(130)) from the total number of detected K$_\alpha$ X rays (990(80)). The calculated $E0$ $0_2^+ \rightarrow 0_1^+$ intensity is compatible with 0 and gives an upper limit of 140 counts. The detection of $E0$ $0_2^+ \rightarrow 0_1^+$ transitions can thus not be excluded.

Table 4.3 summarizes the intensities of the observed transitions in the Coulomb excitation of ^{196}Po on ^{104}Pd. Seven different angular ranges were defined for the $2_1^+ \rightarrow 0_1^+$ transitions in target and projectile and for the $4_1^+ \rightarrow 2_1^+$ transition in ^{196}Po to gain sensitivity on second-order effects. The deduced cross section for Coulomb excitation, σ_{CE}, is extracted based on the known cross section for Coulomb excitation for the target and taking into account the beam purity and the Miniball detection efficiencies at the respective transition energies. Finally, following the same method as in ^{198}Po, 1σ upper limits were determined for the unobserved transitions (see Table 4.5).

IV. GOSIA ANALYSIS

The unknown matrix elements coupling the low-lying states in the polonium isotopes are extracted using the coupled-channels Coulomb-excitation analysis code GOSIA [47, 48]. Two different approaches are used, depending on the number of states that are populated in the experiment. In the case where only the 2_1^+ state is populated, GOSIA2 is used (see section IV A). When multi-step Coulomb excitation is observed, a combined approach using GOSIA and GOSIA2 is employed, as explained in section IV B.

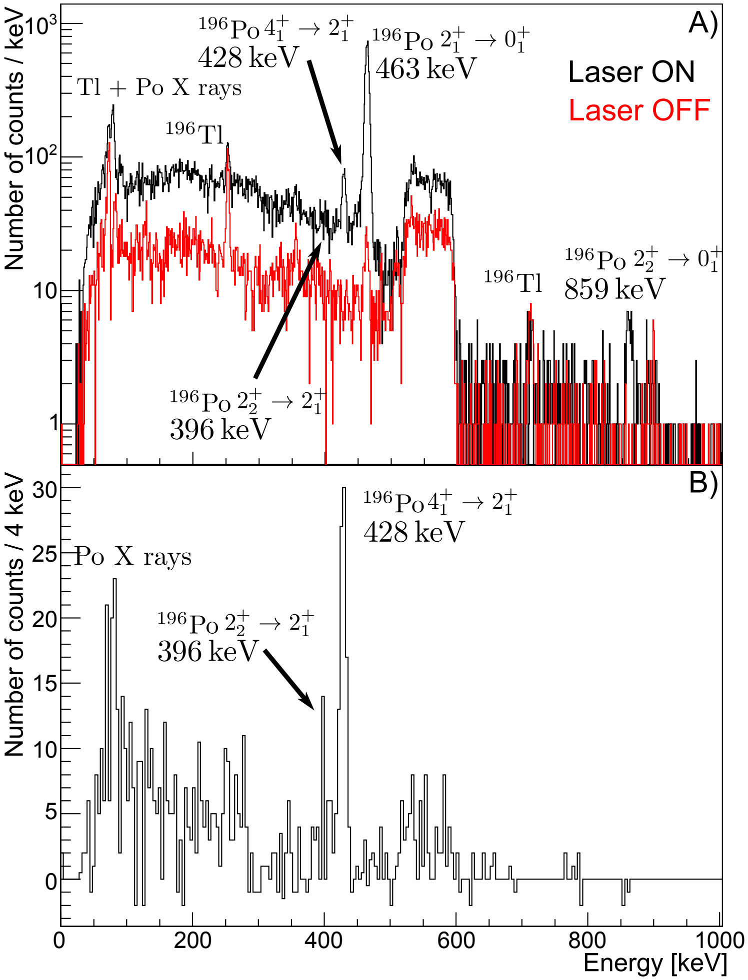

Figure 4.11: (Color online) A) Background-subtracted and Doppler-corrected γ-ray energy spectrum following the Coulomb excitation of ^{196}Po, induced by the ^{196}Po beam on the ^{104}Pd target during equally long laser ON (in black) and laser OFF (in red) windows. The γ energies are Doppler corrected for mass 196 and the observed transitions are highlighted. The broad structure around 550 keV is due to the ^{104}Pd target excitation at 556 keV. B) Energy of γ rays that are coincident with the $2_1^+ \to 0_1^+$ γ ray at 463 keV in ^{196}Po. The gated spectrum is background subtracted and Doppler corrected for ^{196}Po. The observed transitions in ^{196}Po are highlighted.

Table 4.5: 1σ upper limits for unobserved transitions in the Coulomb excitation of ^{196}Po on ^{104}Pd. The values for the 1σ upper limits (UPL) are determined using the method described in [46] and are not efficiency corrected. The uncertainty that is mentioned on the upper limit, represents the 1σ uncertainty on the value. F is the efficiency-corrected ratio of the 1σ upper limit to the intensity of the $2^+_1 \rightarrow 0^+_1$ transition.

Transition	Energy [keV]	UPL	F
$6^+_1 \rightarrow 4^+_1$	499	9(20)	0.2%
$0^+_2 \rightarrow 2^+_1$	95	61(70)	0.6%
$2^+_2 \rightarrow 0^+_2$	301	48(60)	0.6%
$4^+_2 \rightarrow 4^+_1$	497	21(20)	0.4%
$4^+_2 \rightarrow 2^+_2$	529	528(50)	9.5%
$4^+_2 \rightarrow 2^+_1$	925	8(2)	0.2%

A. Exclusive population of 2^+_1 state

This section deals with the cases of ^{200,202}Po in which only the 2^+_1 state is populated. The Coulomb-excitation cross section is affected by the matrix element coupling the ground state to the populated 2^+_1 state $\langle 0^+_1||E2||2^+_1\rangle$ and, to second order, by the diagonal matrix element of the 2^+_1 state $\langle 2^+_1||E2||2^+_1\rangle$. The sensitivity to the second-order effect is determined by the obtained statistics, i.e. the number of subdivisions that was adopted.

Measuring the intensity of the incoming beam is difficult in a radioactive ion-beam experiment with low beam energy as the intensity is very low and can fluctuate. The beam can be contaminated as well. Another normalization method is thus needed. The Coulomb-excitation cross section of the projectile is normalized to the target-excitation cross section, which is calculated using the known matrix elements of the target. Table 4.6 lists the matrix elements coupling the relevant states in the ^{104}Pd and ^{94}Mo targets that were used.

GOSIA2 is a special version of the GOSIA code that simultaneously minimizes the χ^2 function for the projectile and target, thus resulting in a set of normalization constants and projectile matrix elements that best reproduce the experimental γ-ray yields. A drawback of the current version of GOSIA2 is that a proper correlated-error determination is not implemented. As only two parameters are determined, the correlated uncertainties are extracted by constructing a two-dimensional χ^2 surface and projecting the 1σ contour of the total χ^2 surface

Table 4.6: Matrix elements coupling the relevant states in ^{104}Pd and ^{94}Mo. These matrix elements were used to determine the cross section for Coulomb excitation of the target.

Isotope	Matrix element	Value [eb]	Reference
^{104}Pd	$\langle 0_1^+ \| E2 \| 2_1^+ \rangle$	0.73(2)	[49]
	$\langle 0_1^+ \| E2 \| 2_2^+ \rangle$	0.134(7)	[50]
	$\langle 2_1^+ \| E2 \| 2_1^+ \rangle$	-0.61(15)	[51]
	$\langle 2_1^+ \| E2 \| 4_1^+ \rangle$	1.16(3)	[50]
	$\langle 2_1^+ \| E2 \| 0_2^+ \rangle$	0.20(1)	[50]
	$\langle 2_1^+ \| E2 \| 2_2^+ \rangle$	0.57(3)	[50]
^{94}Mo	$\langle 0_1^+ \| E2 \| 2_1^+ \rangle$	0.451(4)	[52]
	$\langle 2_1^+ \| E2 \| 2_1^+ \rangle$	0.17(11)	[53]
	$\langle 2_1^+ \| E2 \| 4_1^+ \rangle$	0.78(6)	[54]

on the respective axis [44]. In this case the 1σ contour is defined as the points for which $\chi^2_{min} \leq \chi^2 \leq \chi^2_{min} + 1$.

1. ^{202}Po

Coulomb excitation of ^{202}Po was studied using two different targets, ^{94}Mo and ^{104}Pd. Most of the statistics, especially on target excitation, was collected on the ^{104}Pd target. The $4_1^+ \rightarrow 2_1^+$ transition in ^{202}Po was not observed above the level of 13 % (5 %) relative to the ^{202}Po $2_1^+ \rightarrow 0_1^+$ γ ray in the ^{104}Pd (^{94}Mo) experiment. The higher upper limit for the ^{104}Pd target is due to the overlap of the $4_1^+ \rightarrow 2_1^+$ γ-ray energy with the target de-excitation transition energy. In both cases the assumption is made that only the 2_1^+ state is populated. Figure 4.12 shows the total χ^2 surface that was constructed in which χ^2 is defined as:

$$\chi^2 = \chi^2_{\mathrm{Total},^{94}\mathrm{Mo}} + \chi^2_{\mathrm{Total},^{104}\mathrm{Pd}}, \tag{4.3}$$

where

$$\chi^2_{\mathrm{Total}} = \mathrm{N_P^{data}}\chi^2_{\mathrm{P,GOSIA}} + \mathrm{N_T^{data}}\chi^2_{\mathrm{T,GOSIA}}. \tag{4.4}$$

Here, $\mathrm{N_P^{data}}$ is the number of data points for the projectile (3(2) for the experiment on ^{104}Pd(^{94}Mo)) and $\mathrm{N_T^{data}}$ represents the number of data points for the target (5(4) for ^{104}Pd(^{94}Mo)). The number of data points for the target include the known matrix elements that were provided to GOSIA (with their error bars). $\chi^2_{\mathrm{P,GOSIA}}$ and $\chi^2_{\mathrm{T,GOSIA}}$ are the reduced χ^2 values that are given as output by the GOSIA code.

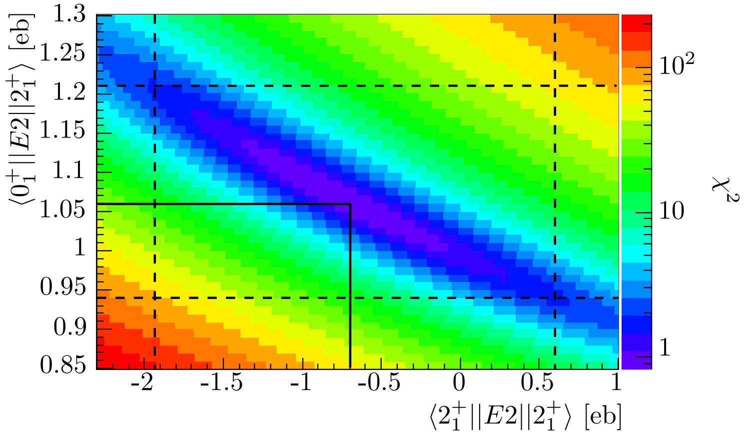

Figure 4.12: (Color online) χ^2 surface of the transitional and diagonal matrix element of the 2_1^+ state in ^{202}Po. The χ^2 is the sum of the χ^2 resulting from the experiment on ^{104}Pd and the χ^2 extracted from the ^{94}Mo experiment. Projection of the 1σ contour (dotted lines) gives the correlated uncertainties on the two parameters that are extracted.

The correlated uncertainties of the transitional and diagonal matrix element can be deduced from the 1σ contour as shown in Figure 4.12. The resulting matrix elements with their corresponding error bars are given in Table 4.7. The value for the transitional matrix element, assuming that $\langle 2_1^+||E2||2_1^+\rangle = 0\,\text{eb}$, i.e. with no influence of second-order effects, is also given. The error bar that is extracted in this way represents the quality of the data in a simplified way and reflects the statistical error of the measured (projectile and target) γ-ray yields, the uncertainty on the γ-ray detection efficiency, on the beam and target purity and the error bar on the matrix elements of the target.

2. ^{200}Po

Coulomb excitation of ^{200}Po was studied only with the ^{104}Pd target. The $4_1^+ \rightarrow 2_1^+$ and $0_2^+ \rightarrow 2_1^+$ γ rays were not observed above the level of 0.9 % and 0.7 % relative to the ^{200}Po $2_1^+ \rightarrow 0_1^+$ γ ray, respectively, so an exclusive population of the 2_1^+ state was assumed. Figure 4.13 shows the total χ^2 surface that was constructed applying the χ^2 definition given in equation 4.4 with $\mathrm{N_P^{data}} = 14$ and $\mathrm{N_T^{data}} = 16$. Significantly higher sensitivity to the second-order effect of the diagonal matrix element results from the large statistics that were

Table 4.7: Final results for the matrix elements extracted in ^{200,202}Po in this work, using the GOSIA2 code. Two values of the transitional matrix element $\langle 0_1^+||E2||2_1^+\rangle$ are listed: the first results from the full χ^2 surface analysis, the second value $\langle 0_1^+||E2||2_1^+\rangle$(Q=0) is the value that results from projecting the surface at $\langle 2_1^+||E2||2_1^+\rangle = 0\,$eb. The transition energies $E_\gamma(2_1^+ \rightarrow 0_1^+)$ and their uncertainties are taken from literature.

Isotope	$E_\gamma(2_1^+ \rightarrow 0_1^+)$ [keV]	$\langle 0_1^+\|\|E2\|\|2_1^+\rangle$ [eb]	$\langle 2_1^+\|\|E2\|\|2_1^+\rangle$ [eb]	χ^2_{min}	$\langle 0_1^+\|\|E2\|\|2_1^+\rangle$(Q=0) [eb]
^{202}Po	677.2(2)	$1.06(^{15}_{13})$	$-0.7(^{13}_{12})$	0.8	0.99(4)
^{200}Po	665.9(1)	1.03(3)	0.1(2)	7.9	1.040(8)

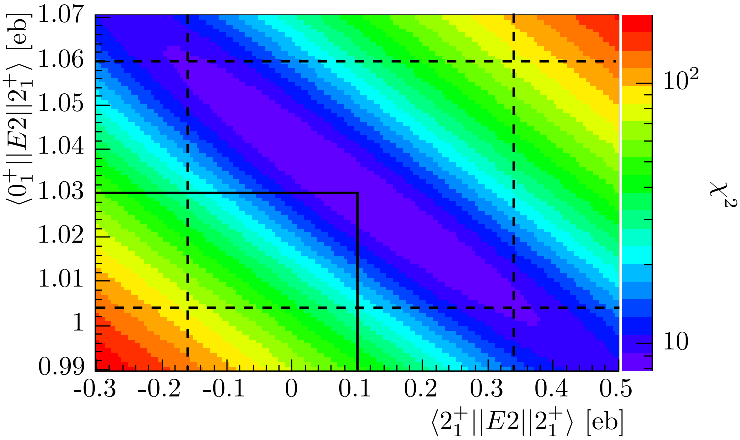

Figure 4.13: (Color online) Large scale χ^2 surface of the transitional and diagonal matrix element of the 2_1^+ state in ^{200}Po. Projection of the 1σ contour gives the correlated uncertainties on the two parameters that are extracted.

acquired, which allowed to divide the data into 14 angular ranges. The resulting matrix elements with their corresponding error bars are given in Table 4.7. An independent χ^2-surface analysis, with 6 angular ranges instead of 14, yielded consistent results with a slightly larger error bar for the $\langle 2_1^+||E2||2_1^+\rangle$ diagonal matrix element. Also a value for the transitional matrix element, under the assumption that $\langle 2_1^+||E2||2_1^+\rangle = 0\,$eb, i.e. with no influence of second-order effects, is given.

B. Population of several low-lying excited states

In case of multi-step Coulomb excitation to states above the 2_1^+ state, a combined approach between the standard version of the GOSIA code and GOSIA2 is implemented. The strategy combines the possibility to simultaneously minimize the target and projectile χ^2 in GOSIA2 and the correlated-error determination of GOSIA. The GOSIA2 χ^2-surface analysis is provided as a first approximation in which the influence of higher-order excitations is not considered. The first-order solution for $\langle 0_1^+||E2||2_1^+\rangle$ is used as absolute normalization in the second step in which GOSIA is used to include couplings to higher-lying excited states. All populated states, observed γ-ray yields and relevant spectroscopic data are included and additionally a number of "buffer" states are added to avoid artificial population build-up on top of the highest observed state. Including an $E0$ decay path in GOSIA has to be done in an indirect way by simulating the electron decay via a $M1$ transition [55]. Thus, non-existing, additional 1^+ states are included in the level scheme of the polonium isotope that take care of the $E0$ decay paths of the 0_2^+ and 2_2^+ states. As $M1$ excitation is orders of magnitudes weaker than $E2$ excitation, the 0_2^+ and 2_2^+ states are not populated via the 1^+ states. In GOSIA the target de-excitation yields are used to determine relative normalization constants that are related to the incoming beam intensity and the particle detection efficiency and link the different experimental subdivisions of the data to each other. The solution that results from the GOSIA χ^2 minimization is then fed again to GOSIA2 to check the stability of the solution for $\langle 0_1^+||E2||2_1^+\rangle$. In this step the couplings between states above the 2_1^+ state are fixed and only $\langle 0_1^+||E2||2_1^+\rangle$ and $\langle 2_1^+||E2||2_1^+\rangle$ are free parameters of the GOSIA2 fit. Iterations between GOSIA and GOSIA2 are performed until a consistent solution is reached [44].

1. ^{198}Po

The ^{94}Mo target was used to study the Coulomb excitation of ^{198}Po. Multi-step Coulomb excitation up to the 4_1^+, 2_2^+ and 0_2^+ state was observed. The first approximation with GOSIA2 yields a minimum at $\chi^2 = 3.9$ for $\langle 0_1^+||E2||2_1^+\rangle = 1.14(^{12}_{11})\,\mathrm{eb}$ and $\langle 2_1^+||E2||2_1^+\rangle = 3.6(^{17}_{14})\,\mathrm{eb}$. The first-order solution for $\langle 0_1^+||E2||2_1^+\rangle$ is then used as additional data point in the GOSIA analysis, together with the known and relevant spectroscopic information on ^{198}Po which is listed in Table 4.8. The $E2/M1$ mixing ratio that was determined in ^{202}Po is assumed to stay constant for the neighboring polonium isotopes, which is an approximation. However, as the Coulomb-excitation data is insensitive to the $M1$ component of the mixed $E2/M1$ transitions, this does not influence the extracted matrix elements.

Table 4.8: Spectroscopic information on ^{196,198}Po that was included in the GOSIA analysis. The $E2/M1$ mixing ratio that was determined in ^{202}Po is assumed to stay constant for the neighboring polonium isotopes. The $I_{2_2^+\to 2_1^+}/I_{2_2^+\to 0_1^+}$ branching ratio is the γ-ray branching ratio and does not include $E0$ components.

^{196}Po		
Observable	Value	Reference
$\tau_{2_1^+}$	11.7(15) ps	[16]
$\tau_{4_1^+}$	7.8(11) ps	[16]
$\tau_{6_1^+}$	2.9(12) ps	[16]
$I_{2_2^+\to 2_1^+}/I_{2_2^+\to 0_1^+}$	0.64(3)	[18]
$\delta(E2/M1)$	1.8(5)	[45]
^{198}Po		
Observable	Value	Reference
$I_{2_2^+\to 2_1^+}/I_{2_2^+\to 0_1^+}$	2.1(11)	[56]
$I_{0_2^+\to 0_1^+}/I_{0_2^+\to 2_1^+}$	2.2(16)	[57]
$\delta(E2/M1)$	1.8(5)	[45]

Next to the populated states, the 6_1^+ and 4_2^+ states were included as buffer states. The $E0$-decay transitions of the 0_2^+ and 2_2^+ states were simulated via $M1$ transitions through two 1^+ states that were included in the level scheme at 300 keV and at 700 keV. A χ^2 minimization is performed resulting in four different sets of matrix elements that reproduce the experimental data on a comparable level. The four different solutions represent four different relative sign combinations for the matrix elements. Solutions 1 and 2, shown in Table 4.9, represent two different solutions where $\langle 0_1^+||E2||2_2^+\rangle$ is positive. The solutions where $\langle 0_1^+||E2||2_2^+\rangle$ is negative (solutions 3 and 4) are not shown in Table 4.9 as they are not considered to be physical solutions. The relative signs of the matrix elements affect the Coulomb-excitation cross section in an important way. Every possible excitation path contributes to the cross section for multi-step Coulomb excitation to a certain excited state. As the excitation amplitude for a given path is proportional to the product of the matrix elements that are involved, the relative signs of these matrix elements play a crucial role. The signs of the products of matrix elements were varied by carefully adopting various initial values and all possible sign combinations were investigated [33, 44].

Table 4.9: Two sets of reduced transitional and diagonal $E2$ matrix elements between low-lying states in ^{196,198}Po obtained in this work. The error bars correspond to 1σ. The different solutions correspond to different relative sign combinations of the matrix elements.

^{196}Po

$\langle I_i \vert\vert E2 \vert\vert I_f \rangle [eb]$	Solution 1	Solution 2
$\langle 0_1^+ \vert\vert E2 \vert\vert 2_1^+ \rangle$	$1.32(5)$	$1.32(5)$
$\langle 0_1^+ \vert\vert E2 \vert\vert 2_2^+ \rangle$	$0.44(4)$	$-0.44(3)$
$\langle 2_1^+ \vert\vert E2 \vert\vert 2_1^+ \rangle$	$-0.2(4)$	$1.1(5)$
$\langle 2_1^+ \vert\vert E2 \vert\vert 2_2^+ \rangle$	$2.12(^{16}_{22})$	$2.04(^{15}_{18})$
$\langle 2_1^+ \vert\vert E2 \vert\vert 4_1^+ \rangle$	$2.68(11)$	$2.69(^{12}_{11})$

^{198}Po

$\langle I_i \vert\vert E2 \vert\vert I_f \rangle [eb]$	Solution 1	Solution 2
$\langle 0_1^+ \vert\vert E2 \vert\vert 2_1^+ \rangle$	$1.15(13)$	$1.15(13)$
$\langle 0_1^+ \vert\vert E2 \vert\vert 2_2^+ \rangle$	$0.25(^{11}_{4})$	$0.27(^{10}_{5})$
$\langle 2_1^+ \vert\vert E2 \vert\vert 2_1^+ \rangle$	$2.9(^{14}_{15})$	$2.4(^{16}_{14})$
$\langle 2_1^+ \vert\vert E2 \vert\vert 0_2^+ \rangle$	$1.4(^{24}_{7})$	$-1.8(^{8}_{19})$
$\langle 2_1^+ \vert\vert E2 \vert\vert 2_2^+ \rangle$	$2.8(9)$	$3.1(9)$
$\langle 2_1^+ \vert\vert E2 \vert\vert 4_1^+ \rangle$	$3.3(^{4}_{5})$	$3.2(4)$
$\langle 0_2^+ \vert\vert E2 \vert\vert 2_2^+ \rangle$	$1.2(8)$	$< 3(3)$

In solutions 3 and 4 (not shown in Table 4.9), the population of the 2_2^+ state is significantly lower than in solutions 1 and 2. In order to reproduce the experimental yields, the diagonal matrix element of the 2_1^+ state has to be increased in these solutions to unphysically large values of > 4 eb, far beyond the rotational limit. Because of these large values for the diagonal matrix element, solutions 3 and 4 are disregarded. The sign of the loop $\langle 2_1^+||E2||0_2^+\rangle \cdot \langle 0_2^+||E2||2_2^+\rangle \cdot \langle 2_2^+||E2||2_1^+\rangle$ is the only difference between solutions 1 and 2, which are shown in Table 4.9 (positive for solution 1, negative for solution 2). Changing the sign of this loop does not change the population of any of the excited states significantly. However the matrix element $\langle 0_2^+||E2||2_2^+\rangle$ reaches the lower limit 0 in solution 2, hinting towards the fact that a better solution would be obtained with a negative sign for this matrix element. When the sign of the matrix element between the 0_2^+ and 2_2^+ state is changed, the first solution is reproduced exactly in magnitude, but with a negative value for $\langle 2_1^+||E2||0_2^+\rangle$ and $\langle 0_2^+||E2||2_2^+\rangle$. However, the positive sign for the $\langle 2_1^+||E2||0_2^+\rangle \cdot \langle 0_2^+||E2||2_2^+\rangle \cdot \langle 2_2^+||E2||2_1^+\rangle$ loop is not changed. This is an argument to put solution 1 forward as the correct

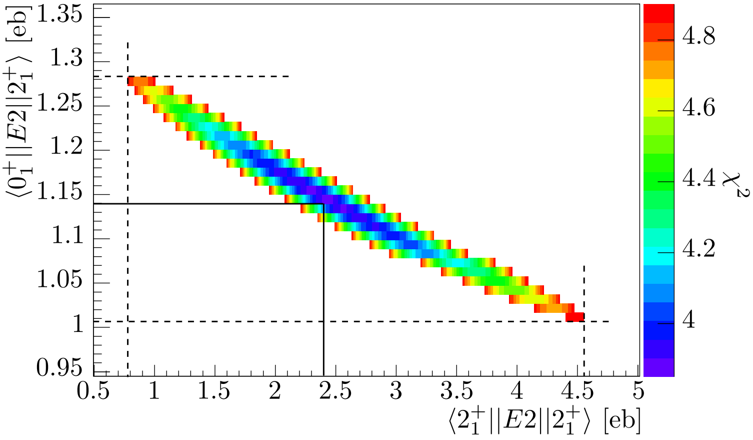

Figure 4.14: (Color online) Result of the χ^2-surface analysis for the Coulomb excitation of ^{198}Po on ^{94}Mo showing 1σ contour constructed by letting the χ^2 increase to $\chi^2_{min} + 1 = 4.9$. Projection of the 1σ contour gives the correlated uncertainties on the two parameters that are extracted.

sign combination.

The matrix elements of solution 1 are fixed in a new χ^2 analysis in GOSIA2 where only $\langle 0_1^+||E2||2_1^+\rangle$ and $\langle 2_1^+||E2||2_1^+\rangle$ are allowed to vary. The resulting 1σ contour is shown in Figure 4.14, yielding a result for both matrix elements which is consistent with the GOSIA minimum ($\langle 0_1^+||E2||2_1^+\rangle = 1.14(14)\,$eb, $\langle 2_1^+||E2||2_1^+\rangle = 2.4(^{21}_{16})\,$eb).

2. ^{196}*Po*

The Coulomb excitation of the lightest polonium isotope that was studied in this work, ^{196}Po, was examined on a ^{104}Pd target. Multi-step Coulomb excitation to the 4_1^+, 2_2^+ and 0_2^+ state was observed. The relevant spectroscopic information on ^{196}Po that is included in the GOSIA analysis is listed in Table 4.8. The first approximation with GOSIA2, with all the relevant spectroscopic information included, yields a minimum at $\chi^2_{\text{min}} = 13.1$ for $\langle 0_1^+||E2||2_1^+\rangle = 1.36\,\binom{5}{6}$ eb and $\langle 2_1^+||E2||2_1^+\rangle = 0.1\,\binom{6}{5}$ eb. The first-order solution for $\langle 0_1^+||E2||2_1^+\rangle$ is used as additional data point in the GOSIA analysis, together with the relevant spectroscopic information which is listed in Table 4.8. The $E0$ transitions of the 0_2^+ and 2_2^+ states were simulated via $M1$ transitions through two 1^+ states that were included in the level scheme at 300 keV and 650 keV. A χ^2

minimization, checking also the sensitivity on the signs of the loops of matrix elements, leads to two sets of matrix elements that reproduce the experimental data on a comparable level (see Table 4.9). A lack of experimental information on the coupling between the 0_2^+ state and the 2_1^+ and 2_2^+ states, renders it impossible to extract information on the sign and magnitude of $\langle 2_1^+||E2||0_2^+\rangle$ and $\langle 0_2^+||E2||2_2^+\rangle$. However, to make sure that the correlations to these couplings are taken into account, the matrix elements were included in the GOSIA analysis, as well as the buffer states 6_1^+ and 4_2^+. It is clear from Table 4.9 that the sign of the loop $\langle 0_1^+||E2||2_1^+\rangle \cdot \langle 2_1^+||E2||2_2^+\rangle \cdot \langle 2_2^+||E2||0_1^+\rangle$ only influences the value of the diagonal matrix element of the 2_1^+ state significantly. There is no model-independent way to distinguish between these two solutions with the present set of data.

V. DISCUSSION

Mixing between co-existing structures has a large influence on the matrix elements and depends strongly on the proximity of the energy levels of same spin. Figure 4.15 shows systematically both the level energies and transitional quadrupole moments $|Q_t|$ for $^{196-202}$Po.

The experimentally obtained results are compared with three different theoretical approaches: the beyond mean-field method (BMF), the generalized Bohr Hamiltonian (GBH) and the interacting boson model (IBM). The first two methods are based on the introduction of a mean field determined by the HFB method and the same SLy4 energy density functional. In the BMF method, the mean-field wave functions are first projected on angular momentum and particle number and then mixed with respect to the axial quadrupole moment. Spectra and transition probabilities are calculated in the laboratory frame of reference and compared directly to the experimental data [19]. In the GBH method, the mass parameters of a Bohr Hamiltonian are derived thanks to a cranking approximation to the adiabatic time-dependent Hartree-Fock method and are rescaled to take into account the fact that time-odd contributions to the mass parameters are neglected. One of the interests of this method is that it leads to calculations much less heavy than the BMF method and permits to treat triaxial quadrupole deformations [59, 60]. Note that in both methods, the only parameters are those of the energy density functional and no specific adjustments are performed in their applications to the neutron-deficient isotopes around lead. The IBM is a very convenient method to put into evidence the group properties of nuclear spectra and to classify them using group theoretical methods. However, it contains 8 parameters per isotope in the form that has been used here, which are adjusted for each isotope thanks to known experimental data. The measured energies for the yrast band up to $I = 8^+$, the states 0_2^+, 2_2^+, 2_3^+, 2_4^+, 3_1^+, 4_2^+, 4_3^+, 5_1^+ and 6_2^+ and the measured

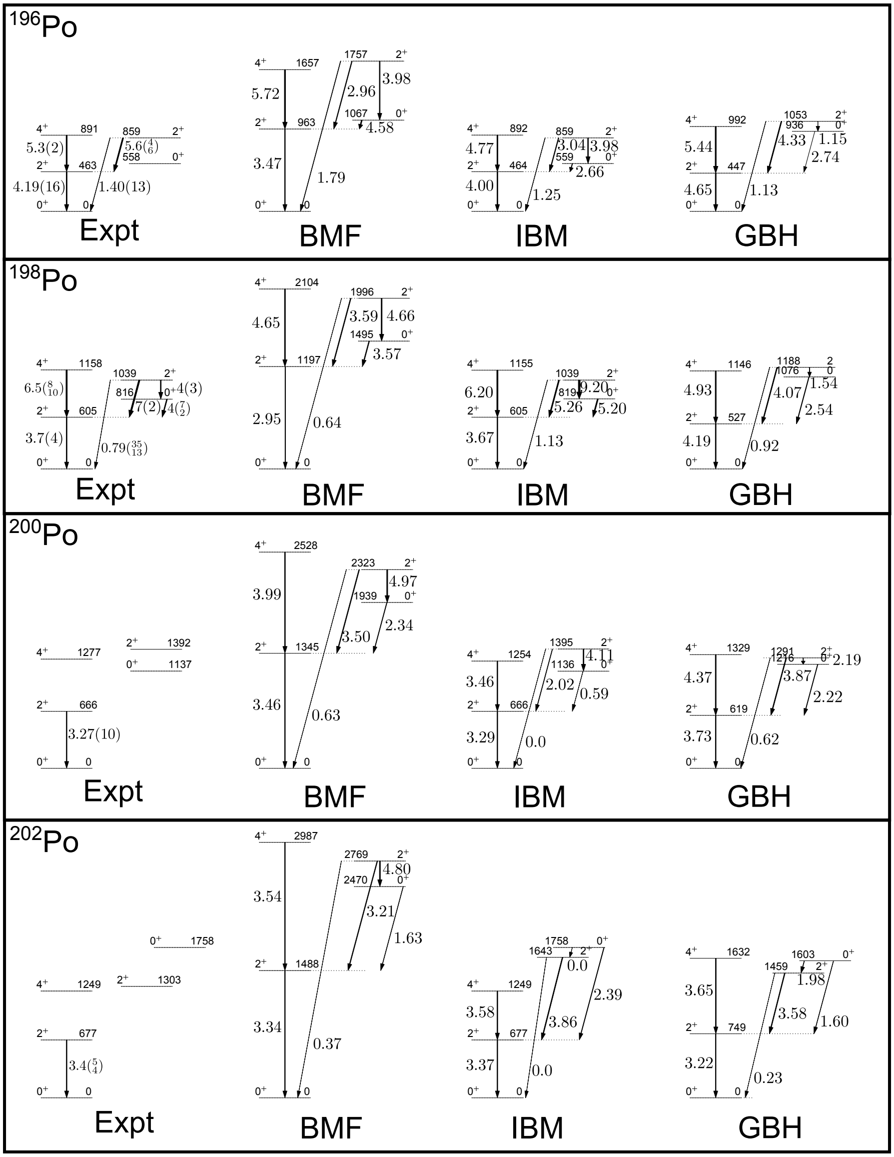

Figure 4.15: Experimental levels of the low-lying structures in ^{196,198,200,202}Po. The level energies are taken from Nuclear Data Sheets and are given in keV. Transitional $|Q_t|$ values are given in eb, based on the experimentally determined matrix elements. The width of the arrows represents the relative size of the transitional quadrupole moments $|Q_t|$. The experimental level energies and $|Q_t|$ values are compared to the same information, predicted by the BMF [19], IBM [58] and GBH models [59].

$B(E2)$ values between the above states are used to fix the parameters of the Hamiltonian through a least-squares fit. The interest of the IBM is therefore to analyze data but it is less suited to perform predictions for unknown nuclei [4].

The BMF approach overestimates the level energies in the four polonium isotopes studied here, as was noted by Yao et al. [19]. The level energies in the neighboring mercury, lead and radon isotopes are also too widely spaced in the BMF calculations. The results obtained using the GBH approach are significantly better, pointing out the importance of triaxial quadrupole deformations, although the renormalization of the GBH mass parameters does not allow a firm conclusion. The transition probabilities between the ground state and 2_1^+ state are reproduced quite well for ^{200,202}Po, suggesting a correct description of the underlying structures. For mass $A < 200$, these transition probabilities are underestimated. Further, significant differences can be noted between the transition probabilities related to the 0_2^+ and 2_2^+ states resulting from the three theoretical descriptions. The triaxial quadrupole degree of freedom included in the GBH approach does not affect significantly the transition probabilities.

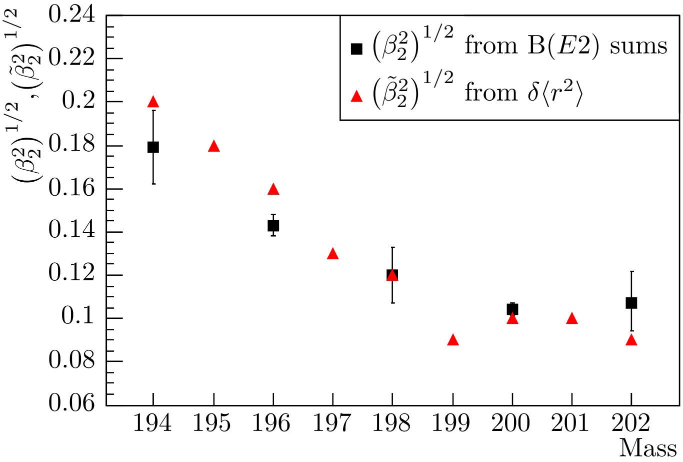

Figure 4.16: (Color online) Deformation parameters of the ground state, extracted from the charge radii $\delta\langle r^2\rangle$ (triangles) [61] and sum of squared matrix elements according to equation 4.6 (squares). For the odd isotopes the deformation parameter for the $3/2^-$ ground state is shown. The data point for ^{194}Po is deduced from the lifetime measurement [15].

Figure 4.16 shows a comparison of extracted deformation parameters obtained from the measured charge radii $\delta\langle r^2\rangle$ on the one hand and from the sum of squared matrix elements $\sum\limits_i |\langle 0_1^+||E2||2_i^+\rangle|^2$ on the other. As the parameters extracted from these two approaches are not identical, a separate notation is used. A deformation parameter, called $\tilde{\beta}_2$, was estimated from the charge radii using the expression

$$\langle r^2\rangle_A \approx \langle r^2\rangle_A^{sph}\left(1+\frac{5}{4\pi}\tilde{\beta}_2^2\right), \tag{4.5}$$

where $\langle r^2\rangle_A^{sph}$ is the mean-square charge radius of a spherical nucleus with the same volume, which was evaluated with the droplet model with a revised parametrization [61]. From the extracted $E2$ matrix elements, a deformation parameter β_2 can be deduced, through the quadrupole invariant $\langle Q^2\rangle$, using the expression

$$\sum_i |\langle 0_1^+||E2||2_i^+\rangle|^2 = \left(\frac{3}{4\pi}ZeR_0^2\right)^2\beta_2^2, \tag{4.6}$$

where a uniform charge distribution is assumed [62]. The sum of squared matrix elements $|\langle 0_1^+||E2||2_i^+\rangle|^2$ was evaluated over the 2^+ states that were populated for each case, i.e. only the 2_1^+ state in ^{200,202}Po and 2_1^+ and 2_2^+ states in ^{196,198}Po. In ^{194}Po, only the $B(E2)$ value to the 2_1^+ state is known from the lifetime measurement [15]. The onset of deviation from sphericity around $N = 112$ ($A = 196$), observed from the laser spectroscopy studies (see also Figure 4.1), is confirmed by the measured transition probabilities. An overall good agreement between the deformation parameter extracted from the charge radii and the squared matrix elements is observed within the error bars.

The experimentally determined transitional quadrupole moments $|Q_t|$ connecting the 2_1^+ and 2_2^+ states to the ground state are displayed and compared to the predictions from the BMF, IBM and GBH calculations in Figure 4.17. The same trend of increasing deformation with decreasing mass is observed from the experimental $|Q_t|$ values. The BMF $|Q_t(2_1^+ \rightarrow 0_1^+)|$ values start to deviate from the experimental values at mass $A = 198$ as noted earlier. The inclusion of the new data points, deduced in this work, shows that the three theoretical approaches reproduce the experimental values quite well.

The reproduction of the experimental $|Q_t(2_1^+ \rightarrow 0_1^+)|$ values by the IBM model follows directly from the fit that is performed to the measured $B(E2)$ values to fix the parameters of the IBM Hamiltonian. Nevertheless the experimental trend in $|Q_t(2_2^+ \rightarrow 0_1^+)|$ is predicted well by the IBM model, as well as the GBH and BMF model. The GBH model slightly overestimates the collectivity in the $2_1^+ \rightarrow 0_1^+$ transition for $^{196-200}$Po.

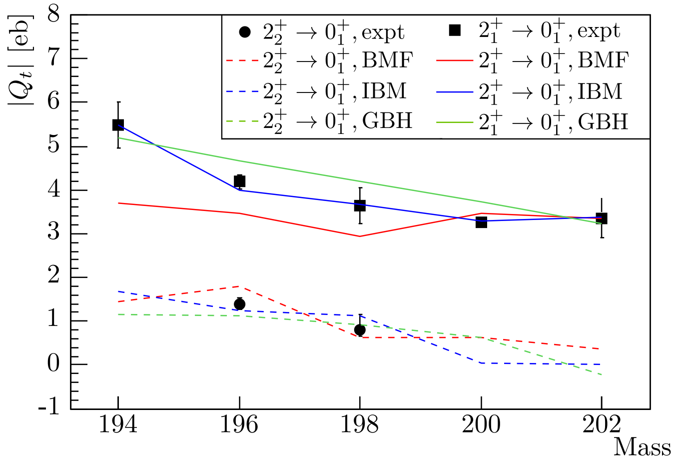

Figure 4.17: (Color online) Experimental $|Q_t|$ values, extracted from the measured matrix elements $\langle 0_1^+ || E2 || 2_1^+ \rangle$ and $\langle 0_1^+ || E2 || 2_2^+ \rangle$ in the even-even polonium nuclei as a function of mass number. Data for $A = 194$ is taken from [15]. The experimental values are compared to the predictions from three different theoretical model descriptions: the beyond-mean-field model (BMF) [19], the interacting boson model [58] and the general Bohr Hamiltonian model (GBH) [59].

The deformation of the 2_1^+ state can be understood in a Coulomb-excitation experiment through the measurement of the spectroscopic quadrupole moment Q_s. The observed trend of increasing deformation in the 2_1^+ state when going down in mass number, shown in Figure 4.18, is predicted by the three model descriptions.

A phenomenological two-state mixing model was used to calculate the $E2$ matrix elements between low-lying states in the neutron-deficient $^{182-188}$Hg isotopes [3, 26] to test the assumption that the excited states in the mercury isotopes can be described by a spin-independent interaction between two rotational structures. A common set of matrix elements within the unperturbed bands (transitional as well as diagonal $E2$ matrix elements) for the four studied mercury isotopes was found to reproduce most of the experimental results. A similar approach has been used for the polonium isotopes studied in this work. However, in the polonium isotopes a rotational structure was assumed to mix with a more spherical structure. A fit with the variable moment of inertia model (VMI) [63] of the yrast $4^+, 6^+, 8^+$ and 12^+ levels in ^{196}Po was used to determine the

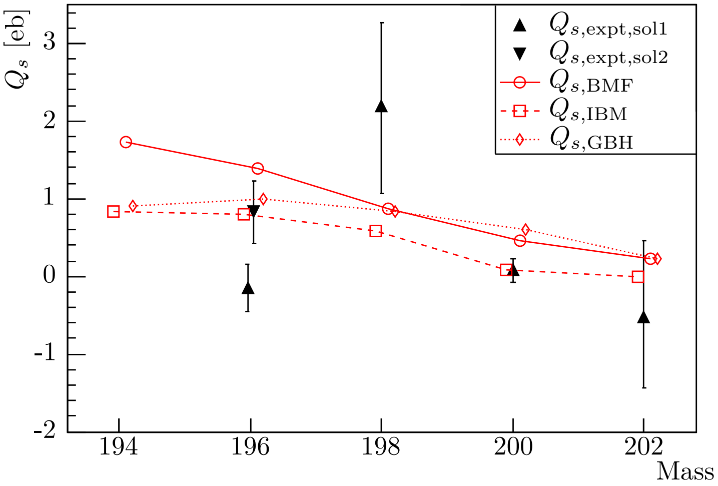

Figure 4.18: (Color online) Experimentally determined values for the spectroscopic quadrupole moment Q_s of the 2_1^+ state as a function of the mass of the polonium isotope. In ^{196}Po no model-independent distinction could be made between two solutions for the matrix elements, yielding two different results of Q_s. Both results are shown here with a small offset from integer A for clarity. The experimental results are compared to the predictions from the BMF [19], IBM [58] and GBH model [59].

unperturbed energies of the 0^+ and 2^+ rotational states. The 10^+ state was not included because of an ambiguity. In this procedure, no mixing was assumed for the states with spin $I \geq 4$. Using the unperturbed 0^+ and 2^+ rotational energies from the VMI fit, information on the size of the spin-independent mixing matrix element was extracted [33]. The mixing amplitudes, shown in Table 4.10, were determined from combining the spin-independent mixing matrix element $V = 200\,\mathrm{keV}$ with the mixed experimental level energies.

The experimental $E2$ matrix elements can then be expressed in terms of pure intraband matrix elements and a set of mixing amplitudes. No interband transitions between the unperturbed structures were allowed. A set of unperturbed matrix elements was fitted to optimally reproduce the experimental results, yielding $\langle 0_I^+||E2||2_I^+\rangle = 1.1\,\mathrm{eb}$, $\langle 0_{II}^+||E2||2_{II}^+\rangle = 1.5\,\mathrm{eb}$, $\langle 2_I^+||E2||2_I^+\rangle = -0.4\,\mathrm{eb}$ and $\langle 2_{II}^+||E2||2_{II}^+\rangle = 1.8\,\mathrm{eb}$. Here, I represents the spherical structure and II the deformed one. In the fitting procedure the unperturbed diagonal matrix elements were not allowed to cross the rotational limit compared to the intraband transitional matrix element ($|\ \langle 2^+||E2||2^+\rangle\ | < 1.19 \times \langle 0^+||E2||2^+\rangle$ [64]).

Table 4.10: Square of wave-function mixing amplitudes of the “normal” (vibrational) configuration, at spin 0^+ (α^2_{0+}) and spin 2^+ (α^2_{2+}). Details on the method applied to extract these values are provided in [33].

Isotope	α^2_{0+}	α^2_{2+}
^{194}Po	12 %	29 %
^{196}Po	85 %	50 %
^{198}Po	94 %	69 %
^{200}Po	97 %	92 %
^{202}Po	99 %	88 %

A comparison of the measured and calculated values of the $E2$ matrix elements is shown in Figure 4.19. The best fit was found with solution 2 in ^{196}Po (see Table 4.9) where the diagonal matrix element is positive and $\langle 0^+_1||E2||2^+_2\rangle$ is negative. Most of the experimental results are reproduced within the 1σ uncertainty. The total χ^2 for this fit is equal to 102, while the total χ^2 for the best fit to solution 1 is equal to 189. The extracted unperturbed $E2$ matrix elements describing the rotational structure in the polonium isotopes are comparable to those extracted in the two-state mixing approach in the mercury isotopes for the weakly deformed oblate structure, where the extracted unperturbed transitional and diagonal $E2$ matrix elements of the weakly-deformed structure are 1.2 eb and 1.8 eb respectively [3]. This supports the interpretation that a weakly deformed, oblate structure is intruding in the low-lying energy levels of the neutron-deficient polonium isotopes. The characteristics of this weakly-deformed oblate structure seem to be related to those of the oblate structure in the mercury isotopes, that mirror the polonium isotopes with respect to $Z = 82$.

VI. SUMMARY AND CONCLUSIONS

A set of matrix elements, coupling the low-lying states in the even-even neutron-deficient $^{196-202}$Po isotopes, was extracted in two Coulomb-excitation campaigns, which were performed at the REX-ISOLDE facility in CERN. In the two heaviest isotopes, ^{200,202}Po, the transitional and diagonal matrix element of the 2^+_1 state were determined. In ^{196,198}Po multi-step Coulomb excitation was observed to populate the $4^+_1, 0^+_2$ and 2^+_2 states. The relatively large uncertainty on the matrix elements related to the 0^+_2 and 2^+_2 states is due to the indirect observation of the $E0$ transitions between the 0^+_2 and 0^+_1 states and the 2^+_2 and 2^+_1 states through characteristic polonium X rays. For future experiments the electron spectrometer SPEDE will provide a direct way of detecting $E0$ transitions [65].

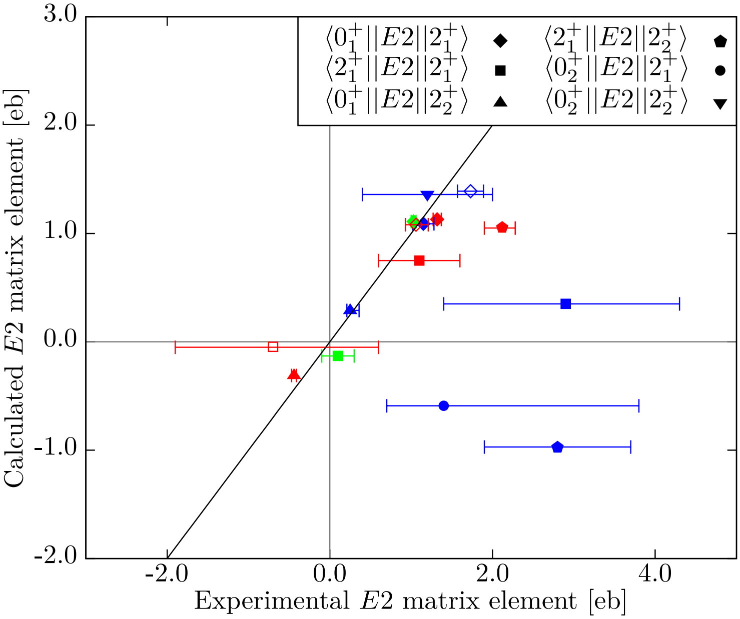

Figure 4.19: (Color online) The measured $E2$ matrix elements determined in this work, compared to those extracted from two-level mixing calculations for ^{196}Po (full red), ^{198}Po (full blue), ^{200}Po (full green), ^{202}Po (open red). The measured 1σ error bars are shown. In ^{196}Po solution 2 (see Table 4.9) is adopted. The experimental $E2$ matrix element $\langle 0_1^+||E2||2_1^+\rangle$ for ^{194}Po, shown with an open blue symbol, is deduced from the lifetime measurement [15].

The experimental results were compared to the results from the measurement of mean-square charge radii in the polonium isotopes, confirming the onset of deformation from ^{196}Po onwards. Three different model descriptions were used to compare to the data. Calculations with the beyond-mean-field model, the interacting boson model and the general Bohr Hamiltonian model show partial agreement with the experimental data. The comparison between the BMF model and GBH results does not permit a firm conclusion on the effect of triaxial quadrupole deformations. Finally, calculations with a phenomenological two-level mixing model hint towards the spin-independent mixing of a more spherical structure with a weakly-deformed oblate structure. Overall the comparison to theory would benefit from an increase in experimental sensitivity. This increased sensitivity could be reached in Coulomb-excitation experiments with higher beam energies at HIE-ISOLDE [66, 67].

ACKNOWLEDGMENTS

We acknowledge the support of the ISOLDE Collaboration and technical teams and especially the support from RILIS and REX. This work was supported by FWO-Vlaanderen (Belgium), by GOA/2010/010 (BOF KU Leuven), by the Interuniversity Attraction Poles Programme initiated by the Belgian Science Policy Office (BriX network P7/12), by the European Commission within the Seventh Framework Programme through I3-ENSAR (contract no. RII3-CT-2010-262010), by the German BMBF under contract nos. 05P12PKFNE, 06DA9036I 05P12RDCIA and 05P12RDCIB, by the UK Science and Technology Facilities Council, by the Spanish MINECO under Project No. FIS2011-28738-C02-02, by the Narodowe Centrum Nauki (Polish Center for Scientific Research), grant no. UMO-2013/10/M/ST2/00427, by the Academy of Finland (contract no. 131665) and by the European Commission through the Marie Curie Actions call PIEFGA-2008-219174 (J.P.).

---

[1] K. Heyde and J. L. Wood, Reviews of Modern Physics 83, 1467 (2011).
[2] G. Ulm et al., Zeitschrift für Physik A 325, 247 (1986).
[3] N. Bree et al., Physical Review Letters 112, 162701 (2014).
[4] J. E. García-Ramos and K. Heyde, Physical Review C 89, 014306 (2014).
[5] A. N. Andreyev et al., Nature 405, 430 (2000).
[6] R. Julin, K. Helariutta, and M. Muikku, Journal of Physics G: Nuclear and Particle Physics 27, 109 (2001).
[7] H. De Witte et al., Physical Review Letters 98, 112502 (2007).
[8] M. Seliverstov et al., Physics Letters B 719, 362 (2013).
[9] A. Oros et al., Nuclear Physics A 645, 107 (1999).
[10] N. Bijnens et al., Physical review Letters 75, 4571 (1995).
[11] T. E. Cocolios et al., Physical Review Letters 106, 052503 (2011).
[12] W. Borchers et al., Hyperfine Interactions 34, 25 (1987).
[13] T. Hilberath et al., Zeitschrift für Physik A 342, 1 (1992).
[14] F. Le Blanc, D. Lunney, J. Obert, and J. Oms, Physical Review C 60, 054310 (1999).
[15] T. Grahn et al., Physical Review Letters 97, 062501 (2006).
[16] T. Grahn et al., Physical Review C 80, 014323 (2009).
[17] C. Ellegaard et al., Nuclear Physics A 206, 83 (1973).
[18] L. Bernstein et al., Physical Review C 52, 621 (1995).
[19] J. Yao, M. Bender, and P.-H. Heenen, Physical Review C 87, 034322 (2013).
[20] J. E. García-Ramos, V. Hellemans, and K. Heyde, Physical Review C 84, 014331 (2011).
[21] K. Helariutta et al., The European Physical A 6, 289 (1999).

[22] K. Van de Vel et al., The European Physical Journal A 17, 167 (2003).
[23] G. Dracoulis, Physical Review C 49, 3324 (1994).
[24] G. Lane et al., Nuclear Physics A 589, 129 (1995).
[25] J. C. Walpe et al., Physical Review C 85, 057302 (2012).
[26] L. P. Gaffney et al., Physical Review C 89, 024307 (2014).
[27] D. Cline, Annual Reviews Nuclear Particle Science 36, 683 (1986).
[28] O. Kester et al., Nuclear Instruments and Methods in Physics Research B 204, 20 (2003).
[29] T. E. Cocolios et al., Nuclear Instruments and Methods in Physics Research B 266, 4403 (2008).
[30] B. Marsh et al., Nuclear Instruments and Methods in Physics Research B 317, 550 (2013).
[31] A. Kramida, Y. Ralchenko, J. Raeder, and NIST ASD Team (2013), NIST Atomic Spectra Database (ver. 5.1), 2013.
[32] J. Van de Walle et al., Physical Review C 79, 014309 (2009).
[33] N. Kesteloot, Deformation and mixing of co-existing shapes in the neutron-deficient polonium isotopes, PhD thesis, KU Leuven, 2015.
[34] N. Warr et al., The European Physical Journal A 49, 40 (2013).
[35] A. N. Ostrowski et al., Nuclear Instruments Methods in Physics Research A 480, 448 (2002).
[36] N. Bree et al., Nuclear Instruments and Methods in Physics Research B , to be published (2015).
[37] T. Grahn et al., EPJ Web of Conferences 63, 01009 (2013).
[38] T. Kibédi, T. Burrows, M. Trzhaskovskaya, P. Davidson, and C. Nestor, Nuclear Instruments and Methods in Physics Research A 589, 202 (2008).
[39] R. B. Firestone, Table of Isotopes, Number 4573810, John Wiley & Sons, Inc., 8th edition, 1996.
[40] M. Klintefjord, to be published.
[41] R. Stegmann, to be published.
[42] D. Abriola and A. A. Sonzogni, Nuclear Data Sheets 107, 2423 (2006).
[43] S. Basu, G. Mukherjee, and A. Sonzogni, Nuclear Data Sheets 111, 2555 (2010).
[44] L. P. Gaffney et al., European Physical Journal A , to be published (2015).
[45] N. Bijnens et al., Physical Review C 58, 754 (1998).
[46] O. Helene, Nuclear Instruments and Methods 212, 319 (1983).
[47] T. Czosnyka, D. Cline, and C. Y. Wu, Bull. Am. Phys. Soc. 28, 745 (1982).
[48] T. Czosnyka, D. Cline, and C. Y. Wu, Coulomb excitation data analysis code Gosia.
[49] S. Raman, C. Malarkey, W. Milner, C. Nestor, and P. Stelson, Atomic Data and Nuclear Data Tables 36, 1 (1987).
[50] M. Luontama, R. Julin, J. Kantele, and A. Passoja, Zeitschrift für Physik

A 324, 317 (1986).
[51] C. Fahlander, L. Hasselgren, and J. Thun, Nuclear instruments and methods 146, 329 (1977).
[52] S. Raman, C. Nestor, and P. Tikkanen, Atomic Data and Nuclear Data Tables 78, 1 (2001).
[53] P. Paradis, G. Lamoureux, R. Lecomte, and S. Monaro, Physical Review C 14, 835 (1976).
[54] J. Barrette et al., Physical Review C 6, 1339 (1972).
[55] K. Wrzosek-Lipska et al., Physical Review C , to be published (2015).
[56] M. Lach et al., Zeitschrift für Physik A 350, 207 (1994).
[57] J.Wauters et al., Zeitschrift für Physik A 344, 29 (1992).
[58] J. García-Ramos and K. Heyde, private communication.
[59] L. Próchniak, private communication.
[60] L. Próchniak and S. G. Rohoziński, Journal of Physics G: Nuclear and Particle Physics 36, 123101 (2009).
[61] M. D. Seliverstov et al., Physical Review C 89, 034323 (2014).
[62] K. Wrzosek-Lipska et al., Phys. Rev. C 86, 064305 (2012).
[63] M. Mariscotti, G. Scharff-Goldhaber, and B. Buck, Physical Review 178, 1864 (1969).
[64] A. Bohr, Rev. Mod. Phys. 48, 365 (1976).
[65] J. Konki et al., EPJ Web of Conferences 63, 01019 (2013).
[66] M. Lindroos, P. Butler, M. Huyse, and K. Riisager, Nuclear Instruments and Methods in Physics Research B 266, 4687 (2008).
[67] D. Voulot et al., IPAP-2012 Conf. Proc. C1205201, 3853 (2012).

4.2 Detailed analysis per isotope

The total statistics that was obtained in the Coulomb-excitation experiments on $^{196-202}$Po has been shown in section 4.1, in the background-subtracted and Doppler corrected spectra on the one hand, and in Table 4.3 on the other. For all studied isotopes, it was possible to divide the data into a number of angular ranges to obtain sensitivity on subtle second-order effects. The strategy that was adopted in the GOSIA analysis for each isotope, together with the main results, is also described in section 4.1. In this section, additional plots and details are provided for completeness.

4.2.1 Population of the 2_1^+ state: ^{200,202}Po nuclei

In the two heaviest isotopes that were studied in this thesis, ^{200,202}Po, only the 2_1^+ state was populated. The cross section for Coulomb excitation of this state is affected to first order by $\langle 0_1^+ || E2 || 2_1^+ \rangle$ and to second order by $\langle 2_1^+ || E2 || 2_1^+ \rangle$. The sensitivity to the reorientation effect is determined by the level of statistics as was explained in 2.1.4.

^{202}Po

Coulomb excitation of ^{202}Po was studied on a ^{94}Mo and a ^{104}Pd target. Table 4.11 shows the total and divided statistics that was acquired, together with the extracted cross section for Coulomb excitation of the populated 2_1^+ state in ^{202}Po, σ_{CE}:

$$\sigma_{\mathrm{CE},2_1^+} = \frac{N_{\gamma_{2_1^+\to 0_1^+}} \left(1 + \alpha_{2_1^+\to 0_1^+}\right) A_T}{\varepsilon_{\gamma_{2_1^+\to 0_1^+}} \rho d N_A I_b}, \tag{4.7}$$

where $N_{\gamma_{2_1^+\to 0_1^+}}$ is the observed γ-ray yield, $\alpha_{2_1^+\to 0_1^+}$ is the $E2$ conversion coefficient at the $2_1^+ \to 0_1^+$ transition energy, A_T is the mass number of the target, $\varepsilon_{\gamma_{2_1^+\to 0_1^+}}$ is the absolute detection efficiency of Miniball at the $2_1^+ \to 0_1^+$ transition energy, ρd is the target thickness and N_A is Avogadro's constant. The beam intensity, I_b, is extracted based on the known cross section for Coulomb excitation of the target and taking into account the beam (and ^{94}Mo target) purity and the Miniball detection efficiency at the respective transition energy in the target nucleus.

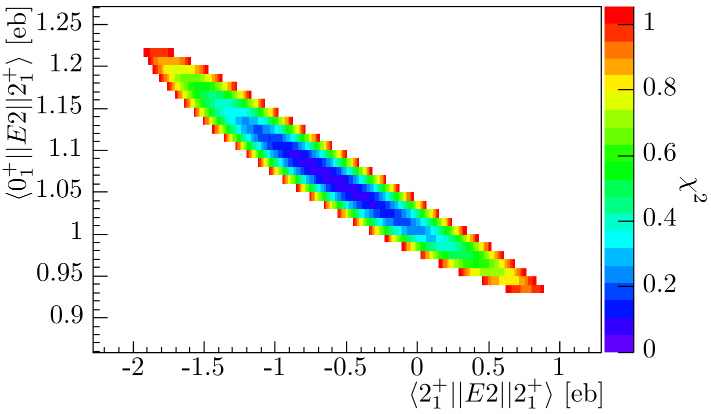

Figure 4.20: 1σ contour of the χ^2 surface of the transitional and diagonal matrix element coupling to the 2_1^+ state in ^{202}Po, constructed from the experiment on the ^{104}Pd target. The 1σ contour represents all the points with $\chi^2_{\text{min}} \leq \chi^2 \leq \chi^2_{\text{min}} + 1$, where $\chi^2_{\text{min}} = 0.06$.

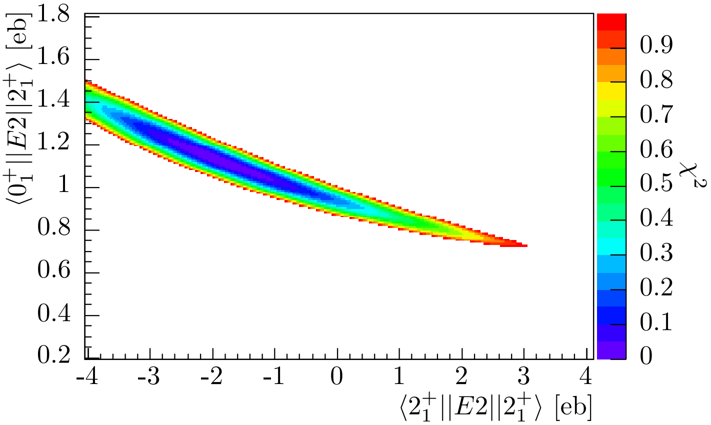

Figure 4.21: 1σ contour of the χ^2 surface of the transitional and diagonal matrix element coupling to the 2_1^+ state in ^{202}Po, constructed from the experiment on the ^{94}Mo target. The 1σ contour represents all the points with $\chi^2_{\text{min}} \leq \chi^2 \leq \chi^2_{\text{min}} + 1$, where $\chi^2_{\text{min}} = 3.7 \times 10^{-5}$.

Table 4.11: Statistics gathered in the Coulomb-excitation experiment of ^{202}Po on ^{104}Pd and on ^{94}Mo. θ_{lab} is the scattering angle in the laboratory frame of reference, N_γ represents the number of detected γ rays at the Miniball setup and σ_{CE} is the deduced cross section for Coulomb excitation to the 2_1^+ state in barn.

^{202}Po on ^{104}Pd				
Nucleus	Transition	θ_{lab}	N$_\gamma$	σ_{CE} [b]
^{202}Po	$2_1^+ \to 0_1^+$	26.1° – 57.1°	$3.8(3) \times 10^2$	0.45(6)
		26.1° – 40.9°	167(17)	
		41.0° – 49.4°	122(15)	
		49.5° – 57.1°	99(13)	
^{104}Pd	$2_1^+ \to 0_1^+$	26.1° – 57.1°	$10.4(4) \times 10^2$	
		26.1° – 40.9°	$4.2(3) \times 10^2$	
		41.0° – 49.4°	$3.3(2) \times 10^2$	
		49.5° – 57.1°	$2.7(2) \times 10^2$	
^{202}Po on ^{94}Mo				
Nucleus	Transition	θ_{lab}	N$_\gamma$	σ_{CE} [b]
^{202}Po	$2_1^+ \to 0_1^+$	26.1° – 57.1°	$2.2(2) \times 10^2$	0.39(8)
		26.1° – 45.5°	135(14)	
		45.5° – 57.1°	87(14)	
^{94}Mo	$2_1^+ \to 0_1^+$	26.1° – 57.1°	75(13)	
		26.1° – 45.5°	50(9)	
		45.5° – 57.1°	27(10)	

The low total statistics gathered on the ^{94}Mo target excitation only allowed for two subdivisions, while the data on the ^{104}Pd target was divided into three subdivisions. Figure 4.20 shows the 1σ contour of the χ^2 surface, constructed with the data on the ^{104}Pd target. In this, χ^2 is defined as

$$\chi^2 = N_T^{\text{data}} \chi^2_{T,\text{GOSIA}} + N_P^{\text{data}} \chi^2_{P,\text{GOSIA}}, \tag{4.8}$$

where $N_{T(P)}^{\text{data}}$ represents the number of data points for the target (projectile) and $\chi^2_{T(P),\text{GOSIA}}$ is the reduced χ^2 value that is given by GOSIA as output. The number of data points is defined as explained in 2.2. Using this definition leads to $N_P^{\text{data}} = 3$ and $N_T^{\text{data}} = 5$ for the experiment on the ^{104}Pd target (including two ^{104}Pd matrix elements from literature) and $N_P^{\text{data}} = 2$ and $N_T^{\text{data}} = 4$ for the experiment on the ^{94}Mo target (including two ^{94}Mo matrix elements from literature). The very small χ^2_{min} value for the χ^2 surface constructed from the ^{94}Mo data is due to the small number of subdivisions that was adopted in this case. With only two data points for the projectile (the two yields mentioned in Table 4.11) and two free parameters (the transitional and diagonal matrix element in ^{202}Po), the problem has one exact solution with a vanishing χ^2 value. Effectively, this is the same as the fitting of a straight line through two data points. The χ^2_{min} value is not exactly equal to zero, as there is also a contribution from the information on the target excitation. However, in this case the relative error on the ^{94}Mo yields is large (see Table 4.11), which gives rise to a small χ^2_{min} value.

Projection of the 1σ contour on both axes gives the correlated uncertainties on the two parameters that are extracted: $\langle 0_1^+||E2||2_1^+\rangle = 1.06\,\binom{16}{14}$ eb, $\langle 2_1^+||E2||2_1^+\rangle = -0.6\,\binom{15}{13}$ eb. The 1σ contour, representing the data on the ^{94}Mo target, is shown in Figure 4.21. The small number of subdivisions clearly limits the sensitivity on the second-order effect of the diagonal matrix element, as is reflected by the large uncertainties that are extracted: $\langle 0_1^+||E2||2_1^+\rangle = 1.1\,(4)$ eb, $\langle 2_1^+||E2||2_1^+\rangle = -2\,(5)$ eb. Important to notice is that the results, extracted independently from the data on the two targets, are consistent with each other. Despite the lack of sensitivity to the second-order effect in the ^{94}Mo data, combining the data on the two targets improves the uncertainties on both extracted parameters: $\langle 0_1^+||E2||2_1^+\rangle = 1.06\,\binom{15}{13}$ eb, $\langle 2_1^+||E2||2_1^+\rangle = -0.7\,\binom{13}{12}$ eb. Figure 4.22 shows the final 1σ contour, where χ^2 is defined as:

$$\chi^2 = \chi^2_{^{94}\text{Mo}} + \chi^2_{^{104}\text{Pd}}, \tag{4.9}$$

with $\chi^2_{^{94}\text{Mo}}$ and $\chi^2_{^{104}\text{Pd}}$ defined by equation 4.8.

Figure 4.23 represents a method to extract the value and error bar of the transitional matrix element $\langle 0_1^+||E2||2_1^+\rangle$, under the assumption that second-order effects do not influence the Coulomb-excitation experiment. A value of 0 is assumed for the diagonal matrix element of the 2_1^+ state. Fixing the value of the diagonal matrix element, effectively means taking a vertical cut of the χ^2 surface at $\langle 2_1^+||E2||2_1^+\rangle = 0$ eb. The result is shown in Figure 4.23, which also shows the $\chi^2_{\text{min}} + 1$ line, determining the uncertainty on the extracted transitional matrix element. The value, $\langle 0_1^+||E2||2_1^+\rangle(Q = 0) = 0.99(4)$ eb, has a smaller error bar that reflects the quality of the data, without including the correlation between the first-order and second-order effects. The extracted error bar contains the statistical error on the measured (projectile and target) γ-ray yields, the relative uncertainty on the γ-ray detection efficiencies at the relevant energies, the uncertainty on the beam and target purity and the tabulated error bars on the matrix elements of the target nucleus. However, by ignoring the correlation to the diagonal matrix element, only part of the physics of the Coulomb-excitation experiment is reflected. It seems thus recommended to

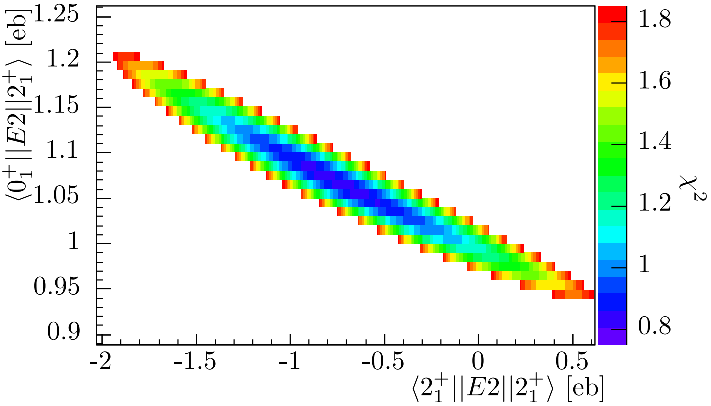

Figure 4.22: 1σ contour of the χ^2 surface of the transitional and diagonal matrix element coupling to the 2_1^+ state in ^{202}Po, constructed from a combination of the experiments on the ^{94}Mo and ^{104}Pd targets. The 1σ contour represents all the points with $\chi^2_{\text{min}} \leq \chi^2 \leq \chi^2_{\text{min}} + 1$, where $\chi^2_{\text{min}} = 0.8$.

quote the error bars including the correlations. However, a future measurement of the quadrupole moment or the lifetime of the 2_1^+ state can be folded into the χ^2 surface. In the case of a value for the lifetime of the 2_1^+ state, a horizontal cut of the χ^2 surface at the appropriate value leads to a new estimate for the diagonal matrix element of the 2_1^+ state.

^{200}Po

The ^{104}Pd target was used to study Coulomb excitation of ^{200}Po. All of the 2009 beam time (more than 40 hours) was devoted to study this isotope, so enough statistics was collected to analyze the data strip by strip. This means that a total of 14 subdivisions was defined. The total and divided statistics are listed in Table 4.12, together with the deduced cross section for Coulomb excitation of the populated 2_1^+ state in ^{200}Po, σ_{CE}. The cross section was calculated following the same procedure as in ^{202}Po, i.e. equation 4.7.

The 1σ contour, resulting from the χ^2 analysis in GOSIA2, taking into account the data in Table 4.12, is shown in Figure 4.24. The level of statistics ensures a good sensitivity on the value of the diagonal matrix element of the 2_1^+ state: $\langle 0_1^+||E2||2_1^+\rangle = 1.03\,(3)$ eb, $\langle 2_1^+||E2||2_1^+\rangle = 0.1\,(2)$ eb. A consistency check was performed, dividing the data into 6 subdivisions instead of 14.

Table 4.12: Statistics gathered in the Coulomb-excitation experiment of ^{200}Po on ^{104}Pd. θ_{lab} is the scattering angle in the laboratory frame of reference, N_γ represents the number of detected γ rays at the Miniball setup and σ_{CE} is the deduced cross section for Coulomb excitation in barn.

Nucleus	Transition	θ_{lab}	N_γ	σ_{CE} [b]
^{200}Po	$2_1^+ \rightarrow 0_1^+$	21.8° – 51.6°	$19.30(18) \times 10^3$	0.48(3)
		21.8° – 24.7°	$0.80(5) \times 10^3$	
		24.8° – 27.5°	$1.11(5) \times 10^3$	
		27.6° – 30.2°	$1.24(5) \times 10^3$	
		30.3° – 32.8°	$1.24(5) \times 10^3$	
		32.9° – 35.2°	$1.39(5) \times 10^3$	
		35.3° – 37.5°	$1.36(5) \times 10^3$	
		37.6° – 39.7°	$1.43(5) \times 10^3$	
		39.7° – 41.7°	$1.54(5) \times 10^3$	
		41.7° – 43.6°	$1.29(5) \times 10^3$	
		43.6° – 45.4°	$1.53(5) \times 10^3$	
		45.4° – 47.1°	$1.45(5) \times 10^3$	
		47.1° – 48.7°	$1.40(5) \times 10^3$	
		48.7° – 50.2°	$1.50(6) \times 10^3$	
		50.2° – 51.6°	$1.44(6) \times 10^3$	
^{104}Pd	$2_1^+ \rightarrow 0_1^+$	21.8° – 51.6°	$43.7(3) \times 10^3$	
		21.8° – 24.7°	$1.93(7) \times 10^3$	
		24.8° – 27.5°	$2.95(7) \times 10^3$	
		27.6° – 30.2°	$3.11(7) \times 10^3$	
		30.3° – 32.8°	$3.05(8) \times 10^3$	
		32.9° – 35.2°	$3.22(8) \times 10^3$	
		35.3° – 37.5°	$3.34(8) \times 10^3$	
		37.6° – 39.7°	$3.25(8) \times 10^3$	
		39.7° – 41.7°	$3.47(8) \times 10^3$	
		41.7° – 43.6°	$2.92(7) \times 10^3$	
		43.6° – 45.4°	$3.27(8) \times 10^3$	
		45.4° – 47.1°	$3.00(8) \times 10^3$	
		47.1° – 48.7°	$2.92(8) \times 10^3$	
		48.7° – 50.2°	$2.97(8) \times 10^3$	
		50.2° – 51.6°	$3.02(9) \times 10^3$	

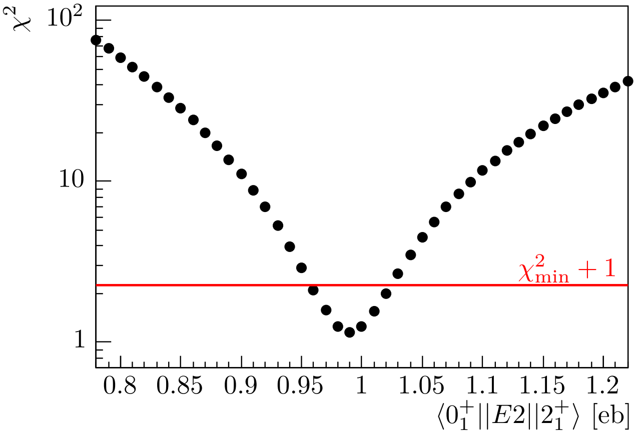

Figure 4.23: One-dimensional cut of the total χ^2 surface on ^{202}Po, at $\langle 2_1^+||E2||2_1^+\rangle = 0\,\text{eb}$, representing the total χ^2 value as a function of the value of the transitional matrix element $\langle 0_1^+||E2||2_1^+\rangle$. The red line represents $\chi^2_{\text{min}}+1$, where $\chi^2_{\text{min}} = 1.2$ in this case.

Figure 4.25 shows a comparison of the 1σ contours resulting from both analysis methods. The 1σ contours are observed to overlap, which means that both methods produce consistent results. A slight decrease in the uncertainty on the diagonal matrix element can be observed upon increasing the number of subdivisions from 6 ($\langle 0_1^+||E2||2_1^+\rangle = 1.01\,(3)\,\text{eb}$, $\langle 2_1^+||E2||2_1^+\rangle = 0.2\,(3)\,\text{eb}$) to 14. It is thus recommended to maximize the number of subdivisions, without increasing the relative uncertainty on the individual γ-ray yields per subdivision to unreasonable values. As formulating a rule of thumb for the balance between the number of subdivisions and the relative error on the individual yields is difficult, each case should be studied independently.

From Figure 4.25 it is clear that the two analysis methods, with 14 and 6 subdivisions, produce consistent results. The number of subdivisions has an influence on the extracted uncertainty of the matrix elements. Next to that, the value for the matrix elements also shifts (non-significantly) when comparing the two results. This is a statistical effect and does not contain any physics. Figure 4.26 visualizes how the 1σ contour is constructed, for the case of 14 subdivisions. The 1σ contour is the result of the overlap of 14 separate 1σ contours, resulting from each experiment (angular range) individually and represented as bands in Figure 4.26. The curvature of the individual bands increases with increasing centre-of-mass scattering angle, reflecting an increased

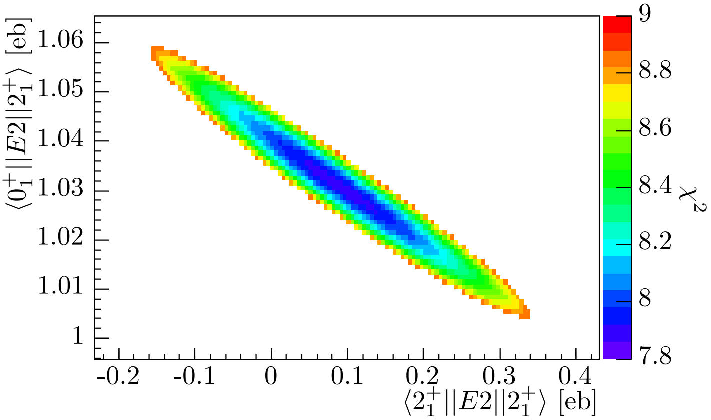

Figure 4.24: 1σ contour of the χ^2 surface of the transitional and diagonal matrix element coupling to the 2_1^+ state in ^{200}Po, constructed from the GOSIA2 analysis where the data was subdivided in 14 angular ranges. The 1σ contour represents all the points with $\chi^2_{\text{min}} \leq \chi^2 \leq \chi^2_{\text{min}} + 1$, where $\chi^2_{\text{min}} = 7.9$.

sensitivity to the second-order effect at larger centre-of-mass scattering angles. When only 6 subdivisions are adopted, the number of bands is smaller and the overlap of the bands with different curvature is slightly different. This can give rise to a shift in extracted value but this is a purely statistical effect.

Finally, Figure 4.27 shows the method of error determination under the assumption that there is no influence of second-order effects. The χ^2 surface is projected at $\langle 2_1^+ || E2 || 2_1^+ \rangle = 0\,\text{eb}$, resulting in $\langle 0_1^+ || E2 || 2_1^+ \rangle (Q = 0) = 1.040(8)\,\text{eb}$ as result for the transitional matrix element. The error bar on this value contains the statistical error on the measured (projectile and target) γ-ray yields, the relative uncertainty on the γ-ray detection efficiencies at the relevant energies, the uncertainty on the beam purity and the tabulated error bars on the matrix elements of the target nucleus.

4.2.2 Multi-step Coulomb excitation: ^{196,198}Po nuclei

Multi-step Coulomb excitation was observed to populate several low-lying excited states above the 2_1^+ state in the two lightest isotopes that were studied, ^{196,198}Po. In this case, all the couplings between the populated states need to be taken into account in the GOSIA analysis. A combined approach between

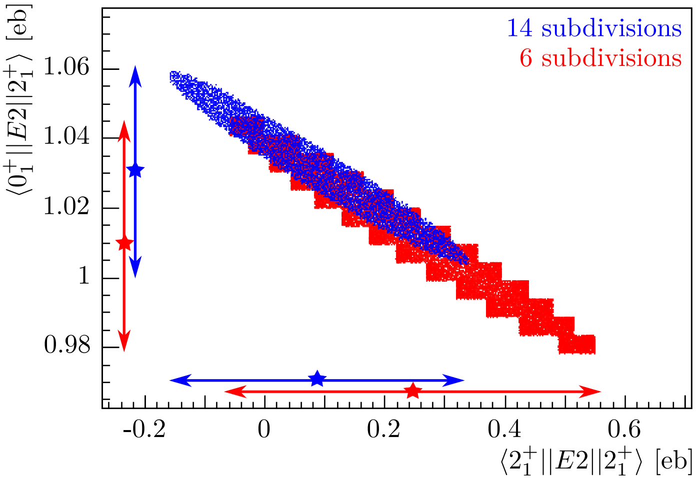

Figure 4.25: 1σ contours of the χ^2 surface in ^{200}Po, constructed from the GOSIA2 analysis with 14 ranges (in blue) and 6 ranges (in red). The 1σ contour represents all the points with $\chi^2_{\text{min}} \leq \chi^2 \leq \chi^2_{\text{min}} + 1$, where $\chi^2_{\text{min}} = 7.9$ in the case of 14 subdivisions and $\chi^2_{\text{min}} = 0.6$ in the case of 6 subdivisions. The extracted value for both matrix elements is illustrated with a star (in blue for the analysis with 14 subdivisions and in red for the analysis with 6 subdivisions) and an arrow, indicating the 1σ uncertainty.

standard GOSIA and GOSIA2, of which the principle is described in [72] and the details related to this case are given in section 4.1, has been applied.

^{198}Po

Observed transitions A ^{94}Mo target was used to study Coulomb excitation of ^{198}Po. As the collected statistics on the $2_1^+ \rightarrow 0_1^+$ transition in the ^{94}Mo target nucleus was significantly lower than the statistics on the $2_1^+ \rightarrow 0_1^+$ γ ray in ^{198}Po, the optimal number of subdivisions was based on the relative uncertainty on the target yield. The best trade-off between increased sensitivity to second-order effects and increased relative uncertainty on the yields was found at five subdivisions. A consistency check was performed, adopting three and seven subdivisions. Figure 4.28 shows the low-lying excited levels of ^{198}Po that were included in the GOSIA analysis, including the 6_1^+ and 4_2^+ buffer states that were not populated in the experiment, together with a schematic representation of the observed yields. The total and divided statistics that were adopted in

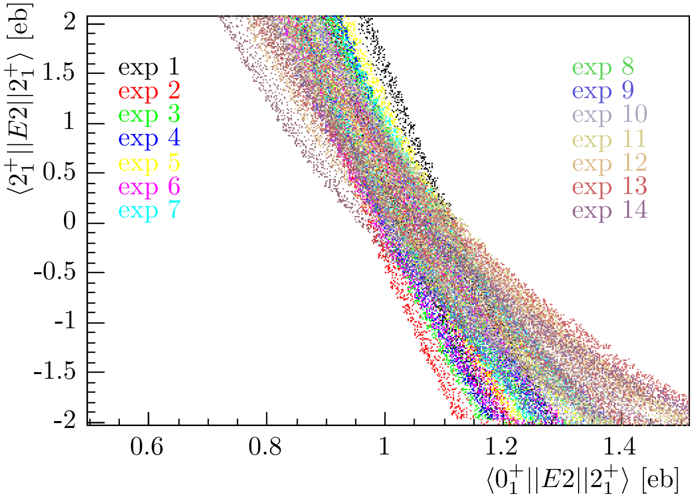

Figure 4.26: Two-dimensional χ^2 plot with respect to $\langle 0_1^+||E2||2_1^+\rangle$ and $\langle 2_1^+||E2||2_1^+\rangle$ for ^{200}Po on ^{104}Pd. The data was sub-divided into 14 different scattering angular ranges and their individual 1σ limits are represented by the different bands; in increasing order of centre of mass scattering angle these are: black, red, bright green, dark blue, yellow, pink, light blue, green, purple, grey, yellow ochre, orange, dark red, dark purple.

the GOSIA analysis are shown in Table 4.13, which also lists the calculated Coulomb-excitation cross section to each populated state, σ_{CE}.

Multi-step Coulomb excitation was observed in ^{198}Po to the 4_1^+, 0_2^+ and 2_2^+ states (see level scheme in Figure 4.28). The background-subtracted γ-ray spectrum and the gated $\gamma\gamma$-energy spectrum, shown in section 4.1 show clearly the $2_1^+ \rightarrow 0_1^+$ and $4_1^+ \rightarrow 2_1^+$ transitions and show a weak indication of the transitions depopulating the 0_2^+ and 2_2^+ states.

The particle-gated $\gamma\gamma$-energy spectrum also contains polonium X rays, which can be attributed to the conversion of observed coincident γ rays and to the $E0$ component of the $2_2^+ \rightarrow 2_1^+$ transition. The $4_1^+ \rightarrow 2_1^+$ transition, which is observed clearly in both the “singles” particle-gated γ-ray energy spectrum as in the particle-gated $\gamma\gamma$ spectrum, is used to link the intensity in the $\gamma\gamma$ spectrum

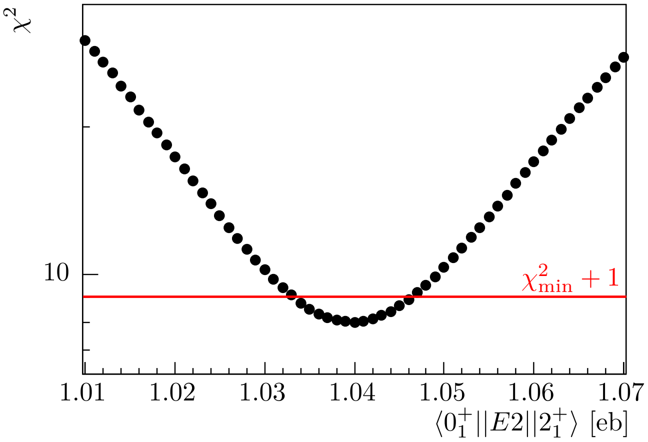

Figure 4.27: One-dimensional cut of the total χ^2 surface on ^{200}Po, at $\langle 2_1^+||E2||2_1^+\rangle = 0\,$eb, representing the total χ^2 value as a function of the value of the transitional matrix element $\langle 0_1^+||E2||2_1^+\rangle$. The red line represents $\chi^2_{\rm min} + 1$, where $\chi^2_{\rm min} = 8.0$ in this case.

to the "singles" intensity. A scaling factor S is defined as

$$S = \frac{I_{4_1^+ \to 2_1^+,\rm singles}}{I_{4_1^+ \to 2_1^+,\rm coincidences}} \tag{4.10}$$

and is equal to 10(4) in this case. Of the 9(10) counts in the polonium K_α X-ray peak in the $\gamma\gamma$ spectrum, 3(1) counts can be attributed to the $E2(/M1)$ conversion of the $4_1^+ \to 2_1^+$, $2_2^+ \to 2_1^+$ and $0_2^+ \to 2_1^+$ transitions. The $E2/M1$ conversion coefficient of the mixed $2_2^+ \to 2_1^+$ γ-ray transition was calculated assuming an $E2/M1$ mixing ratio $\delta = 1.8(5)$, which was based on the $E2/M1$ $2_2^+ \to 2_1^+$ conversion coefficient in ^{202}Po, as this is the only mixing ratio that was measured for the polonium isotopes [37]. The error bar of the calculated conversion coefficient was increased to allow for variation in $E2/M1$ mixing ratio δ.

As a negligible amount of "atomic" K_α X rays is expected to be coincident with the $2_1^+ \to 0_1^+$ transition, the remaining 6(10) coincident K_α X rays (corresponding to 60(100) K_α X rays in the singles spectrum) must be related to the $E0$ part of the $2_2^+ \to 2_1^+$ transition. In the total Coulomb-excitation γ-ray spectrum, 1160(100) K_α X rays are detected of which 117(17) result from $E2/M1$ conversion of observed $E2(/M1)$ transitions and 880(190) are

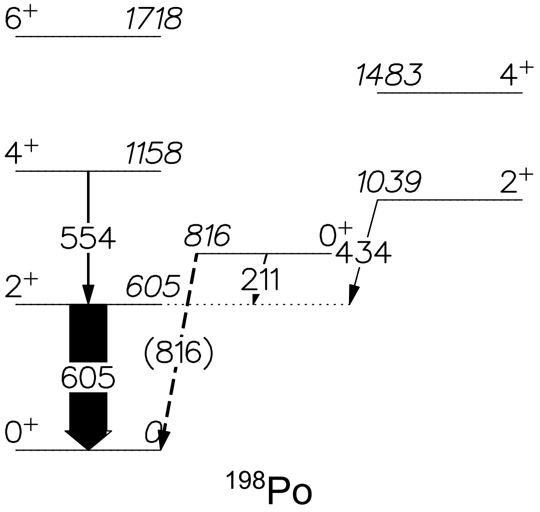

Figure 4.28: Level scheme of ^{198}Po, showing the levels that were included in the GOSIA analysis with their spin and parity and energy in keV. The observed transitions are illustrated with black arrows of which the width represents the intensity. The dashed line shows the $E0$ transition between the 0_2^+ state and the ground state.

estimated to originate from the K-vacancy creation process. This yields an excess of 220(280) X rays that can be related to $E0$ processes. Subtracting the deduced amount of 76(130) X rays associated with $E0$ $2_2^+ \to 2_1^+$ transitions, leaves 145(310) X rays that can be attributed to the $E0$ transition between the excited 0^+ state and the ground state. The large uncertainties on these numbers are due to the indirect method of determining these intensities.

Determination of cross section for Coulomb excitation In this case, where multiple low-lying states are populated, the calculation of the Coulomb-excitation cross section is not simply a translation of observed γ-ray yield into cross section as in equation 4.7. Other feeding and decay paths have to be taken into account in the calculation:

$$\sigma_{\mathrm{CE},i} = \frac{N_{\gamma_{i\to f},corr} A_T}{b f_{i\to f} \varepsilon_{\gamma_{2_1^+\to 0_1^+}} \rho d N_A I_b}, \tag{4.11}$$

Table 4.13: Statistics gathered in the Coulomb-excitation experiment of ^{198}Po on ^{94}Mo. θ_{lab} is the scattering angle in the laboratory frame of reference, N_γ represents the number of detected γ rays at the Miniball setup and σ_{CE} is the deduced cross section for Coulomb excitation in barn.

Nucleus	Transition	θ_{lab}	N_γ	σ_{CE} [b]
^{198}Po	$2_1^+ \to 0_1^+$	$26.1° - 57.1°$	$4.60(8) \times 10^3$	1.00(16)
		$26.1° - 35.6°$	$0.86(4) \times 10^3$	
		$35.6° - 40.9°$	$0.94(4) \times 10^3$	
		$41.0° - 45.5°$	$0.78(3) \times 10^3$	
		$45.5° - 51.2°$	$0.81(3) \times 10^3$	
		$51.2° - 57.1°$	$1.14(4) \times 10^3$	
	$4_1^+ \to 2_1^+$	$26.1° - 57.1°$	171(39)	0.038(11)
	$0_2^+ \to 2_1^+$	$26.1° - 57.1°$	78(58)	0.03(4)
	$2_2^+ \to 2_1^+$	$26.1° - 57.1°$	34(40)	0.010(12)
^{94}Mo	$2_1^+ \to 0_1^+$	$26.1° - 57.1°$	$5.3(3) \times 10^2$	
		$26.1° - 35.6°$	105(16)	
		$35.6° - 40.9°$	132(14)	
		$41.0° - 45.5°$	100(13)	
		$45.5° - 51.2°$	84(12)	
		$51.2° - 57.1°$	126(14)	

where $bf_{i\to f}$ is the branching fraction, which is defined as:

$$bf_{i\to f} = \frac{I_{i\to f}}{\sum\limits_k I_{i\to k}\left(1+\alpha_{i\to k}\right)}, \tag{4.12}$$

in which the summation runs over the final states k where state i can decay to, including f. $N_{\gamma_{i\to f},corr}$ represents the γ-ray yield, corrected for other feeding paths:

$$N_{\gamma_{i\to f},corr} = \frac{N_{\gamma_{i\to f}}}{\varepsilon_{i\to f}} - \sum_j \frac{N_{\gamma_{j\to i}}\left(1+\alpha_{j\to i}\right)}{\varepsilon_{j\to i}}. \tag{4.13}$$

In this case the summation runs over the states j that provide feeding to state i.

In the calculation of the observed Coulomb-excitation cross sections for ^{198}Po, a few assumptions are made because of missing information. The total conversion coefficient of the mixed $E0/M1/E2$ $2_2^+ \to 2_1^+$ transition is unknown. The observed γ-ray and $E0$ yields in this study have large error bars which makes it

Table 4.14: Four sets of reduced transitional and diagonal $E2$ matrix elements coupling low-lying states in ^{198}Po, obtained in this work. The error bars represent 1σ. The different solutions correspond to different relative sign combinations of the matrix elements. χ^2_{min} represents the total χ^2 value in the minimum, taking into account the total number of data points.

$\langle \text{I}_i \| E2 \| \text{I}_f \rangle [eb]$	Solution 1	Solution 2	Solution 3	Solution 4
$\langle 0_1^+ \| E2 \| 2_1^+ \rangle$	$1.15(13)$	$1.15(13)$	$1.10(^{17}_{11})$	$1.10(^{17}_{11})$
$\langle 0_1^+ \| E2 \| 2_2^+ \rangle$	$0.25(^{11}_{4})$	$0.27(^{10}_{5})$	$-0.08(^{2}_{3})$	$-0.023(^{4}_{29})$
$\langle 2_1^+ \| E2 \| 2_1^+ \rangle$	$2.9(^{14}_{15})$	$2.4(^{16}_{14})$	$4.6(^{4}_{17})$	$4.0(^{10}_{11})$
$\langle 2_1^+ \| E2 \| 0_2^+ \rangle$	$1.4(^{24}_{7})$	$-1.8(^{8}_{19})$	$1.6(^{6}_{7})$	$-1.7(^{9}_{3})$
$\langle 2_1^+ \| E2 \| 2_2^+ \rangle$	$2.8(9)$	$3.1(9)$	$0.9(^{4}_{3})$	$0.26(^{49}_{9})$
$\langle 2_1^+ \| E2 \| 4_1^+ \rangle$	$3.3(^{4}_{5})$	$3.2(4)$	$3.5(^{4}_{5})$	$3.3(^{4}_{5})$
$\langle 0_2^+ \| E2 \| 2_2^+ \rangle$	$1.2(8)$	$< 3(3)$	$3.4(^{11}_{22})$	$3.9(^{6}_{31})$
χ^2_{min}	0.3	0.3	0.3	0.9

impossible to get an estimate with a reasonable precision from this data set. Therefore, the measured mixing ratio $\delta(E2/M1) = 1.8(5)$ for the $2_2^+ \to 2_1^+$ transition in ^{202}Po [37] was used to estimate the total conversion coefficient of the $2_2^+ \to 2_1^+$ transition. Furthermore, as the $2_2^+ \to 0_2^+$ transition was not observed in this study or in previous decay studies [23, 34], its intensity was assumed to be zero in the calculation of the branching fraction of the 2_2^+ decay.

GOSIA analysis The combined approach using standard GOSIA and GOSIA2, employing the data given in Table 4.13 and the relevant spectroscopic information on ^{198}Po, which is shown in Table 4.8, yields four different solutions, shown in Table 4.14. They represent four different combinations of the relative signs of the matrix elements coupling to the 2_2^+ state, as described in section 2.1.4. The total χ^2 values in the minimum were calculated from the GOSIA output using the total number of data points for the ^{198}Po projectile. The 9 γ-ray yields, shown in Table 4.13, 2 $E0$ yields depopulating the 0_2^+ and 2_2^+ states, 2 branching ratios, 1 $E2/M1$ mixing ratio δ and 1 matrix element $\langle 0_1^+ \| E2 \| 2_1^+ \rangle$ sum to a total of 15 data points.

Next to the matrix elements reported in Table 4.14, additional matrix elements were included in the GOSIA analysis. The experimental data set did not allow to extract values for these matrix elements, but they were included to make sure

Table 4.15: Relative population of the low-lying excited states involved in the GOSIA analysis of ^{198}Po. The population is calculated for the four different solutions shown in Table 4.14 and takes into account the integration over scattering angle and bombarding energy. The uncertainty on the relative population is determined by folding in the experimental uncertainty on the matrix elements coupling to the respective state.

Populated state	Solution 1	Solution 2	Solution 3	Solution 4
2_1^+	93(3) %	93(3) %	94.3(13) %	94.7(17) %
0_2^+	2(3) %	2(2) %	1.8(8) %	2.0(11) %
2_2^+	1.4(10) %	1.6(15) %	0.8(5) %	0.3(3) %
4_1^+	3.1(6) %	2.9(5) %	3.1(6) %	2.9(6) %

that the additional correlations were taken into account in the GOSIA analysis. This means that the extracted uncertainties mentioned in Table 4.14 include possible variations for these additional matrix elements. The starting values for these extra matrix elements were determined as follows:

- $\langle 4_1^+||E2||6_1^+\rangle$: estimated from the rigid rotor model, using $\langle 0_1^+||E2||2_1^+\rangle$
- $\langle 2_2^+||E2||4_2^+\rangle$: estimated from the rigid rotor model, applied to the non-yrast band, using $\langle 0_2^+||E2||2_2^+\rangle$
- $\langle 2_1^+||M1||2_2^+\rangle$: related to $\langle 2_1^+||E2||2_2^+\rangle$ through the $E2/M1$ mixing ratio δ
- $\langle 2_2^+||E2||2_2^+\rangle$: assumed to be zero.

In the final GOSIA analysis, these four matrix elements were free to vary in a physically reasonable range. The observed sensitivity was not sufficient to report values on them. This was to be expected as no experimental information related to these matrix elements was obtained from the data set. Finally, “virtual” $M1$ matrix elements were added to take care of the $E0$ component of the 0_2^+ and 2_2^+ states [78]. These matrix elements couple the 0_2^+ state to the ground state through a “virtual” 1_1^+ state at 300 keV, and the 2_2^+ state to the 2_1^+ state through a “virtual” 1_2^+ state at 700 keV.

From the χ^2_{min} values in Table 4.14, no significant difference in reproduction of the experimental data can be observed between solutions 1, 2 and 3. Using the GOSIA code, the relative population of the different excited states can be determined for each of these solutions. By default, GOSIA determines the population to a certain state at the average beam energy and scattering

Table 4.16: Relative importance of the three excitation paths in the population of the 2_2^+ state in ^{198}Po, determined using the GOSIA code. The two solutions correspond to solution 1 and solution 2 in Table 4.14. The relative population takes into account the integration over scattering angle and bombarding energy. The mentioned uncertainty is determined by folding in the experimental uncertainty on the matrix elements that are involved in the excitation process.

Solution	1-step excitation	2-step excitation	3-step excitation
Solution 1	22(9) %	75(9) %	3(2) %
Solution 2	21(8) %	79(8) %	0.0004(4) %

angle. These "point" populations were multiplied by the correction factor (see equation 2.24) to take into account the integration over scattering angle and bombarding energy. The results, which are shown in Table 4.15, help to further distinguish between the four solutions. The GOSIA code does not provide a way to determine the error bar on the calculated population numbers. The uncertainty on the relative population that is mentioned in Table 4.15, is determined by hand, folding in the relative error bar on the extracted matrix elements coupling to the respective state.

The negative sign for the loop $\langle 0_1^+||E2||2_1^+\rangle \times \langle 2_1^+||E2||2_2^+\rangle \times \langle 0_1^+||E2||2_2^+\rangle$ in solutions 3 and 4, gives a lower population of the 2_2^+ state, relative to the 2_1^+ state. In order to reproduce the experimentally observed yields, the diagonal matrix element of the 2_1^+ state has to be increased to large values, which exceed the rotational limit (1.3 eb for solutions 3 and 4) by far. Because of this unphysically large value for $\langle 2_1^+||E2||2_1^+\rangle$, these two solutions are disregarded.

Only the sign of the loop $\langle 2_1^+||E2||0_2^+\rangle \times \langle 0_2^+||E2||2_2^+\rangle \times \langle 2_2^+||E2||2_1^+\rangle$ is different when comparing solutions 1 and 2. Changing the sign of this loop does not change the population of any of the excited states significantly as can be seen in Table 4.15. However, a difference can be observed in the relative importance of the excitation paths in the population of the 2_2^+ state. This state can be populated through three different paths: in one step, $0_1^+ \rightarrow 2_2^+$, in two steps, $0_1^+ \rightarrow 2_1^+ \rightarrow 2_2^+$ or in three steps, $0_1^+ \rightarrow 2_1^+ \rightarrow 0_2^+ \rightarrow 2_2^+$.

The relative importance of the respective excitation path is again calculated using GOSIA, taking into account the integration over scattering angle and bombarding energy. The uncertainty on these numbers is determined manually, by folding in the relative uncertainty on the experimentally extracted matrix elements that are involved in the respective excitation paths. From the results in Table 4.16, it is apparent that two-step excitation is dominant in both solutions, while a difference can be observed in the relative importance of the three-step process which is negligible in solution 2. The matrix element $\langle 0_2^+||E2||2_2^+\rangle$ reaches the lower limit 0 in solution 2, hinting towards the fact that a better solution would be obtained with a negative sign for this matrix element. When the sign of $\langle 0_2^+||E2||2_2^+\rangle$ is allowed to change, the first solution is reproduced exactly in magnitude, but with a negative value for $\langle 2_1^+||E2||0_2^+\rangle$ and $\langle 0_2^+||E2||2_2^+\rangle$. However, the positive sign for the loop $\langle 2_1^+||E2||0_2^+\rangle \times \langle 0_2^+||E2||2_2^+\rangle \times \langle 2_2^+||E2||2_1^+\rangle$ is not changed. This is an argument to put solution 1 forward as the correct sign combination.

In the final step of the standard GOSIA/GOSIA2 approach, the matrix elements coupling the higher-lying excited states are fixed to the values determined in solution 1. Only $\langle 0_1^+||E2||2_1^+\rangle$ and $\langle 2_1^+||E2||2_1^+\rangle$ are free to vary in a χ^2-surface analysis using GOSIA2. The resulting 1σ contour is shown in Figure 4.14 and gives consistent results for $\langle 0_1^+||E2||2_1^+\rangle$ and $\langle 2_1^+||E2||2_1^+\rangle$ as obtained from the standard GOSIA analysis.

^{196}Po

Observed transitions and Coulomb-excitation cross sections Multi-step Coulomb excitation of ^{196}Po was observed, using a ^{104}Pd target, to populate the 2_1^+, 4_1^+, 0_2^+ and 2_2^+ states (see level scheme in Figure 4.29). Statistics acquired in the $2_1^+ \rightarrow 0_1^+$ and $4_1^+ \rightarrow 2_1^+$ transitions allowed for seven subdivisions. The observed total and divided statistics are summarized in Table 4.17, together with the extracted total cross section for Coulomb excitation to the 2_1^+, 4_1^+ and 2_2^+ state, based on equations 4.11, 4.12 and 4.13. The same method as in ^{198}Po was applied to disentangle the origin of the observed polonium X rays, giving rise to 76(70) X rays related to the $E0$ component of the $2_2^+ \rightarrow 2_1^+$ transition and an upper limit of 140 counts for the $E0$ transition from the 0_2^+ state to the ground state. The Coulomb-excitation cross section for the 2_2^+ state was determined twice, using two observed γ rays, depopulating the 2_2^+ state. Branching fractions were calculated using the intensities observed in the in-beam spectroscopy study of ^{196}Po by Bernstein et al. [24]. As in ^{198}Po, the $E2/M1$ mixing ratio δ was fixed to the value from literature for the $2_2^+ \rightarrow 2_1^+$ transition and the $E0$ component of the 2_2^+ decay was assumed to be negligible.

GOSIA analysis The data in Table 4.17 was combined with the relevant spectroscopic information on ^{196}Po shown in Table 4.8 to construct the input for the GOSIA analysis. Two solutions, resulting from the combined GOSIA and GOSIA2 approach, are presented in Table 4.18 with the total χ^2 value in the minimum. This value is calculated using the GOSIA output and the total number

Table 4.17: Statistics gathered in the Coulomb-excitation experiment of ^{196}Po on ^{104}Pd. θ_{lab} is the scattering angle in the laboratory frame of reference, N_γ represents the number of detected γ rays at the Miniball setup and σ_{CE} is the deduced cross section for Coulomb excitation in barn.

Nucleus	Transition	θ_{lab}	N_γ	σ_{CE} [b]
^{196}Po	$2_1^+ \to 0_1^+$	$26.1° - 57.1°$	$6.05(9) \times 10^3$	1.67(19)
		$26.1° - 32.6°$	$0.48(2) \times 10^3$	
		$32.7° - 38.3°$	$0.78(3) \times 10^3$	
		$38.4° - 43.3°$	$0.96(3) \times 10^3$	
		$43.3° - 47.5°$	$1.05(4) \times 10^3$	
		$47.6° - 51.2°$	$1.07(4) \times 10^3$	
		$51.2° - 54.4°$	$0.99(4) \times 10^3$	
		$54.4° - 57.1°$	$0.84(3) \times 10^3$	
	$4_1^+ \to 2_1^+$	$26.1° - 57.1°$	373(41)	0.108(17)
		$26.1° - 32.6°$	$0.15(11) \times 10^3$	
		$32.7° - 38.3°$	$0.45(13) \times 10^3$	
		$38.4° - 43.3°$	$0.25(14) \times 10^3$	
		$43.3° - 47.5°$	$0.67(15) \times 10^3$	
		$47.6° - 51.2°$	$0.67(14) \times 10^3$	
		$51.2° - 54.4°$	$0.52(14) \times 10^3$	
		$54.4° - 57.1°$	$0.43(14) \times 10^3$	
	$2_2^+ \to 0_1^+$	$26.1° - 57.1°$	79(12)	0.052(14)
	$2_2^+ \to 2_1^+$	$26.1° - 57.1°$	85(35)	0.06(3)
^{104}Pd	$2_1^+ \to 0_1^+$	$26.1° - 57.1°$	$5.17(8) \times 10^3$	
		$26.1° - 32.6°$	$0.47(2) \times 10^3$	
		$32.7° - 38.3°$	$0.62(3) \times 10^3$	
		$38.4° - 43.3°$	$0.85(3) \times 10^3$	
		$43.3° - 47.5°$	$0.90(3) \times 10^3$	
		$47.6° - 51.2°$	$0.86(3) \times 10^3$	
		$51.2° - 54.4°$	$0.78(3) \times 10^3$	
		$54.4° - 57.1°$	$0.63(3) \times 10^3$	

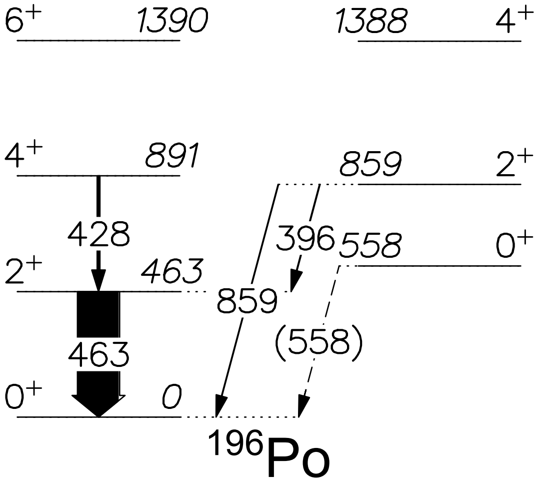

Figure 4.29: Level scheme of ^{196}Po, showing the levels that were included in the GOSIA analysis with their spin and parity and energy in keV. The observed transitions are illustrated with black arrows of which the width represents the intensity. The dashed line shows the $E0$ transition between the 0_2^+ state and the ground state.

of data points for the ^{196}Po projectile. A total of 26 data points is reached when summing the 18 γ-ray yields in Table 4.17, the 2 additional $E0$ yields depopulating the 0_2^+ and 2_2^+ states, the three life time values, the branching ratio and the $E2/M1$ mixing ratio mentioned in Table 4.8 and $\langle 0_1^+||E2||2_1^+\rangle$ resulting from the first-order solution using GOSIA2. The two solutions in Table 4.18 correspond to different sign combinations of the extracted matrix elements and show a small, and not significant, difference in χ^2_{min}.

The results in Table 4.18 do not mention any matrix elements related to the 0_2^+ state. The experimental data does not allow to extract information on these matrix elements. The only observed yield, related to the decay of the 0_2^+ state, is the $E0$ path to the ground state of which only an upper limit of 140 counts could be determined. Other possible γ-ray transitions related to the 0_2^+ state, $0_2^+ \rightarrow 2_1^+$ and $2_2^+ \rightarrow 0_2^+$ were unobserved in this study. As a consequence, this data set is only sensitive to the sign of one of the loops: $\langle 0_1^+||E2||2_1^+\rangle \times \langle 2_1^+||E2||2_2^+\rangle \times \langle 0_1^+||E2||2_2^+\rangle$ is positive for solution 1 and negative for solution 2 in Table 4.18.

Similar to the analysis of ^{198}Po, additional matrix elements were included in the GOSIA analysis for ^{196}Po. The experimental data set did not allow to extract

Table 4.18: Two sets of reduced transitional and diagonal $E2$ matrix elements coupling low-lying states in ^{196}Po, obtained in this work. The error bars represent 1σ. The different solutions correspond to different relative sign combinations of the matrix elements. χ^2_{min} represents the total χ^2 value in the minimum, taking into account the total number of data points.

$\langle \mathrm{I}_i \vert\vert E2 \vert\vert \mathrm{I}_f \rangle [eb]$	Solution 1	Solution 2
$\langle 0_1^+ \vert\vert E2 \vert\vert 2_1^+ \rangle$	1.32(5)	1.32(5)
$\langle 0_1^+ \vert\vert E2 \vert\vert 2_2^+ \rangle$	0.44(4)	−0.44(3)
$\langle 2_1^+ \vert\vert E2 \vert\vert 2_1^+ \rangle$	−0.2(4)	1.1(5)
$\langle 2_1^+ \vert\vert E2 \vert\vert 2_2^+ \rangle$	$2.12(^{16}_{22})$	$2.04(^{15}_{18})$
$\langle 2_1^+ \vert\vert E2 \vert\vert 4_1^+ \rangle$	2.68(11)	$2.69(^{12}_{11})$
χ^2_{min}	8.3	8.7

Table 4.19: Relative population of the low-lying excited states involved in the GOSIA analysis of ^{196}Po. The population is calculated for the two different solutions shown in Table 4.18 and takes into account the integration over scattering angle and bombarding energy. The uncertainty on the relative population is determined by folding in the experimental uncertainty on the matrix elements coupling to the respective state.

Populated state	Solution 1	Solution 2
2_1^+	90(2) %	91.0(11) %
0_2^+	2(2) %	1.1(11) %
2_2^+	2.9(3) %	2.7(3) %
4_1^+	5.1(3) %	5.2(4) %

Table 4.20: Relative importance of the three excitation paths in the population of the 2_2^+ state in ^{196}Po, determined using the GOSIA code. The two solutions correspond to solution 1 and solution 2 in Table 4.18. The relative population takes into account the integration over scattering angle and bombarding energy. The mentioned uncertainty is determined by folding in the experimental uncertainty on the matrix elements that are involved in the excitation process.

Solution	1-step excitation	2-step excitation	3-step excitation
Solution 1	54(3) %	46(3) %	0.000010(10) %
Solution 2	53(3) %	47(3) %	0.4(4) %

values for these matrix elements, but they were included to make sure that the additional correlations were taken into account in the GOSIA analysis. This means that the extracted uncertainties mentioned in Table 4.18 include possible variations for these additional matrix elements. The starting values for these extra matrix elements were determined as follows:

- $\langle 4_1^+||E2||6_1^+\rangle$: determined from the lifetime of the 6_1^+ state which is measured to be $\tau_{6_1^+} = 2.9(12)\,\text{ps}$ [47]
- $\langle 2_2^+||E2||4_2^+\rangle$: estimated from the rigid rotor model, applied to the non-yrast band, using $\langle 0_2^+||E2||2_2^+\rangle$
- $\langle 2_1^+||M1||2_2^+\rangle$: related to $\langle 2_1^+||E2||2_2^+\rangle$ through the $E2/M1$ mixing ratio δ
- $\langle 2_2^+||E2||2_2^+\rangle$: assumed to be zero.

In the final GOSIA analysis, these four matrix elements were free to vary in a physically reasonable range. The observed sensitivity was not sufficient to report values on them. Only the matrix element $\langle 4_1^+||E2||6_1^+\rangle$ could be determined but this value is the simple translation of the measured lifetime to the matrix element. Finally, "virtual" $M1$ matrix elements were added to take care of the $E0$ component of the decay of the 0_2^+ and 2_2^+ states [78]. These matrix elements couple the 0_2^+ state to the ground state through a "virtual" 1_1^+ state at 300 keV, and the 2_2^+ state to the 2_1^+ state through a "virtual" 1_2^+ state at 650 keV.

Changing the sign of the loop $\langle 0_1^+||E2||2_1^+\rangle \times \langle 2_1^+||E2||2_2^+\rangle \times \langle 0_1^+||E2||2_2^+\rangle$, affects the value of the diagonal matrix element $\langle 2_1^+||E2||2_1^+\rangle$ significantly. The two different solutions lead to a difference in the relative population of the 0_2^+ state (see Table 4.19), but as explained earlier, the present data set is not precise enough to distinguish between the two solutions. Finally, Table 4.20 shows that

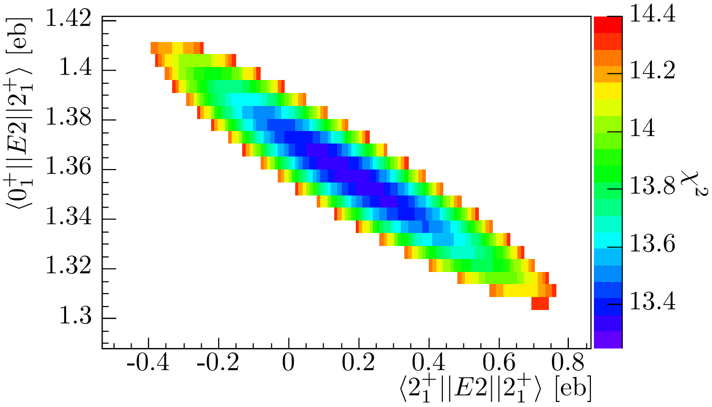

Figure 4.30: 1σ contour of the χ^2 surface in ^{196}Po, constructed by fixing the higher-order matrix elements according to solution 1 in Table 4.18. The 1σ contour represents all the points with $\chi^2_{\text{min}} \leq \chi^2 \leq \chi^2_{\text{min}} + 1$, where $\chi^2_{\text{min}} = 13.3$.

the relative importance of the excitation paths of the 2_2^+ state does not differ significantly between solutions 1 and 2. In this case, the one-step excitation, directly from the ground state to the 2_2^+ state, is dominant. The combination of all the information listed above, does not allow to distinguish between the two solutions shown in Table 4.18 in a model-independent way. Additional spectroscopic information or a more precise measurement of the $E0$ yields could help to solve this issue.

In the last step of the combined GOSIA/GOSIA2 approach, the matrix elements of the two adopted solutions are fixed in a new χ^2 analysis in GOSIA2 where only $\langle 0_1^+||E2||2_1^+\rangle$ and $\langle 2_1^+||E2||2_1^+\rangle$ are allowed to vary. The resulting total χ^2 plot is shown in Figure 4.30 for solution 1 and in Figure 4.31 for solution 2. The result from this GOSIA2 analysis is consistent with the values extracted from the standard GOSIA analysis: $\langle 0_1^+||E2||2_1^+\rangle = 1.36(5)$ eb, $\langle 2_1^+||E2||2_1^+\rangle = 0.2(6)$ eb for solution 1 and $\langle 0_1^+||E2||2_1^+\rangle = 1.36(5)$ eb, $\langle 2_1^+||E2||2_1^+\rangle = 1.4\binom{7}{6}$ eb for solution 2.

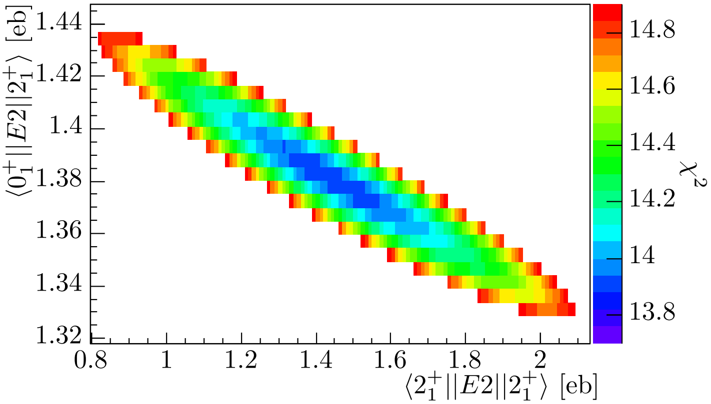

Figure 4.31: 1σ contour of the χ^2 surface in ^{196}Po, constructed by fixing the higher-order matrix elements according to solution 2 in Table 4.18. The 1σ contour represents all the points with $\chi^2_{\mathrm{min}} \leq \chi^2 \leq \chi^2_{\mathrm{min}} + 1$, where $\chi^2_{\mathrm{min}} = 13.9$.

5 | Discussion of the results

Coulomb excitation is a powerful technique as it allows extraction of electromagnetic matrix elements in a model-independent way. This chapter starts with an overview of the information that was obtained in this thesis. Three different nuclear models (i.e. the beyond-mean-field model (BMF), the interacting-boson model (IBM) and the general Bohr Hamiltonian model (GBH)) are used to compare the acquired results to. A short introduction to the basic physics that is contained in the different model descriptions is given in this chapter. The reader is referred to the references for more details. A comparison is made between model-independent observables, extracted from the data on the one hand and predicted by the theoretical nuclear models on the other. Next to that, a model-dependent value for the deformation parameter β_2 is extracted from the Coulomb-excitation results and compared to a deformation parameter derived from recent measurements of mean-square charge radii of the neutron-deficient polonium isotopes [79]. Finally, the phenomenological two-state mixing model is introduced and applied to the polonium isotopes and its predictions are confronted with the experimentally-deduced results.

5.1 Summary of the experimentally deduced $E2$ matrix elements

Table 5.1 lists the transitional $E2$ matrix elements that were extracted in this thesis using the technique of Coulomb excitation. From the matrix elements, the $B(E2)$ value in W.u. is deduced. The transition quadrupole moment $|Q_t|$, defined as

$$|Q_t(I_i \to I_f)| = \sqrt{\frac{16\pi}{5}} \frac{1}{\langle I_i 020 | I_f 0 \rangle} \frac{1}{\sqrt{2I_i + 1}} \langle I_f || E2 || I_i \rangle \tag{5.1}$$

Table 5.1: Summary of the results on transitional $E2$ matrix elements that were obtained in this thesis. I_i and I_f represent the initial and final spin of the transition with energy E_γ. The matrix element $\langle I_f||E2||I_i\rangle$ is translated to a $B(E2)$ value in W.u. and a transition quadrupole moment $|Q_t|$.

Isotope	I_i	I_f	E_γ [keV]	$\langle I_f\Vert E2\Vert I_i\rangle$ [eb]	$B(E2)$ [W.u.]	$\vert Q_t\vert$ [eb]
^{196}Po	2^+_1	0^+_1	463	1.32(5)	51(4)	4.19(16)
	2^+_2	0^+_1	859	0.44(4)	5.6(10)	1.40(13)
	2^+_2	2^+_1	396	$2.12(^{16}_{22})$	$1.3(^{2}_{3}) \times 10^2$	$5.6(^{4}_{6})$
	4^+_1	2^+_1	428	2.68(11)	116(10)	5.3(2)
^{198}Po	2^+_1	0^+_1	605	1.15(13)	39(9)	3.7(4)
	2^+_2	0^+_1	1039	$0.25(^{11}_{4})$	$1.8(^{16}_{10})$	$0.79(^{35}_{13})$
	2^+_2	2^+_1	434	2.8(9)	$2.3(15) \times 10^2$	7(2)
	4^+_1	2^+_1	554	$3.3(^{4}_{5})$	$1.8(^{4}_{5}) \times 10^2$	$6.5(^{8}_{10})$
	0^+_2	2^+_1	211	$1.4(^{24}_{7})$	$3(^{9}_{3}) \times 10^2$	$4(^{8}_{2})$
	2^+_2	0^+_2	223	1.2(8)	$4(6) \times 10^1$	4(3)
^{200}Po	2^+_1	0^+_1	666	1.03(3)	31(2)	3.27(10)
^{202}Po	2^+_1	0^+_1	671	$1.06(^{15}_{13})$	$33(^{9}_{8})$	$3.4(^{5}_{4})$

is also calculated from the transitional matrix elements. In this, $\langle I_i 020|I_f 0\rangle$ is a Clebsch-Gordan coefficient. In the case of ^{196}Po, where no model-independent distinction could be made between two solutions, solution 1 from Table 4.18 is chosen for the transitional $E2$ matrix elements as for these matrix elements no significant differences were observed.

The diagonal matrix element of the 2^+_1 state was also determined for all isotopes and is listed in Table 5.2, together with the deduced spectroscopic quadrupole moment. For ^{196}Po, two values are mentioned, related to the two solutions in Table 4.18.

5.2 Theoretical approaches

In general, two different approaches are possible in the description of the complex light-lead region where fingerprints of shape coexistence have been identified in multiple isotopes. The first is based on the spherical shell model and explains intruder states as proton excitations across the closed $Z = 82$ shell. The heavy open-shell nuclei in the light-lead region increase the dimensionality

Table 5.2: Summary of the results that were obtained in this thesis on diagonal $E2$ matrix elements. From the diagonal matrix element, the spectroscopic quadrupole moment Q_s is deduced.

Isotope	I	$\langle I\|\|E2\|\|I\rangle$ [eb]	Q_s [eb]
^{196}Po	2_1^+	$-0.2(4)$	$-0.2(3)$
		$1.0(5)$	$0.8(4)$
^{198}Po	2_1^+	$2.9(^{14}_{15})$	$2.2(11)$
^{200}Po	2_1^+	$0.1(2)$	$0.08(15)$
^{202}Po	2_1^+	$-0.7(^{13}_{12})$	$-0.5(^{10}_{9})$

of the corresponding shell-model space heavily. Therefore, the neutron-deficient polonium isotopes are studied in the algebraic framework of the interacting boson model (IBM) [80]. The alternative approach is based on mean-field methods and uses a description in terms of shapes and deformed shells. The beyond-mean-field approach (BMF) goes beyond the mean field to restore symmetries that were broken in the determination of a set of self-consistent mean-field wave functions [81–83]. The third nuclear model constructs a general Bohr Hamiltonian (GBH) by applying mean-field methods [84]. The resulting wave functions are parameterized by collective variables.

5.2.1 The interacting boson model (IBM)

The shell model considers the motion of independent nucleons, moving in a spherical mean field [3]. Closed shells at the magic numbers form the basis of this model, providing reference points for the calculations. m particle-n hole ($mp-nh$) excitations across closed shells and the residual proton-neutron interaction are crucial in the explanation of low-lying intruder structures. The large open neutron shell, spanning from $N = 82$ to $N = 126$, combined with the degrees of freedom of the two valence protons in the polonium isotopes and with the inclusion of $mp-nh$ excitations across the $Z = 82$ closed shell, present a problem that exceeds the current computational possibilities. Therefore, the model space is truncated in the interacting boson model by focusing on 0^+ and 2^+ coupled nucleon pairs which are treated as bosons [80, 85–87].

The interacting boson model with configuration mixing (IBM-CM in short) considers s and d bosons and mixes the boson configurations that correspond to different particle-hole excitations [88, 89]. Following the intruder spin symmetry [90, 91], no distinction is made between particle and hole bosons.

The drawback of the IBM model is the fact that experimental spectroscopic information is needed in order to determine the parameters of the Hamiltonian. The essential behavior of the parameters describing a general IBM Hamiltonian have been derived through a mapping from the nuclear shell model onto a boson space [92]. This makes it more difficult for the model to make predictions about unexplored regions of the nuclear chart.

The calculations for the neutron-deficient polonium isotopes involved the determination of 6 free parameters for the energies and 2 effective charges for the $E2$ transitions per isotope. The 8 free parameters per isotope were determined through a least-squares fit of the measured energies for the yrast band up to $I^\pi = 8^+$, the states 0_2^+, 2_2^+, 2_3^+, 2_4^+, 3_1^+, 4_2^+, 4_3^+, 5_1^+ and 6_2^+ and the measured $B(E2)$ values between the above states [93]. In this least-squares fit, the weight of the energy of the 2_1^+ state and the $B(E2; 2_1^+ \rightarrow 0_1^+)$ value is large compared to the other data points that get a more reduced weight, hereby effectively normalizing to the energy and transition probability of the 2_1^+ state.

5.2.2 The beyond-mean-field model (BMF)

The beyond-mean-field (BMF) calculations use Hartree-Fock + BCS theory and a Skyrme SLy4 effective interaction to determine a set of self-consistent mean-field wave functions. The Hartree-Fock energy is minimized with a constraint on the axial mass quadrupole moment which is used as collective variable. Broken symmetries are restored in a second step by projecting the mean-field states on angular momentum and on particle number. The basis states that are obtained this way, have good angular momentum, which allows to calculate the spectroscopic quadrupole moments and $B(E2)$ values directly. In a last step, the basis states are mixed in the framework of the generator coordinate method to extract collective wave functions [82, 83].

The BMF calculations performed for the polonium isotopes are limited to axially symmetric configurations and can predict values for a multitude of experimental observables like level energies, transition and spectroscopic quadrupole moments, monopole transition strengths, kinetic moments of inertia and mean-square charge radii [62]. The calculations do not need experimental information as input which makes the BMF model a robust method with a large predicting power. However, Yao et al. [62] state that there is an interpretation problem at small deformation values. In that case, the intrinsic deformation does not have a relation to an observable, making the interpretation of the energy curves less clear.

5.2.3 The general Bohr Hamiltonian model (GBH)

The general Bohr Hamiltonian model (GBH) uses the dynamical collective variables β_2 and γ to describe quadrupole excitations (see equation 1.7), without assuming anything a priori about the precise shape of the nucleus [84]. The general Bohr Hamiltonian is described by seven functions which are obtained from microscopic theory employing effective nucleon-nucleon interactions of the Skyrme SLy4 type. The mass parameters of a Bohr Hamiltonian are derived thanks to a cranking approximation to the adiabatic time-dependent Hartree-Fock method and are rescaled to take into account the fact that time-odd contributions to the mass parameters are neglected. One of the interests of this method is that it leads to calculations much less heavy than the BMF method and permits to treat triaxial quadrupole deformations [84, 94]. There is no need to fit to experimental data, the predictions are based solely on the knowledge of the effective nucleon-nucleon interactions as in the BMF approach.

5.3 Discussion

The aim of this thesis is to study the neutron-deficient $^{196-202}$Po isotopes. Tables 5.1 and 5.2 provide a summary of the experimental information that was extracted in this work. Three nuclear models, employing different methods to describe the polonium isotopes, were introduced.

5.3.1 Energy spectra

As mixing between co-existing structures is strongly influenced by the proximity of the energy levels of same spin, the comparison with theory starts with the energy levels. Figures 5.1 and 5.2 compare systematically both the level energies and transition quadrupole moments $|Q_t|$ for $^{196-202}$Po. The experimentally deduced values are compared to the calculations of the three theoretical nuclear models that were introduced in 5.2.

The BMF model overestimates the level energies in the four polonium isotopes studied here, as was noted before by Yao et al. [62]. The level energies in the neighboring mercury, lead and radon isotopes are also too widely spaced in the BMF calculations. The absence of the triaxial degree of freedom in the calculations can be one of the reasons for this discrepancy between the BMF approach and what is experimentally observed. Although the calculated energy of the 0^+_2 state is systematically too large in the GBH predictions (except for ^{202}Po where the experimental 0^+_2 state lies above the 2^+_2 state), the overall

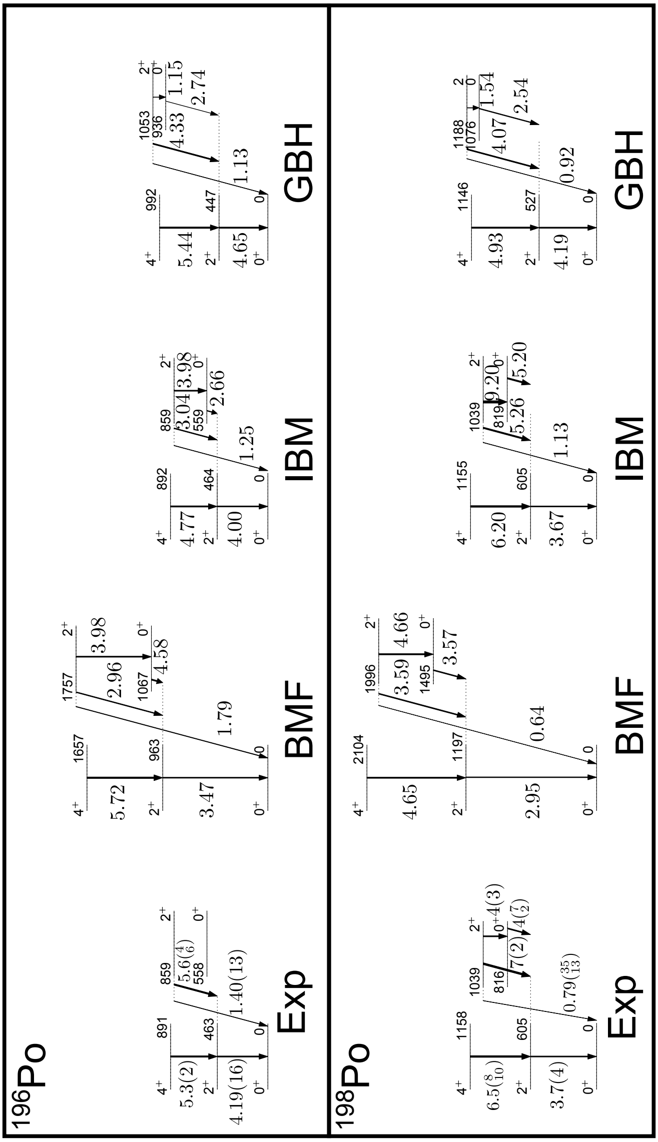

Figure 5.1: Experimental levels of the low-lying structures in ^{196,198}Po. The level energies are taken from Nuclear Data Sheets and are given in keV. Transitional $|Q_t|$ values are given in eb, based on the experimentally determined matrix elements. The width of the arrows represents the relative size of the transitional quadrupole moments $|Q_t|$. The experimental level energies and $|Q_t|$ values are compared to the same information, predicted by the BMF, IBM and GBH models.

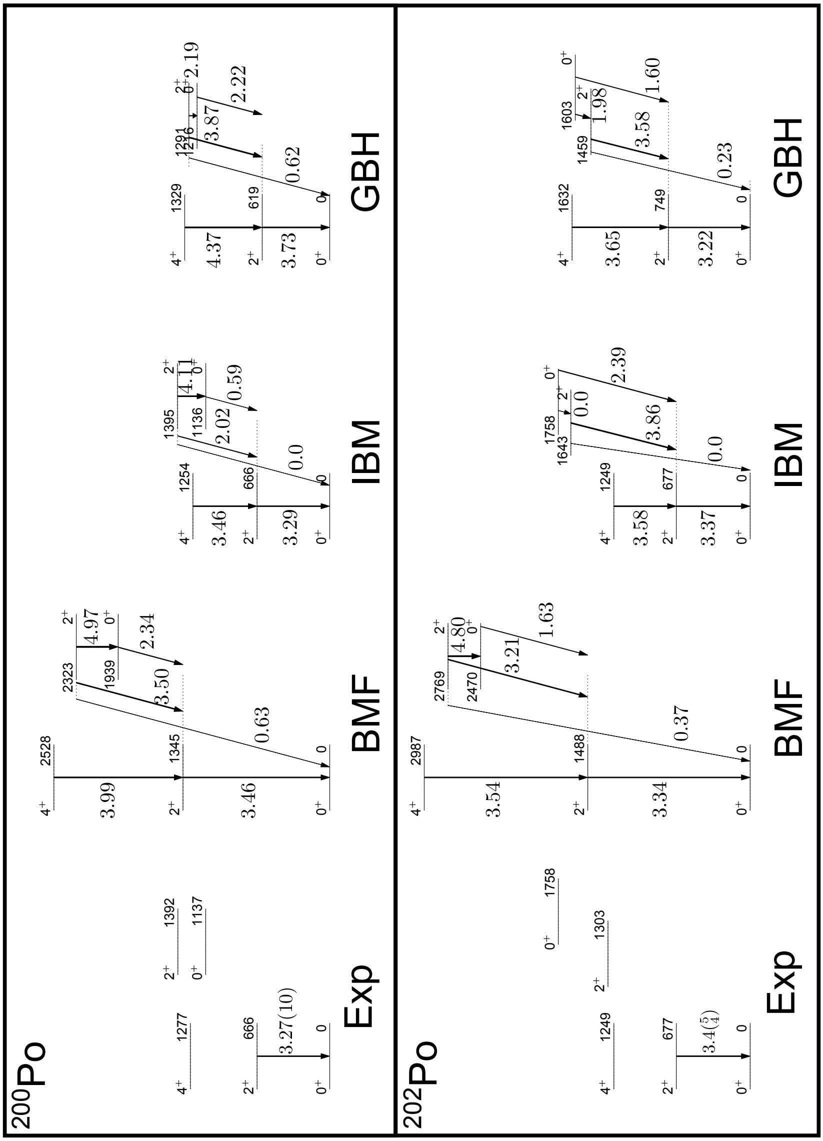

Figure 5.2: Experimental levels of the low-lying structures in ^{200,202}Po. The level energies are taken from Nuclear Data Sheets and are given in keV. Transitional $|Q_t|$ values are given in eb, based on the experimentally determined matrix elements. The width of the arrows represents the relative size of the transitional quadrupole moments $|Q_t|$. The experimental level energies and $|Q_t|$ values are compared to the same information, predicted by the BMF, IBM and GBH models.

agreement with the observed level energies is good. The results obtained using the GBH approach are significantly better then those from the BMF approach, pointing out the importance of triaxial quadrupole deformations. However, the renormalization of the GBH mass parameters does not allow a firm conclusion. The better agreement of the experimental level energies and the level energies calculated by the IBM model is a consequence of the fit that is performed in the IBM calculations, including the experimental level energies.

5.3.2 Electric quadrupole reduced transition probabilities

Despite the systematically too expanded level energies calculated by the BMF model, the transition probabilities between the ground state and 2_1^+ state are reproduced quite well for ^{200,202}Po, hinting towards a correct description of the underlying structures. Figure 5.3 shows a detailed comparison of the transition quadrupole moments, coupling the ground state to the two 2^+ states, extracted from the measured matrix elements on the one hand and predicted by theory on the other. For mass $A < 200$, the BMF $|Q_t(2_1^+ \rightarrow 0_1^+)|$ values underestimate the experimental values. The inclusion of the new data points, deduced in this thesis, shows that the three theoretical approaches reproduce the experimental values quite well.

The reproduction of the experimental $|Q_t(2_1^+ \rightarrow 0_1^+)|$ values by the IBM model follows from the fit that is performed to the measured $B(E2)$ values to fix the parameters of the IBM Hamiltonian. The experimental trend in $|Q_t(2_2^+ \rightarrow 0_1^+)|$ is predicted well by the IBM model, as well as the GBH model. The GBH model slightly overestimates the collectivity in the $2_1^+ \rightarrow 0_1^+$ transition for $^{196-200}$Po. Further, significant differences can be noted in the predictions of the three models for the transitions related to the 0_2^+ and 2_2^+ states (see Figures 5.1 and 5.2). The triaxial quadrupole degree of freedom included in the GBH approach does not affect significantly the transition probabilities. The current experimental accuracy does not allow to distinguish between the different model calculations.

A global view of the collectivity in the yrast band is shown in Figure 5.4, where the experimentally deduced reduced transition probabilities $B(E2; 2_1^+ \rightarrow 0_1^+)$ and $B(E2; 4_1^+ \rightarrow 2_1^+)$ are plotted, together with the predictions from the three models. The increase in collectivity, observed from the experimental $B(E2; 2_1^+ \rightarrow 0_1^+)$ values that are increasing with decreasing neutron number, is reproduced by the IBM and GBH model, but not by the BMF model as noted earlier. The BMF and GBH models predict an even steeper increase in collectivity for the $4_1^+ \rightarrow 2_1^+$ transition with decreasing mass number. The measured $B(E2; 4_1^+ \rightarrow 2_1^+)$ values in ^{194,196}Po are overestimated while the experimental

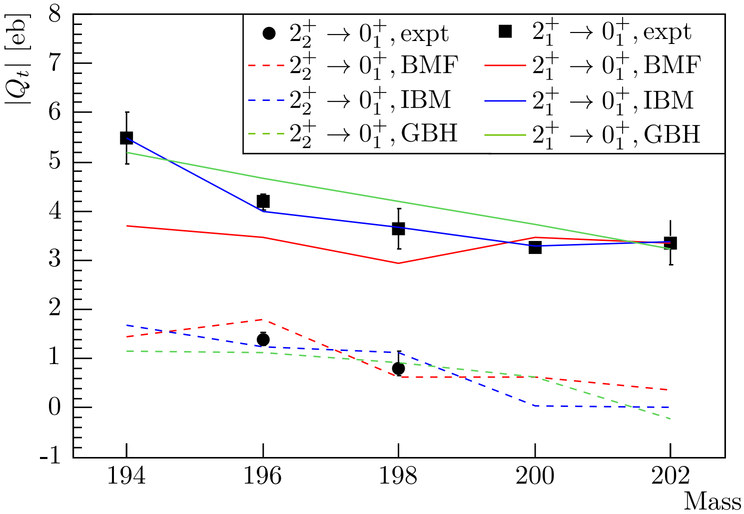

Figure 5.3: Experimental $|Q_t|$ values, extracted from the measured matrix elements $\langle 0_1^+||E2||2_1^+\rangle$ and $\langle 0_1^+||E2||2_2^+\rangle$ in the even-even polonium nuclei as a function of mass number. Data for $A = 194$ is taken from [46]. The experimental values are compared to the predictions from the three different theoretical model descriptions: the BMF, IBM and GBH model.

value for ^{198}Po significantly exceeds both model predictions. The kink in the experimentally deduced $B(E2; 4_1^+ \rightarrow 2_1^+)$ values, observed for mass $A = 198$, is reproduced and related to the fitting procedure in the IBM calculations. A linear behavior of the GBH $B(E2; 2_1^+ \rightarrow 0_1^+)$ and $B(E2; 4_1^+ \rightarrow 2_1^+)$ values as a function of mass number can be observed.

As explained in Chapter 1, the harmonic vibrator model and the rigid rotor model can predict ratios of $B(E2)$ values. Starting from the experimental $B(E2; 2_1^+ \rightarrow 0_1^+)$ values, the $B(E2; 4_1^+ \rightarrow 2_1^+)$ values are determined, assuming an harmonic vibrator and a rigid rotor model. These predictions are shown in Figure 5.5. The low-spin yrast band in ^{194}Po seems to behave like a rigid rotor while the harmonic vibrator behavior fits better to the observed values in ^{196}Po. It should be noted however that both models represent a very simplified picture of the complex physics that is at play in this region of the nuclear chart. Indeed, the low-lying 0_2^+ state that is observed in ^{196}Po does not fit in the picture of an harmonic vibrator. The large $B(E2; 4_1^+ \rightarrow 2_1^+)$ value in ^{198}Po is not well understood.

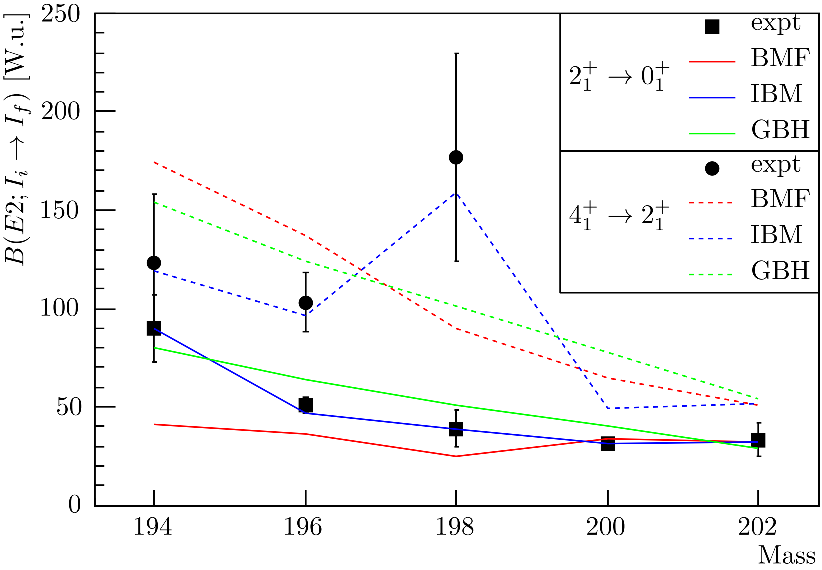

Figure 5.4: Experimental $B(E2; 2_1^+ \to 0_1^+)$ and $B(E2; 4_1^+ \to 2_1^+)$ values, expressed in W.u., compared to the predictions from the BMF, IBM and GBH models. The data for ^{194}Po is deduced from the results of lifetime measurements [46].

5.3.3 Spectroscopic quadrupole moment Q_s

The deformation of the 2_1^+ state can be understood in a Coulomb-excitation experiment through the measurement of the spectroscopic quadrupole moment Q_s. The observed trend of increasing deformation in the 2_1^+ state when going down in mass number, shown in Figure 5.6, is reproduced by the three model descriptions. Also plotted on Figure 5.6 are the predictions for Q_s, by applying the harmonic vibrator and rigid rotor model. The spectroscopic quadrupole moment of an harmonic vibrator vanishes, while the quadrupole moment of a rigid rotor is related to the $B(E2; 2_1^+ \to 0_1^+)$ value as shown.

As the sensitivity to the second-order effect in a Coulomb-excitation experiment is limited, the uncertainty on the experimental values for Q_s are large. Nevertheless, in ^{200}Po, a good precision is reached because of the large statistics that was acquired. One should keep in mind that the theoretical calculations also have an uncertainty. In the case of ^{196}Po, the two solutions for the spectroscopic quadrupole moment of the 2_1^+ state are significantly different. Solution 1 is compatible with harmonic vibrator behavior while solution 2 leans more towards

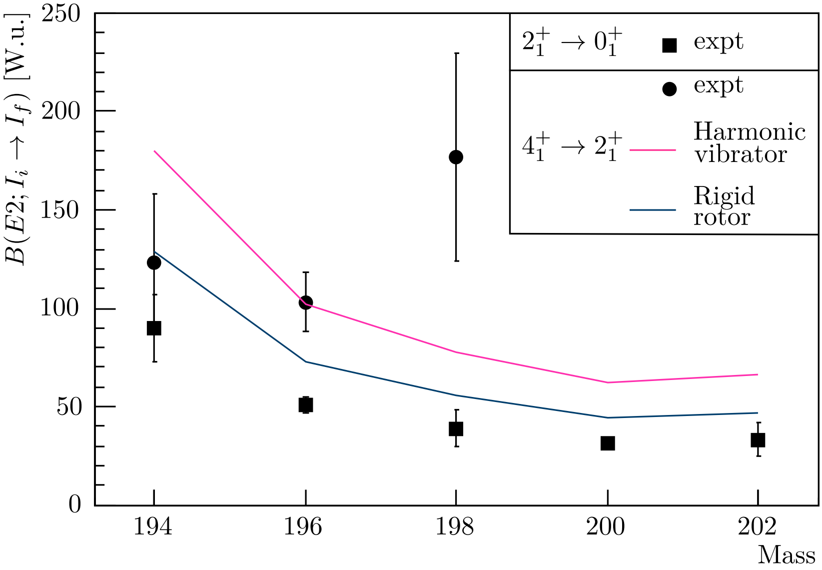

Figure 5.5: Experimental $B(E2; 2_1^+ \to 0_1^+)$ and $B(E2; 4_1^+ \to 2_1^+)$ values, expressed in W.u. The pink and dark blue lines show the $B(E2; 4_1^+ \to 2_1^+)$ value, extrapolated from the experimental $B(E2; 2_1^+ \to 0_1^+)$ value, applying the harmonic vibrator model and the rigid rotor model respectively.

the rigid rotor value. As explained before, there is no model-independent way to distinguish between these two solutions.

5.3.4 Nuclear quadrupole deformation in the Po nuclei

The examination of the observables in the previous sections allowed to extract information about the collectivity in the neutron-deficient polonium isotopes. In order to extract a deformation parameter, assumptions need to be made about the charge distribution of the nucleus which makes it a model-dependent observable. Figure 5.7 shows a comparison of extracted deformation parameters obtained from the measured charge radii $\delta\langle r^2 \rangle$ [95] on the one hand and from the sum of squared matrix elements $\sum_i |\langle 0_1^+ || E2 || 2_i^+ \rangle|^2$ on the other. As the parameters extracted from these two approaches are not identical, a separate notation is used. A deformation parameter, called $\tilde{\beta}_2$, was estimated from the

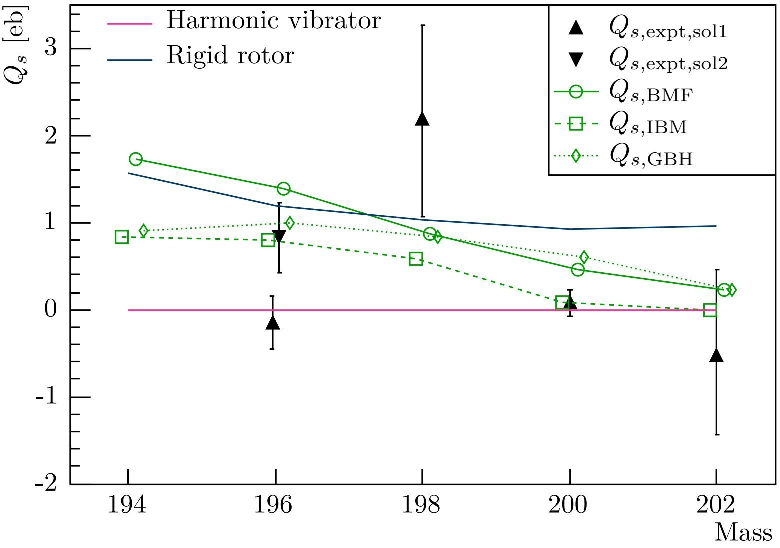

Figure 5.6: Experimentally determined values for the spectroscopic quadrupole moment Q_s of the 2_1^+ state as a function of the mass of the polonium isotope. In ^{196}Po no model-independent distinction could be made between two solutions for the matrix elements, yielding two different results of Q_s. Both results are shown here with a small offset from integer A for clarity. The experimental results are compared to the predictions from the BMF, IBM and GBH model. The pink and dark blue lines represent the prediction for Q_s, starting from the $B(E2; 2_1^+ \to 0_1^+)$ value and applying the harmonic vibrator and rigid rotor model respectively.

charge radii using the expression

$$\langle r^2\rangle_A \approx \langle r^2\rangle_A^{sph}\left(1+\frac{5}{4\pi}\tilde{\beta}_2^2\right), \tag{5.2}$$

where $\langle r^2\rangle_A^{sph}$ is the mean-square charge radius of a spherical nucleus with the same volume, which was evaluated with the finite range droplet model with a revised parametrization [79]. From the extracted $E2$ matrix elements, a deformation parameter β_2 can be deduced, through the quadrupole invariant $\langle Q^2\rangle$, using the expression

$$\sum_i |\langle 0_1^+||E2||2_i^+\rangle|^2 = \left(\frac{3}{4\pi}ZeR_0^2\right)^2 \beta_2^2 \tag{5.3}$$

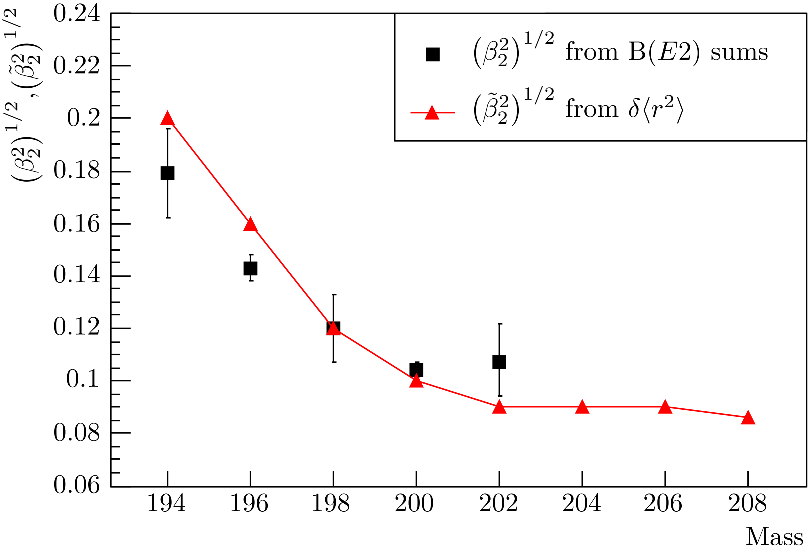

Figure 5.7: Deformation parameters of the ground state, extracted from the charge radii $\delta\langle r^2\rangle$ (triangles) [79] and sum of squared matrix elements according to equation 5.3 (squares). The data point for ^{194}Po is deduced from the lifetime measurement [46].

where a uniform charge distribution is assumed [65, 96, 97]. The sum of squared matrix elements $|\langle 0_1^+||E2||2_i^+\rangle|^2$ was evaluated over the 2^+ states that were populated for each case, i.e. only the 2_1^+ state in ^{200,202}Po and 2_1^+ and 2_2^+ states in ^{196,198}Po. In ^{194}Po, only the $B(E2)$ value to the 2_1^+ state is known from the lifetime measurement [46]. The onset of deviation from sphericity around $N = 112$ ($A = 196$), observed from the laser spectroscopy studies (see also Figure 4.1), is confirmed by the measured transition probabilities. An overall good agreement between the deformation parameters extracted from the charge radii and the squared matrix elements is observed.

5.4 Comparison to a two-state mixing model

In this section, a two-state mixing model is introduced. Previously, it was applied to the neutron-deficient $^{182-188}$Hg isotopes to test the assumption that these isotopes can be described by a spin-independent mixing between two rotational structures [98, 99]. A common set of matrix elements (transitional as well as diagonal) within the unperturbed bands was found to reproduce most of the experimental results. Hereby, the presence of two different structures that coexist at low excitation energy in the light even-mass mercury isotopes is established. A similar approach is used here to interpret the extracted matrix elements in the polonium isotopes.

The mixing probabilities for the mercury isotopes were derived from a fit of known level energies of deformed bands, built upon the first two 0^+ states, using the variable moment of inertia (VMI) model [100]. The polonium isotopes that are studied in this thesis, with neutron number $110 \leq N \leq 118$ are situated quite far from neutron mid-shell ($N = 104$). The presence of two rotational structures is much less pronounced in the polonium isotopes, compared to the mercury isotopes. Therefore, a deformed structure was assumed to mix with a spherical structure. Mixing amplitudes were determined, based on the size of the spin-independent mixing matrix element, which was determined from a fit with the VMI model of selected states in ^{196}Po.

5.4.1 Two-state mixing

As explained earlier, the many-body Schrödinger equation can be approximated by splitting the Hamiltonian in two parts, separating an independent-particle (shell-model) part (equation 1.2) from the residual interaction (equation 1.3). The ensuing eigenvalue equation, using as a basis the independent-particle many-body wave functions and using the Hamiltonian $H_0 + H_1$, can be solved by diagonalizing the Hamiltonian in the basis ϕ_i [3, 12]. The resulting wave functions will then be given by

$$\psi_k = \sum_i a_{ik} \phi_i \tag{5.4}$$

with the expansion coefficients a_{ik} for the kth state resulting from the diagonalization.

Two-state mixing theory

Suppose there are two states in a nucleus, both having the same spin I, that are described by the orthonormal wave functions ϕ_1 and ϕ_2 (see Figure 5.8). As an example, take the situation of $^{18}_{8}\mathrm{O}_{10}$ with two neutrons outside of the $^{16}_{8}\mathrm{O}_8$ closed shell. For a study of the 0^+ states, one can restrict the basis to the $(1d5/2)^2_{0^+}$ and $(2s1/2)^2_{0^+}$ states, called the basis states $\phi_1(0^+)$, $\phi_2(0^+)$ [3]. In general ϕ_1 and ϕ_2 are eigenfunctions of H_0 with respective eigenvalues $2\varepsilon_{1d5/2}$ and $2\varepsilon_{2s1/2}$. The matrix elements H_{11} and H_{22} are defined as $H_{11} = \langle\phi_1|H_0 + H_1|\phi_1\rangle$,

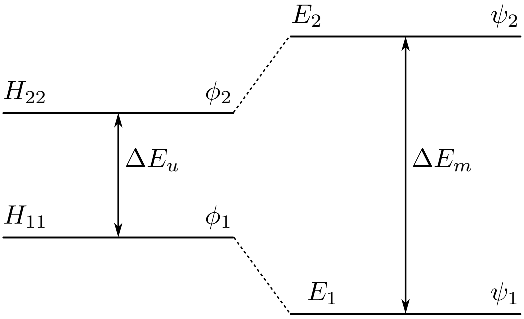

Figure 5.8: Two unperturbed states ϕ_1 and ϕ_2, with unperturbed (diagonal) energies H_{11} and H_{22} respectively, mix through a two-state mixing procedure. The wave functions of the resulting, mixed configurations are denoted with ψ_1 and ψ_2 and correspond to energies E_1 and E_2. ΔE_u represents the unperturbed energy separation while ΔE_m is the energy difference between the states, obtained after mixing.

$H_{22} = \langle \phi_2 | H_0 + H_1 | \phi_2 \rangle$. Linear combinations of these two wave functions describe the perturbed levels:

$$\begin{cases} \psi_1 = a_{11}\phi_1 + a_{21}\phi_2 \\ \psi_2 = a_{12}\phi_1 + a_{22}\phi_2 \end{cases} \tag{5.5}$$

which are normalized: $a_{1p}^2 + a_{2p}^2 = 1 (p = 1, 2)$. The coefficients a_{ij} can be interpreted as mixing amplitudes, expressing the relative contribution of the first and second unperturbed state to the mixed state. The energy eigenvalues can be obtained by solving the Schrödinger equation, which is described by the eigenvalue equation

$$\begin{pmatrix} H_{11} & V \\ V & H_{22} \end{pmatrix} \begin{pmatrix} a_{1p} \\ a_{2p} \end{pmatrix} = E_p \begin{pmatrix} a_{1p} \\ a_{2p} \end{pmatrix} \tag{5.6}$$

where the off-diagonal terms in the two-by-two matrix are equal and give the strength of the mixing interaction: $\langle \phi_1 | H_1 | \phi_2 \rangle = \langle \phi_2 | H_1 | \phi_1 \rangle = V$. Calculating the energy eigenvalues is equivalent to solving the secular equation

$$\begin{vmatrix} H_{11} - E_p & V \\ V & H_{22} - E_p \end{vmatrix} = 0 \tag{5.7}$$

with the solutions given by

$$E_p = \frac{H_{11} + H_{22} \pm \sqrt{(H_{11} - H_{22})^2 + 4V^2}}{2}. \tag{5.8}$$

Referring to Figure 5.8, E_1 corresponds to the solution with the minus sign while E_2 corresponds to the plus sign. The corresponding mixing amplitudes are obtained by combining equations 5.5 and 5.6:

$$\begin{cases} a_{11} = \frac{\pm V}{\sqrt{(E_1 - H_{11})^2 + V^2}} \\ a_{21} = \frac{\pm (E_1 - H_{11})}{\sqrt{(E_1 - H_{11})^2 + V^2}} \end{cases} \tag{5.9}$$

for the lowest-lying state ψ_1 and

$$\begin{cases} a_{22} = \frac{\pm V}{\sqrt{(E_2 - H_{22})^2 + V^2}} \\ a_{12} = \frac{\pm (E_2 - H_{22})}{\sqrt{(E_2 - H_{22})^2 + V^2}} \end{cases} \tag{5.10}$$

for ψ_2. One should note that during the rest of the discussion, V represents an attractive interaction, giving rise to a negative sign of V. This sign will not be written explicitly, but is contained in the symbol V. Rewriting equation 5.8 for $p = 1, 2$, leads to the conclusion that $E_2 - H_{22} = -(E_1 - H_{11})$. This implies the following relations:

$$\begin{cases} |a_{11}| = |a_{22}| = |\alpha| \\ |a_{12}| = |a_{21}| = |\beta| \end{cases} \tag{5.11}$$

where, again, $\alpha^2 + \beta^2 = 1$. Depending on the relative position of the unperturbed states, different conventions are applied for the signs of the mixing amplitudes α and β. Section 5.4.1 discusses this in more detail.

Inspection of the equations that were derived, leads to a few basic insights into two-state mixing. Equation 5.8 learns that mixing always pushes unperturbed levels apart: $\Delta E_m = \sqrt{(H_{11} - H_{22})^2 + 4V^2} \geq \Delta E_u$. The same equation also yields an upper limit for V: $|V| \leq \Delta E_m / 2$. Mixing is maximized when the unperturbed levels are degenerate, which leads to $E_{1,2} = E_0 \pm V$ (with $E_0 = H_{11} = H_{22}$) and equal mixing amplitudes $\alpha^2 = \beta^2 = 50\,\%$. Note that with a negative sign for V, related to an attractive interaction, E_1 corresponds to the positive sign ($E_1 = E_0 + V$) while E_2 corresponds to the negative sign.

Two-state mixing in the even-even polonium isotopes

In the even-even polonium isotopes, mixing is considered between two sets of 0^+ and 2^+ states. To facilitate the discussion, the following terminology will be used. The unperturbed states will be denoted with roman indices I and II, while the mixed, experimentally observed states will be represented by indices 1 and 2. Structure I will always refer to the “normal”, spherical structure.

The intruder structure, which is assumed to be deformed, will be marked as structure II. Mixing amplitude α will always be related to the component of the spherical structure in the lowest-lying state, while β represents the deformed amplitude in the lowest-lying state. This convention follows equations 5.11 and 5.5 exactly. Note that in the following, α_0, α_2, β_0 and β_2 are assumed to be positive values while previously they could also be negative. Depending on the relative position of the two structures, the convention for the signs of the mixing amplitudes is changed. Three different scenarios that occur in the even-even polonium isotopes that are studied in this thesis, are illustrated schematically in Figure 5.9. One should note that the relative position of the mixed states 0^+_1, 0^+_2, 2^+_1 and 2^+_2 depends on the unperturbed energy difference and on the size of the mixing matrix element V. A different ordering of the mixed states is thus perfectly possible, Figure 5.9 only serves to illustrate one of the possibilities.

In the default scenario, depicted in panel A of Figure 5.9, the spherical structure is lowest in energy, both for the 0^+ and 2^+ states. This means that $\alpha_0^2 > 50\,\%$ and $\alpha_2^2 > 50\,\%$. In this case, the convention introduced in [101] is used for the mixed wave functions of the 0^+ and 2^+ states:

$$\begin{cases} |0^+_1\rangle = \alpha_0|0^+_I\rangle + \beta_0|0^+_{II}\rangle \\ |0^+_2\rangle = \beta_0|0^+_I\rangle - \alpha_0|0^+_{II}\rangle \\ |2^+_1\rangle = \alpha_2|2^+_I\rangle + \beta_2|2^+_{II}\rangle \\ |2^+_2\rangle = \beta_2|2^+_I\rangle - \alpha_2|2^+_{II}\rangle. \end{cases} \tag{5.12}$$

Note that a different notation is used for the wave function of the states that are involved than in Figure 5.8. In stead of the notation using ϕ and ψ for the unperturbed and perturbed wave functions respectively, the name of the states, as introduced in Figure 5.9, is used to make the notation more explicit. In situation B) in Figure 5.9, the spherical 0^+ is lower in energy than the deformed 0^+ state: $\alpha_0^2 > 50\,\%$. However, the ordering is reversed for the 2^+ states: the deformed 2^+ state has intruded below the spherical one and thus $\alpha_2^2 < 50\,\%$. In that case, the default convention is applied for the wave functions of the mixed 0^+ states, but for the 2^+ states the convention is different:

$$\begin{cases} |0^+_1\rangle = \alpha_0|0^+_I\rangle + \beta_0|0^+_{II}\rangle \\ |0^+_2\rangle = \beta_0|0^+_I\rangle - \alpha_0|0^+_{II}\rangle \\ |2^+_1\rangle = \alpha_2|2^+_I\rangle + \beta_2|2^+_{II}\rangle \\ |2^+_2\rangle = -\beta_2|2^+_I\rangle + \alpha_2|2^+_{II}\rangle. \end{cases} \tag{5.13}$$

Finally, panel C of Figure 5.9 illustrates the scenario where both the deformed 0^+ and 2^+ states are lower in energy than their spherical partners, yielding $\alpha_0^2 < 50\,\%$, $\alpha_2^2 < 50\,\%$. In this case, the wave functions of the mixed states are

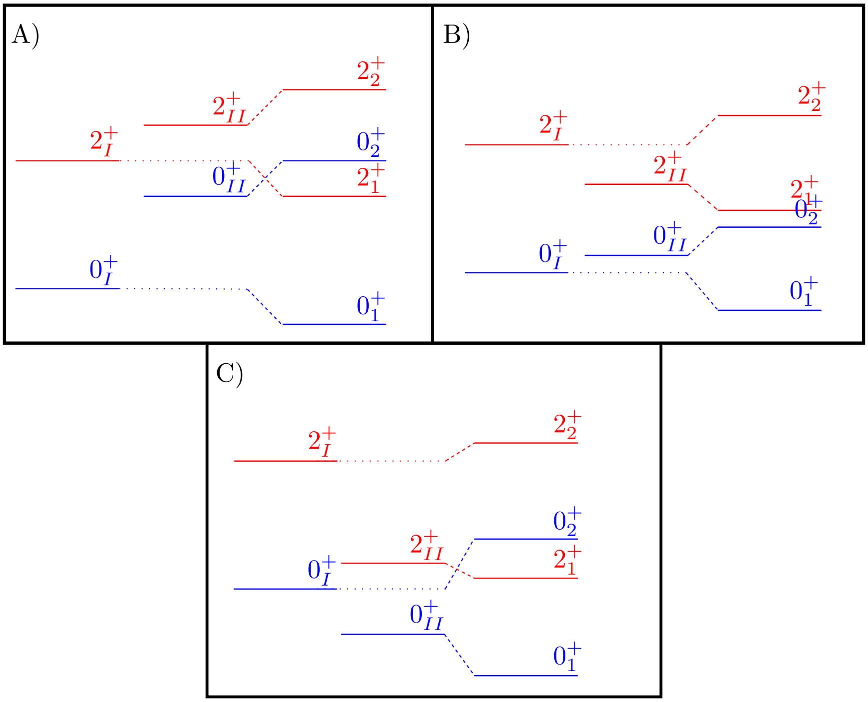

Figure 5.9: Three different mixing scenarios that occur in the even-even polonium isotopes that are studied in this thesis. The spherical structure is indicated by the roman index I, while the deformed states are shown with roman index II. 0^+ states are indicated in blue, 2^+ states are shown in red. The relative position of the mixed states (shown with indices 1 and 2) depends on the size of the mixing matrix element and on the unperturbed energy difference and can vary from what is shown here.

given by:

$$\begin{cases} |0_1^+\rangle = \alpha_0|0_I^+\rangle + \beta_0|0_{II}^+\rangle \\ |0_2^+\rangle = -\beta_0|0_I^+\rangle + \alpha_0|0_{II}^+\rangle \\ |2_1^+\rangle = \alpha_2|2_I^+\rangle + \beta_2|2_{II}^+\rangle \\ |2_2^+\rangle = -\beta_2|2_I^+\rangle + \alpha_2|2_{II}^+\rangle. \end{cases} \tag{5.14}$$

Matrix elements in the two-state mixing model

In section 5.4, the experimentally extracted matrix elements will be compared to the predictions of the phenomenological two-state mixing model. A final ingredient, necessary to perform this comparison, are the matrix elements, predicted by the two-state mixing model. Equations are given here for the default case of mixing, presented in panel A of Figure 5.9. The formulas, expressing the matrix elements in the two other scenarios are obtained analogously.

Transition probabilities between the mixed states, expressed by the reduced $E2$ matrix elements, are calculated, starting from the definition of the mixed wave functions in equation 5.12. In this, the reduced transition rates, expressing transitions between the two unperturbed structures, are assumed to vanish: $\langle 0_I^+||E2||2_{II}^+\rangle = \langle 2_I^+||E2||0_{II}^+\rangle = \langle 2_I^+||E2||2_{II}^+\rangle = 0$. Knowing this, the reduced matrix element between the yrast 0_1^+ and 2_1^+ states can be deduced:

$$\begin{aligned} \langle 0_1^+||E2||2_1^+\rangle &= \langle \alpha_0 0_I^+ + \beta_0 0_{II}^+||E2||\alpha_2 2_I^+ + \beta_2 2_{II}^+\rangle \\ &= \alpha_0\alpha_2\langle 0_I^+||E2||2_I^+\rangle + \alpha_0\beta_2\langle 0_I^+||E2||2_{II}^+\rangle \\ &+ \beta_0\alpha_2\langle 0_{II}^+||E2||2_I^+\rangle + \beta_0\beta_2\langle 0_{II}^+||E2||2_{II}^+\rangle \\ &= \alpha_0\alpha_2\langle 0_I^+||E2||2_I^+\rangle + \beta_0\beta_2\langle 0_{II}^+||E2||2_{II}^+\rangle. \end{aligned}$$

The other matrix elements are deduced in a similar way, yielding expressions for all possible transitions between mixed states:

$$\begin{aligned}
\langle 0_1^+||E2||2_2^+\rangle &= \alpha_0\beta_2\langle 0_I^+||E2||2_I^+\rangle - \alpha_2\beta_0\langle 0_{II}^+||E2||2_{II}^+\rangle \\
\langle 2_1^+||E2||0_2^+\rangle &= \alpha_2\beta_0\langle 0_I^+||E2||2_I^+\rangle - \alpha_0\beta_2\langle 0_{II}^+||E2||2_{II}^+\rangle \\
\langle 0_2^+||E2||2_2^+\rangle &= \beta_0\beta_2\langle 0_I^+||E2||2_I^+\rangle + \alpha_0\alpha_2\langle 0_{II}^+||E2||2_{II}^+\rangle \\
\langle 2_1^+||E2||2_2^+\rangle &= \alpha_2\beta_2\left[\langle 2_I^+||E2||2_I^+\rangle - \langle 2_{II}^+||E2||2_{II}^+\rangle\right] \\
\langle 2_1^+||E2||2_1^+\rangle &= \alpha_2^2\langle 2_I^+||E2||2_I^+\rangle + \beta_2^2\langle 2_{II}^+||E2||2_{II}^+\rangle \\
\langle 2_2^+||E2||2_2^+\rangle &= \beta_2^2\langle 2_I^+||E2||2_I^+\rangle + \alpha_2^2\langle 2_{II}^+||E2||2_{II}^+\rangle .
\end{aligned}$$

Interesting to note is the expression for the matrix element between the two 2^+ states, which reaches its maximal value for maximal mixing of the 2^+ states: $\alpha_2\beta_2 = 0.5$. However, it also depends on the difference between the diagonal matrix elements of the unperturbed 2^+ states, which expresses the difference in deformation of the two structures. Two structures, mixing maximally but having the same deformation (both prolate, both oblate, or both spherical), will thus show a vanishing $\langle 2_1^+||E2||2_2^+\rangle$ matrix element.

5.4.2 The variable moment of inertia model (VMI) applied to the neutron-deficient polonium isotopes

In Figure 5.10 the kinematic moments of inertia, $J^{(1)}$, are plotted as a function of the γ-ray transition energy for the even-even $^{190-196}$Po isotopes. The same is shown for ^{188}Pb and ^{186}Hg as comparison. The kinematic moments of inertia are extracted for each $I \rightarrow I-2$ transition in the yrast band, based on the rotational model (see 1.2.3):

$$J^{(1)} = \frac{\hbar^2}{2\Delta E}\left[(I+2)(I+3) - I(I+1)\right]. \tag{5.15}$$

A smoothly increasing trend of $J^{(1)}$ with respect to the transition energy is the typical behavior for a soft rotor nucleus. These nuclei can be described within the variable moment of inertia (VMI) model [100]. This two-parameter model starts from the rotational model, but allows the moment of inertia of the nucleus to vary across the band. Each nucleus is characterized by (J_0, σ), with J_0 the moment of inertia of the ground state and σ a "softness parameter", which is 0 for a rigid rotor and increases with increasing deviation from the rigid-rotor model.

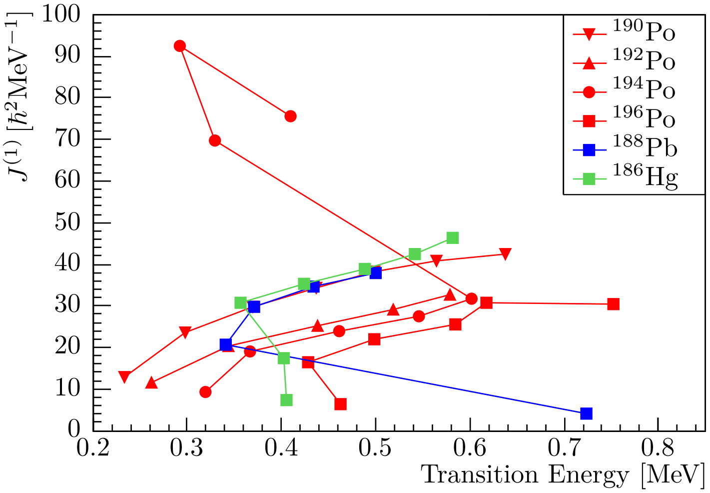

Figure 5.10: Kinematic moments of inertia $J^{(1)}$ as a function of the transition energy in MeV for the yrast states of the even-even $^{190-196}$Po isotopes, compared to those for ^{188}Pb and ^{186}Hg (see also ref. [33]).

The observed pattern for the yrast band in ^{190}Po is very similar to that observed in ^{188}Pb and ^{186}Hg, where a prolate-deformed intruder band is yrast from 6^+ onwards. ^{192}Po also shows smoothly increasing moments of inertia as a function of transition energy, albeit with a smaller magnitude of $J^{(1)}$. Although a similar behavior is observed for ^{194}Po, the trend is clearly distorted for high spins ($I > 10^+$) and also starts to deviate for the low-spin $2^+ \rightarrow 0^+$ transition. At mass $A = 196$, the observed trend shows that a soft-rotor character alone is not enough to describe the yrast band in ^{196}Po. From Figure 5.10, mixing is expected between a rotational structure, which is yrast at higher spins, and a second structure for ^{194,196}Po.

The VMI model was applied to the deformed structure in the neutron-deficient polonium isotopes. The level energy in the VMI model is given by

$$E_I(J) = E_0 + \frac{C}{2}\left(J_I - J_0\right)^2 + \frac{I(I+1)}{2J_I} \qquad (5.16)$$

where C is the "restoring force constant" which is related to the softness parameter, J_0 is the moment of inertia of the ground state and J_I is the moment of inertia of the state with angular momentum I. E_0 is the energy of the 0^+

Table 5.3: Results of the fit of the level energies of the deformed band in $^{190-196}$Po, using the VMI model. The three fit parameters are given with their associated 1σ uncertainty, taking into account correlations between the fit parameters.

Isotope	E_0 [keV]	J_0 [$\hbar^2$/keV]	C [$\times 10^6 \hbar^6$keV^3]
^{190}Po	88.8(16)	0.01780(17)	1.541(18)
^{192}Po	75.3(10)	0.01369(11)	2.17(2)
^{194}Po	128(3)	0.0127(2)	2.44(3)
^{196}Po	309.7(7)	0.01236(4)	3.215(9)

band head of the rotational band. The equilibrium condition

$$\frac{\partial E(J)}{\partial J} = 0 \tag{5.17}$$

determines the moment of inertia for each state with spin I. Combining equations 5.16 and 5.17, yields a cubic equation:

$$J_I^3 - J_I^2 J_0 - \frac{I(I+1)}{2C} = 0 \tag{5.18}$$

which has one real root for any finite positive value of J_I and C and can be solved algebraically. Equation 5.18, together with equation 5.16, gives an expression for the energy of the levels in the deformed band, as a function of the ground-state moment of inertia J_0 and parameter C:

$$E_I = E_0 + \frac{I(I+1)}{2J_I}\left(1 + \frac{I(I+1)}{4CJ_I^3}\right). \tag{5.19}$$

Equations 5.18 and 5.19 were used to fit the known level energies of the yrast band in ^{190,192}Po. The energy of the 0^+ ground state was not included in the fit as this state might be mixed. States up to and including 14^+ were included for ^{190}Po, and 10^+ for ^{192}Po. A good fit is obtained, pointing to the fact that the yrast states from 2^+ onwards belong to a soft rotational band. The resulting energy-versus-spin curve is shown for both isotopes in Figure 5.11, while the fit parameters are given in Table 5.3. As was already apparent from Figure 5.10, the resulting moment of inertia of the ground state, J_0, is larger for ^{190}Po than for ^{192}Po.

The same procedure was applied to fit the yrast 4^+, 6^+, 8^+ and 10^+ levels in ^{194}Po. Panel A of Figure 5.12 shows the result, together with the other

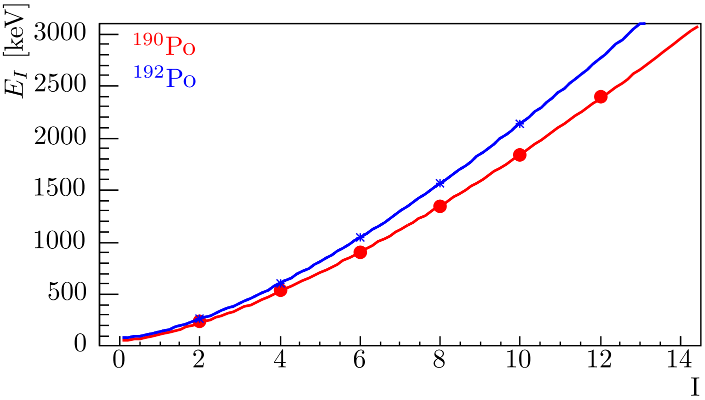

Figure 5.11: Fit of known level energies of the yrast band as a function of spin I in ^{190,192}Po, using the variable moment of inertia model. The states that were included in the fit are illustrated with red circles and blue crosses for ^{190}Po and ^{192}Po respectively. The fit result is depicted with a solid line in the same color.

observed low-lying states that were not included in the fit. In ^{196}Po, the 4^+, 6^+, 8^+ and 12^+ levels were included in the fit with the VMI model. Two states with spin and parity 10^+ are observed to lie very close to each other. Because of this ambiguity, none of these states was taken into account for the fit. The resulting energy-versus-spin curve for ^{196}Po is shown in panel B of Figure 5.12, while the fit parameters for both ^{194,196}Po are listed in Table 5.3. As the extracted fit parameters do not vary drastically between the two isotopes, the characteristics of the deformed structure in ^{194,196}Po are found to be similar. To confirm this, a VMI fit was performed to the same states in both isotopes, but fixing the parameters J_0 and C to the mean values ($J_0 = 0.0125\,\hbar^2/\text{keV}$, $C = 2.828 \times 10^6\,\hbar^6\text{keV}^3$). The level energies could be reproduced in both cases, resulting in changed values for the 0^+ band head energy ($E_0 = 44.60(10)$ keV in ^{194}Po, $E_0 = 329.42(8)$ keV in ^{196}Po).

Multiple states of same angular momentum are observed to lie close in energy in these two isotopes, suggesting possible mixing of structures. However, a rotational sequence with the same characteristics could be identified in both isotopes. Assuming that the fitted states in ^{194,196}Po are pure, an extrapolation of the deformed structure can be performed to estimate the unmixed 0^+ and 2^+ rotational level energies.

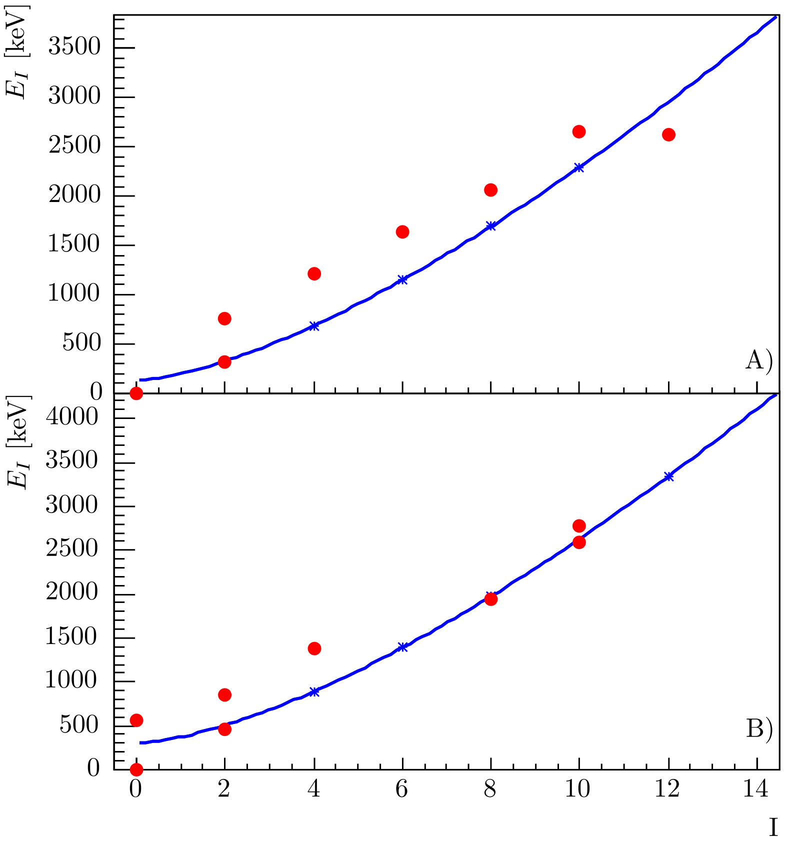

Figure 5.12: A) Fit of 4^+, 6^+, 8^+ and 10^+ yrast level energies as a function of spin I in ^{194}Po, using the variable moment of inertia model. B) Fit of 4^+, 6^+, 8^+ and 12^+ level energies as a function of spin I in ^{196}Po, using the variable moment of inertia model. The states that were included in the fit are illustrated with blue crosses. Other observed states, that were not included in the fit, are shown with red circles.

5.4.3 Application to the Po isotopes

Two-state mixing theory, introduced in section 5.4.1, is applied to $^{194-202}$Po. Results from the VMI fit of selected level energies in ^{196}Po are used to estimate the size of the mixing matrix element, which is assumed to be spin independent and constant throughout the five isotopes that are studied. A deformed structure is assumed to mix with a "normal", spherical, structure. With these assumptions, a common set of unmixed matrix elements is fitted to the experimentally known matrix elements for these isotopes.

Determination of mixing amplitudes

The extrapolated values for the 0^+ and 2^+ level energies of the deformed structure, determined in section 5.4.2, can be combined with the observed, mixed, level energies 0^+_1, 0^+_2, 2^+_1 and 2^+_2 in ^{196}Po to extract the size of the mixing matrix element and mixing amplitudes. Within a two-level model, the energy splitting is symmetric, making it possible to estimate the unperturbed energy of the spherical structure. Figure 5.13 shows a schematic picture of the situation in ^{196}Po, together with the extracted mixing matrix element and the square of the wave-function mixing amplitude. In the two-level model, on one side we have a basis state corresponding to a deformed rotor (see VMI, section 5.4.2), whereas on the other side we consider a basis state which originates from the structure of the 0^+_1 and 2^+_1 states, as observed in the heavier polonium nuclei ($A \geq 198$), which we call "spherical" for the remaining discussion.

While the experimentally observed 0^+_1 state in ^{196}Po has the largest contribution from the spherical structure (see Figure 5.13), the wave function of the 2^+_1 state consists mainly of the deformed structure. This behavior is also apparent from the square of the wave-function mixing amplitude, being larger than 50 % for the 0^+ states, but smaller than 50 % for the 2^+ states. This corresponds to situation B) in Figure 5.9. Since the excited 0^+ state has not been observed in ^{194}Po, it is not possible to repeat this procedure in the lighter isotope.

The size of the mixing matrix elements extracted in ^{196}Po is used as guideline for the mixing in the other isotopes that are studied. Starting from a spin-independent, fixed mixing matrix element V and using the perturbed (experimentally observed) level energies, the unperturbed level energies and mixing amplitudes can be deduced for all isotopes. Consider the mixing between the 0^+ states, depicted schematically in Figure 5.14. The situation for 2^+ mixing is completely equivalent. Following the two-level model, introduced in

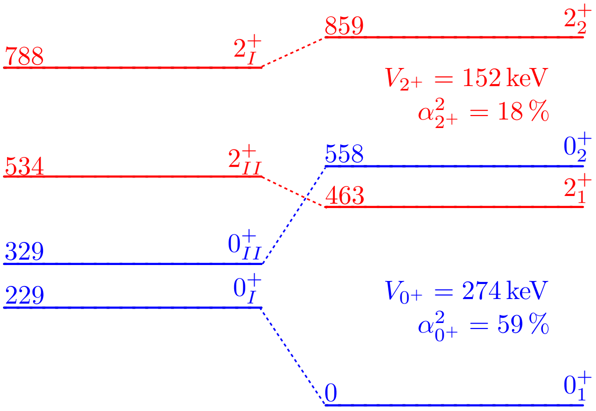

Figure 5.13: Unperturbed states 0^+_I, 0^+_{II}, 2^+_I and 2^+_{II} and level energies on the left, perturbed states 0^+_1, 0^+_2, 2^+_1 and 2^+_2 and level energies on the right, in the case of ^{196}Po. The mixing of the 0^+ states is illustrated in blue, that of the 2^+ states in red. Unmixed states with subscript I belong to the spherical configuration, while states with subscript II are members of the deformed structure. The extracted mixing matrix element and square of the wave-function mixing amplitude of the spherical configuration are also shown.

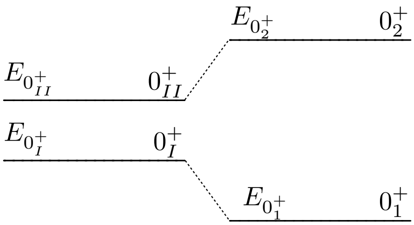

Figure 5.14: Schematic picture of the mixing of the unperturbed 0^+_I and 0^+_{II} states with energies $E_{0^+_I}$ and $E_{0^+_{II}}$, with as a result the mixed states 0^+_1 and 0^+_2 with respective energies $E_{0^+_1}$ and $E_{0^+_2}$.

section 5.4.1, one derives the following relations:

$$\begin{cases} \left|E_{0_2^+} - E_{0_{II}^+}\right| = \left|E_{0_I^+} - E_{0_1^+}\right| \\ \left(E_{0_{II}^+} - E_{0_I^+}\right)^2 = \left(E_{0_2^+} - E_{0_1^+}\right)^2 - 4V^2. \end{cases} \tag{5.20}$$

Considering the polonium isotopes studied, this set of equations contains two unknowns: $E_{0_I^+}$ and $E_{0_{II}^+}$, which can be determined analytically:

$$\begin{cases} E_{0_I^+} = \frac{\mp\sqrt{E^2_{0_1^+} - 2E_{0_1^+}E_{0_2^+} + E^2_{0_2^+} - 4V^2} + E_{0_1^+} + E_{0_2^+}}{2} \\ E_{0_{II}^+} = \frac{\pm\sqrt{E^2_{0_1^+} - 2E_{0_1^+}E_{0_2^+} + E^2_{0_2^+} - 4V^2} + E_{0_1^+} + E_{0_2^+}}{2}. \end{cases} \tag{5.21}$$

From this, the mixing amplitude of the spherical configuration can be extracted:

$$\alpha_{0^+} = \frac{-V}{\sqrt{\left(E_{0_1^+} - E_{0_I^+}\right)^2 + V^2}}. \tag{5.22}$$

The situation in ^{194}Po is slightly different, as $E_{0_2^+}$ is unknown. In this case, $E_{0_{II}^+}$ is determined using the VMI fit and from this, $E_{0_I^+}$ and $E_{0_2^+}$ are determined:

$$\begin{cases} E_{0_2^+} = \frac{E^2_{0_{II}^+} - E_{0_{II}^+}E_{0_1^+} + V^2}{E_{0_{II}^+} - E_{0_1^+}} \\ E_{0_I^+} = \frac{E_{0_{II}^+}E_{0_1^+} - E^2_{0_1^+} + V^2}{E_{0_{II}^+} - E_{0_1^+}}. \end{cases} \tag{5.23}$$

Equations 5.21, 5.22 and 5.23 are applied for all isotopes, for three different values of the mixing matrix element V. The size of the mixing matrix element is based on the extracted mixing matrix elements in ^{196}Po and is taken to be equal to $150, 200$ and $270\,\mathrm{keV}$. Figure 5.15 shows the deduced unperturbed 0^+ and 2^+ level energies in $^{194-202}$Po. The influence of the size of V on the unmixed 0^+ level energies is negligible in the three heaviest isotopes, while in ^{194,196}Po, the position of the unperturbed states is very sensitive to V. The relative position of the two structures is based on the VMI fit of the yrast states at higher spin (Figure 5.12). The deformed structure is assumed to be lowest in energy for $A \leq 194$ for the 0^+ states and for $A \leq 196$ for the 2^+ states. Finally, a large mixing matrix element $V = 270\,\mathrm{keV}$ for the 2^+ mixing, is only possible in the two heaviest isotopes. In the other isotopes, maximal mixing is already reached at $V < 270\,\mathrm{keV}$. The corresponding mixing amplitudes are illustrated in Figure 5.16.

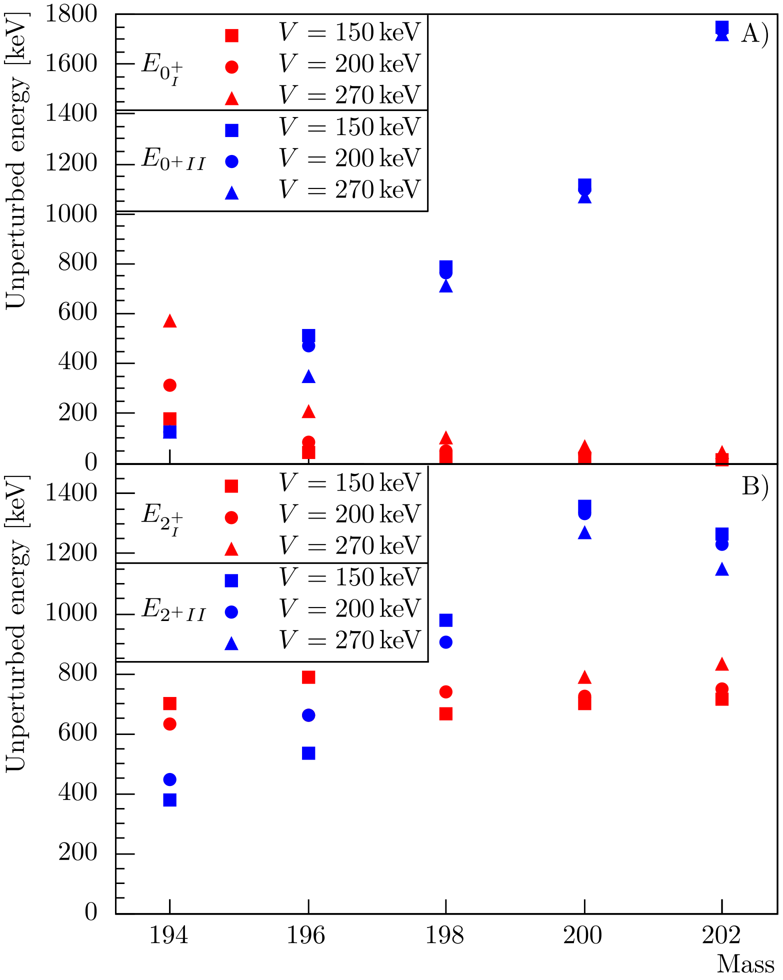

Figure 5.15: A) Unperturbed 0^+ level energies of the spherical ($E_{0^+_I}$, in red) and deformed ($E_{0^+_{II}}$, in blue) structure in $^{194-202}$Po. The unperturbed 0^+_{II} energy in ^{194}Po does not vary with V, as it is fixed to the extrapolated value from the VMI fit. B) Unperturbed 2^+ level energies of the spherical ($E_{2^+_I}$, in red) and deformed ($E_{2^+_{II}}$, in blue) structure in $^{194-202}$Po. For a mixing matrix element $V = 200\,\text{keV}$, the 2^+_I and 2^+_{II} level energies in ^{196}Po are degenerate, corresponding to maximal (50 %) mixing. The level energies are calculated for three different values of the mixing matrix element V.

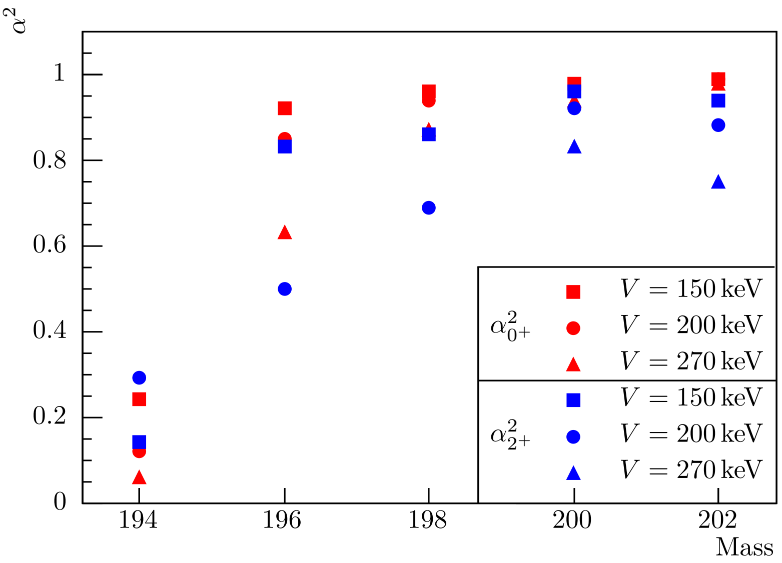

Figure 5.16: Square of wave-function mixing amplitudes for the spherical configuration in $^{194-202}$Po, for three different values of the mixing matrix element V. The mixing amplitudes of the 0^+ state are depicted in red, for the 2^+ state in blue.

A large mixing matrix element $V = 270\,\mathrm{keV}$ is not possible for the 2^+ mixing in ^{194,196,198}Po. In order to have a spin-independent value of the mixing matrix element, $V = 270\,\mathrm{keV}$ has to be excluded. The two other possibilities ($V = 150\,\mathrm{keV}$ and $V = 200\,\mathrm{keV}$) were used, in a next step, to try to reproduce the experimentally observed matrix elements. A common set of unmixed matrix elements was fitted to the experimental matrix elements, calculated following the expressions that were derived in section 5.4.1. The best reproduction was observed at $V = 200\,\mathrm{keV}$, with a total χ^2 of 101, compared to $\chi^2 = 196$ when $V = 150\,\mathrm{keV}$. The resulting mixing amplitudes are shown in Table 5.4.

Results

Starting from the wave-function mixing amplitudes in Table 5.4, a common set of unmixed matrix elements for the five isotopes is fitted to the experimentally observed matrix elements. The level of reproduction is based on the calculated

Table 5.4: Square of wave-function mixing amplitudes of the spherical configuration, at spin 0^+ (α^2_{0+}) and spin 2^+ (α^2_{2+}). The mixing matrix element V is taken to be 200 keV.

Isotope	α^2_{0+}	α^2_{2+}
^{194}Po	12 %	29 %
^{196}Po	85 %	50 %
^{198}Po	94 %	69 %
^{200}Po	97 %	92 %
^{202}Po	99 %	88 %

total χ^2 value, which is defined as

$$\chi^2 = \sum_i \frac{(\mathrm{ME}_{\mathrm{calc},i} - \mathrm{ME}_{\mathrm{exp},i})^2}{\sigma_i^2} \tag{5.24}$$

where $\mathrm{ME}_{\mathrm{calc},i}$ is the calculated matrix element using the two-level mixing model (see section 5.4.1), $\mathrm{ME}_{\mathrm{exp},i}$ is the experimental value of the same matrix element and σ_i is its associated 1σ uncertainty. The sum runs over all the experimentally observed matrix elements for $^{194-202}$Po. For ^{194}Po, the measured value of the lifetime of the 2^+_1 state is used to calculate the $E2$ matrix element between the ground state and the 2^+_1 state, $\langle 0^+_1||E2||2^+_1\rangle = 1.73(16)$ eb [46]. In the fitting procedure the unperturbed diagonal matrix elements were not allowed to cross the rotational limit compared to the intraband transitional matrix element ($|\langle 2^+||E2||2^+\rangle| < 1.195 \times \langle 0^+||E2||2^+\rangle$ (see section 1.2.3).

The result, which is shown in Figure 5.17, corresponds to a common set of unmixed matrix elements for $^{194-202}$Po:

$$\begin{cases} \langle 0^+_I||E2||2^+_I\rangle = 1.1\,\mathrm{eb} \\ \langle 0^+_{II}||E2||2^+_{II}\rangle = 1.5\,\mathrm{eb} \\ \langle 2^+_I||E2||2^+_I\rangle = -0.4\,\mathrm{eb} \\ \langle 2^+_{II}||E2||2^+_{II}\rangle = 1.8\,\mathrm{eb}. \end{cases} \tag{5.25}$$

The best fit was found with solution 2 in ^{196}Po (see Table 4.18) where the diagonal matrix element is positive and $\langle 0^+_1||E2||2^+_2\rangle$ is negative. Note that this solution is also favored by the three theoretical approaches as shown in Figure 5.6. Most of the experimental results are reproduced within 1σ uncertainty. The total χ^2 for this fit is equal to 101, while the total χ^2 for the best fit to solution 1 is equal to 189. The extracted unperturbed $E2$ matrix elements

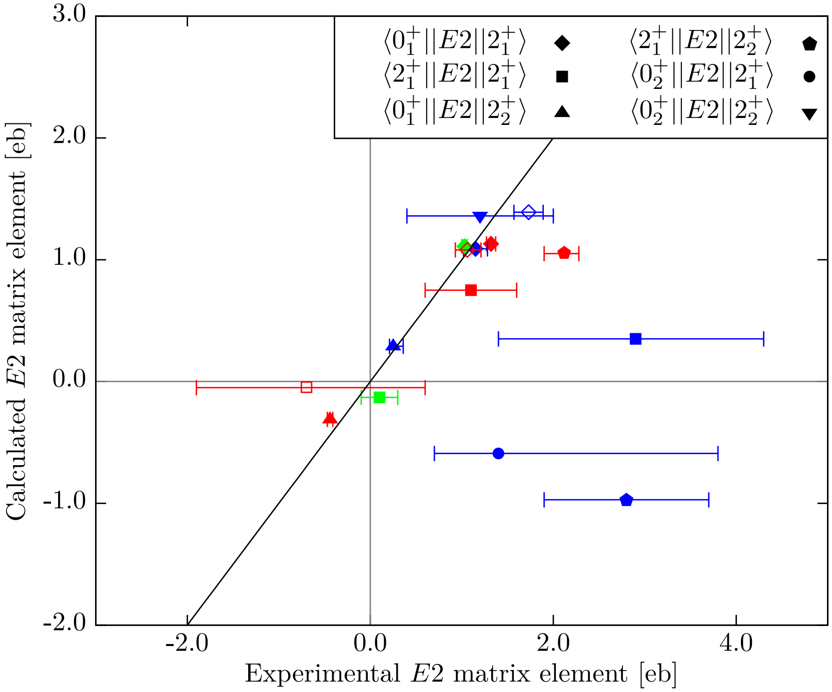

Figure 5.17: The measured $E2$ matrix elements determined in this work, compared to those extracted from two-level mixing calculations for ^{194}Po (open blue), ^{196}Po (full red), ^{198}Po (full blue), ^{200}Po (full green), ^{202}Po (open red). The measured 1σ error bars are shown. In ^{196}Po solution 2 (see Table 4.18) is adopted. This solution corresponds to a total χ^2 value of 101.

describing the deformed structure in the polonium isotopes are comparable to those extracted in the two-state mixing approach in the mercury isotopes for the weakly deformed oblate structure, where the extracted unperturbed transitional and diagonal $E2$ matrix elements of the weakly-deformed structure are 1.2 eb and 1.8 eb respectively [99]. This supports the interpretation that a weakly deformed, oblate structure is intruding in the low-lying energy levels of the neutron-deficient polonium isotopes. The characteristics of this weakly-deformed oblate structure seem to be related to those of the oblate structure in the mercury isotopes, that mirror the polonium isotopes with respect to $Z = 82$.

An alternative fitting procedure was applied where the signs of the transitional $E2$ matrix elements were not taken into account in the fit. The χ^2 value

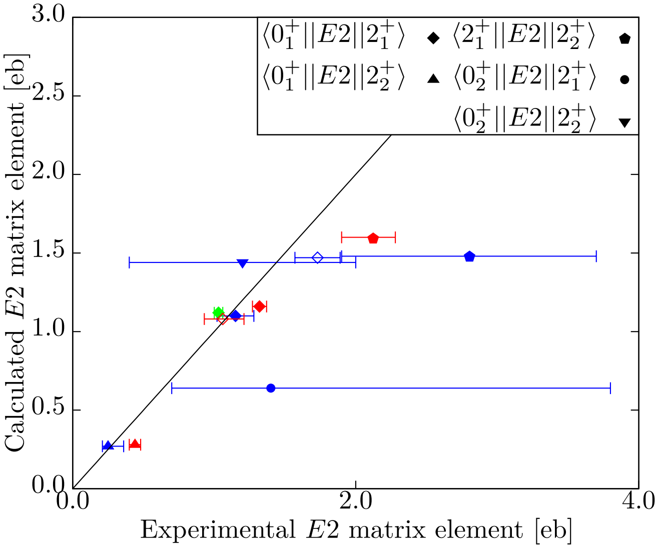

Figure 5.18: The magnitude of the measured $E2$ matrix elements determined in this work, compared to those extracted from two-level mixing calculations for ^{194}Po (open blue), ^{196}Po (full red), ^{198}Po (full blue), ^{200}Po (full green), ^{202}Po (open red). The measured 1σ error bars are shown. In ^{196}Po solution 1 (see Table 4.18) is adopted. This solution corresponds to a total χ^2 value of 48. The diagonal matrix elements are not taken into account in this fit.

was calculated using the magnitude of the experimental and calculated matrix elements. The diagonal matrix elements were also excluded from the fit, as the magnitude of the diagonal matrix element has no physical meaning. In this case, the best fit was found for solution 1 in ^{196}Po ($\chi^2 = 48$, compared to $\chi^2 = 58$ for solution 2). A comparison of the calculated and observed magnitudes of the transitional $E2$ matrix elements is shown in Figure 5.18. The only unperturbed matrix element that differs from the solution where the signs and the diagonal matrix elements are taken into account, is $\langle 2_I^+||E2||2_I^+\rangle = -1.3\,\text{eb}$.

It is clear from Figure 5.17 that the fit result is influenced greatly by the matrix elements with small uncertainties. Matrix elements with larger uncertainties, like the matrix elements coupling the higher-lying states in ^{198}Po, constrain the fit much less. Therefore, in a final fitting procedure the χ^2 value was redefined as:

$$\chi^2 = \sum_i \left(\text{ME}_{\text{calc},i} - \text{ME}_{\text{exp},i}\right)^2 , \tag{5.26}$$

hereby eliminating the influence of the experimental uncertainties. This method

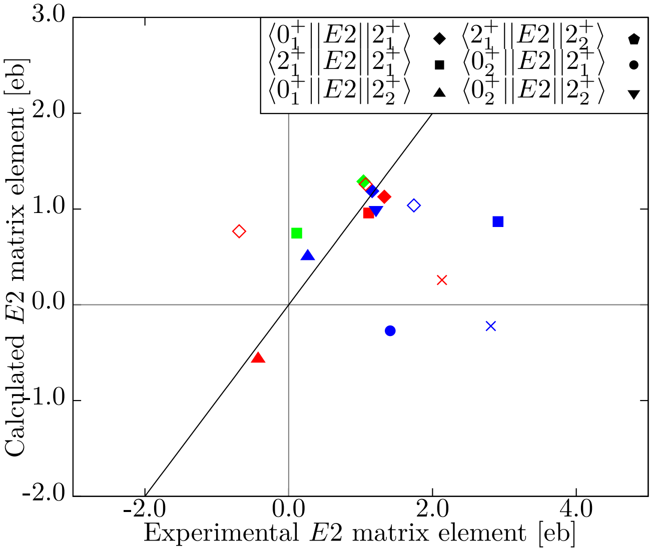

Figure 5.19: The measured $E2$ matrix elements determined in this work, compared to those extracted from two-level mixing calculations for ^{194}Po (open blue), ^{196}Po (full red), ^{198}Po (full blue), ^{200}Po (full green), ^{202}Po (open red). The uncertainties on the experimental $E2$ matrix elements are not given in the figure and were not taken into account in the fitting procedure. In ^{196}Po solution 2 (see Table 4.18) is adopted. This solution corresponds to a total χ^2 value of 23.

changes the unperturbed matrix elements, yielding the best fit for solution 2 in ^{196}Po ($\chi^2 = 23$, compared to $\chi^2 = 26$ for solution 1):

$$\begin{cases} \langle 0_I^+||E2||2_I^+\rangle = 1.3\,\text{eb} \\ \langle 0_{II}^+||E2||2_{II}^+\rangle = 1.0\,\text{eb} \\ \langle 2_I^+||E2||2_I^+\rangle = 0.7\,\text{eb} \\ \langle 2_{II}^+||E2||2_{II}^+\rangle = 1.2\,\text{eb}. \end{cases} \tag{5.27}$$

A comparison of the measured and calculated matrix elements for this final fitting procedure is shown in Figure 5.19, where the uncertainty on the experimental matrix elements is only shown for information. This solution for the unmixed matrix elements seems less physical than the solution in equation 5.25.

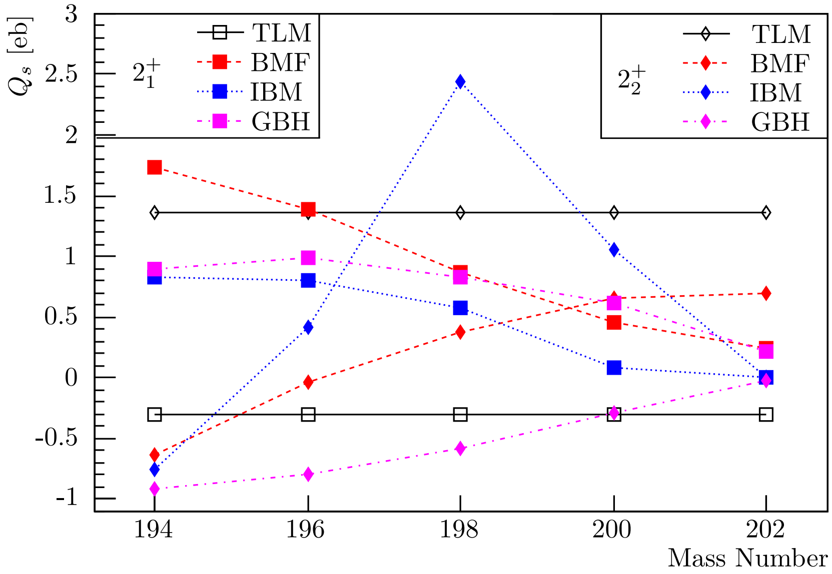

Figure 5.20: Spectroscopic quadrupole moment of the 2_1^+ (squares) and 2_2^+ (diamonds) states as a function of mass number of the polonium isotopes. The results in black are the unperturbed spectroscopic quadrupole moments that are obtained with the two-state-mixing approach. The values in red, blue and pink represent the BMF, IBM and GBH results respectively.

Comparison of two-level-mixing results to theory

From the unperturbed diagonal matrix elements (see equation 5.25) $\langle 2_I^+||E2||2_I^+\rangle = -0.4\,\text{eb}$ and $\langle 2_{II}^+||E2||2_{II}^+\rangle = 1.8\,\text{eb}$, values for the unmixed spectroscopic quadrupole moments of the 2_1^+ and 2_2^+ states can be deduced. Figure 5.20 compares these “pure” values for Q_s with the spectroscopic quadrupole moments calculated with the three different nuclear models (BMF, IBM and GBH). The values for the two unperturbed quadrupole moments, extracted with the two-state-mixing model, point to the presence of a spherical structure and a weakly-deformed oblate structure. A similar figure was constructed for the mercury isotopes, following the two-state-mixing calculations [78]. In that case, the unperturbed Q_s represent limits; the values for Q_s, determined by the theoretical models, do not cross these limits. In the polonium isotopes, the situation is less clear. The theoretical results for Q_s of the 2_2^+ state differ a lot between the three models. Next to that, the theoretical Q_s values exceed the unperturbed values for multiple isotopes. The presence of a third 2^+ state, part of a third structure, can not be excluded. Studies of the more neutron-deficient polonium isotopes, closer to mid-shell, might shed more light on this (see also Chapter 6).

6 | Conclusion and outlook

Summary

The neutron-deficient polonium isotopes are situated in the light-lead region of the nuclear chart, where complex nuclear physics properties have been observed. Shape coexistence, whereby two or more distinct types of deformation occur at similar excitation energy in a nucleus, has been identified both experimentally as well as theoretically in the neighboring Pb and Hg isotopes. Furthermore, the co-existing structures are found to mix with each other. A recent Coulomb-excitation study of the neutron-deficient even-even $^{182-188}$Hg isotopes quantified the mixing between a weakly-deformed oblate-like band and a more-deformed prolate-like band in the neutron-deficient mercury isotopes [99]. The neutron-deficient $^{196-202}$Po isotopes establish a transitional region between two-particle like behavior for the heavier isotopes and interplay between normal and intruder structures for the lighter isotopes.

Coulomb excitation is the process in which the collision between a projectile and a target nucleus leads to the excitation of one of the collision partners. When the energy of the incoming projectile beam is below the so-called “safe” value, the reaction is purely electromagnetic. The cross section for the Coulomb-excitation process is determined by the reduced matrix elements coupling the populated low-lying states in the excited nucleus. The technique of Coulomb excitation is powerful, as it allows to extract information about the collectivity and deformation in a nucleus in a model-independent way.

With the aim of studying the deformation and possible mixing between co-existing structures in the neutron-deficient ^{196,198,200,202}Po isotopes, two Coulomb-excitation campaigns were performed at the REX-ISOLDE facility in CERN. Post-accelerated beams with energies of 2.85 MeV per nucleon were produced and made to collide with a 2.0 mg/cm^2 thick ^{104}Pd and ^{94}Mo target in the collision chamber. Beam intensities of $2.3(2) \times 10^4$ pps to $2.54(17) \times 10^5$

pps were observed at the Miniball detection setup, that consists of a segmented double-sided silicon strip detector to detect the scattered particles and a position-sensitive high-purity germanium detector array to detect the de-excitation γ rays. The heavier ^{198,200,202}Po beams were almost isobarically pure with purities exceeding 95 %, while the lightest ^{196}Po beam suffered from a $\approx 40\,\%$ ^{196}Tl contaminant. The isobaric impurity of the ^{196}Po beam was dealt with by employing the laser ON/OFF mode to disentangle the different components of the beam.

Coulomb-excitation events were selected from the background by applying conditions related to the timing and kinematic properties of the events. The background-subtracted and Doppler-corrected γ-ray spectra showed the population of the 2_1^+ state in all isotopes. Next to that, in ^{196,198}Po multi-step Coulomb excitation was observed to populate the 4_1^+, 0_2^+ and 2_2^+ states, albeit with limited statistics. The relatively large uncertainties on the de-excitation yields related to the 0_2^+ and 2_2^+ states was due to the indirect observation of the $E0$ transitions between the 0_2^+ and 0_1^+ states and the 2_2^+ and 2_1^+ states through characteristic polonium X rays.

The least-squares Coulomb-excitation analysis code GOSIA was used to extract the reduced matrix elements coupling the populated states in the polonium isotopes. In the isotopes ^{200,202}Po the transitional and diagonal matrix element of the 2_1^+ state were determined using a two-dimensional χ^2-surface analysis. A combined approach between standard GOSIA and GOSIA2 was performed to extract a set of reduced matrix elements in ^{196,198}Po. In ^{196}Po, two solutions with different relative sign combinations were identified. No model-independent distinction between the two solutions was possible.

The experimental results have been compared to the results from the measurement of mean-square charge radii in the polonium isotopes, confirming the onset of deformation from ^{196}Po, going towards the lighter Po isotopes. Three different model descriptions have been used to compare to the data. Calculations with the beyond-mean-field model, the interacting boson model and the general Bohr Hamiltonian model show partial agreement with the experimental data. Finally, calculations with a phenomenological two-level mixing model hint towards the mixing of a more spherical structure with a weakly-deformed rotational structure. Overall the comparison to theory would benefit from an increase in experimental sensitivity.

Outlook

The current body of experimental information regarding shape coexistence in the polonium isotopes is relatively scarce, compared to the well-studied neighboring mercury and lead isotopes. Therefore, interesting possibilities related to future Coulomb-excitation experiments of the neutron-deficient polonium isotopes exist. First, one could aim to produce even more neutron-deficient polonium beams and try to reach isotopes closer to neutron mid-shell ($N = 104$). Polonium beams with mass below $A = 196$ would suffer from lower beam intensities, combined with an increasing amount of isobaric thallium contamination. One possible solution for this problem is the Laser Ion Source and Trap (LIST) technique at ISOLDE that suppresses isobaric contamination with a factor of 1000 [102]. As a drawback, the polonium beam intensity also drops with a factor of ≈ 20.

Next to that, the precision of Coulomb-excitation experiments with the presently available beams can be improved. Increased sensitivity to higher-order effects could be reached in Coulomb-excitation experiments with higher beam energies at HIE-ISOLDE where post-accelerated beams with energies up to 10 MeV per nucleon will be produced [103, 104]. Experiments with higher beam energies will result in higher cross section for multi-step Coulomb excitation, providing more information about e.g. reduced $E2$ transition probabilities, quadrupole moments and ground state deformations in these isotopes. However, the data set will also present a challenge as the data analysis and interpretation will be complicated by additional couplings that need to be taken into account.

For future experiments the electron detector SPEDE, which is constructed jointly by the universities of Liverpool and Jyväskylä, will provide a direct way of detecting $E0$ transitions [105]. This might improve the uncertainty on the observed $E0$ decay of the populated states. Finally, additional spectroscopic information on the neutron-deficient polonium isotopes is crucial as input for the GOSIA calculations as it would help to constrain the fit. β-decay studies of the more neutron-deficient At isotopes could provide information on branching ratios and conversion coefficients. However, the β branch in the decay of the At isotopes decreases with decreasing mass number. Further, lifetime measurements of the heavier isotopes with mass $A > 196$ would provide valuable information about the transition probabilities.

Bibliography

[1] D. J. Rowe and J. L. Wood, *Fundamentals of Nuclear Models, Foundational Models*, World Scientific, 2010.

[2] R. F. Casten, *Nuclear Structure from a Simple Perspective*, Oxford University Press, 2000.

[3] K. L. G. Heyde, *The Nuclear Shell Model*, Springer-Verlag, 1990.

[4] E. Epelbaum, H.-W. Hammer, and U.-G. Meissner, *Rev. Mod. Phys.* **81**, 1773 (2008).

[5] S. K. Bogner, T. T. S. Kuo, and A. Schwenk, *Phys. Rep.* **386**, 1 (2003).

[6] S. C. Pieper, *Eur. Phys. J. A* **13**, 75 (2001).

[7] E. Caurier, J. Menéndez, F. Nowacki, and A. Poves, *Phys. Rev. C* **75**, 054317 (2007).

[8] A. Poves, *Nucl. Phys. A* **731**, 339 (2004).

[9] A. Bohr, *Rev. Mod. Phys.* **48**, 365 (1976).

[10] B. Mottelson, *Rev. Mod. Phys.* **48** (1976).

[11] S. G. Nilsson, *Dan. Mat. Fys. Medd.* **29** (1955).

[12] P. J. Brussaard and P. W. M. Glaudemans, *Shell-Model applications in nuclear spectroscopy*, North-Holland Publishing Company, 1977.

[13] P. E. Garrett and J. L. Wood, *J. Phys. G Nucl. Part. Phys.* **37**, 064028 (2010).

[14] P. Van Isacker and K. Heyde, *Scholarpedia* **9**, 31279 (2014).

[15] D. J. Rowe, *Nuclear collective motion: Models and theory*, Hackensack, NJ: World Scientific, 2010.

[16] A. Bohr and B. R. Mottelson, *Nuclear Structure: Volume 2, Nuclear deformations*, W.A. Benjamin, 1969.

[17] V. Hellemans, *Shape coexistence and critical phenomena in atomic nuclei*, PhD thesis, Universiteit Gent, 2008.

[18] G. Ulm et al., *Zeitschrift für Phys. A* **325**, 247 (1986).

[19] A. N. Andreyev et al., *Nature* **405**, 430 (2000).

[20] K. Heyde and J. L. Wood, *Rev. Mod. Phys.* **83**, 1467 (2011).

[21] A. Maj et al., *Nucl. Phys. A* **509**, 413 (1990).

[22] D. Alber, R. Alfier, C. E. Bach, and D. B. Fossan, *Zeitschrift für Phys. A* **339**, 225 (1991).

[23] M. Lach et al., *Zeitschrift für Phys. A* **350**, 207 (1994).

[24] L. A. Bernstein et al., *Phys. Rev. C* **52**, 621 (1995).

[25] W. Younes et al., *Phys. Rev. C* **52**, R1723 (1995).

[26] N. Fotiades, W. Younes, and J. A. Cizewski, *Phys. Rev. C* **55**, 1724 (1997).

[27] N. Fotiades et al., *Phys. Rev. C* **56**, 723 (1997).

[28] K. Helariutta, T. Enqvist, and P. Jones, *Phys. Rev. C* **54**, 2799 (1996).

[29] K. Helariutta et al., *Eur. Phys. A* **6**, 289 (1999).

[30] R. Julin, K. Helariutta, and M. Muikku, *J. Phys. G Nucl. Part. Phys.* **27**, 109 (2001).

[31] A. N. Andreyev et al., *Phys. Rev. C* **66**, 014313 (2002).

[32] K. Van de Vel et al., *Eur. Phys. J. A* **17**, 167 (2003).

[33] D. R. Wiseman et al., *Eur. Phys. J. A* **34**, 275 (2007).

[34] J. Wauters et al., *Zeitschrift für Phys. A* **344**, 29 (1992).

[35] J. Wauters, P. Dendooven, M. Huyse, G. Reusen, and P. Van Duppen, *Phys. Rev. C* **47**, 1447 (1993).

[36] N. Bijnens et al., *Phys. Rev. Lett.* **75**, 4571 (1995).

[37] N. Bijnens et al., *Phys. Rev. C* **58**, 754 (1998).

[38] R. G. Allatt et al., *Phys. Lett. B* **437**, 29 (1998).

[39] A. N. Andreyev et al., *J. Phys. G Nucl. Part. Phys.* **25**, 835 (1999).

[40] A. N. Andreyev, M. Huyse, and P. Van Duppen, *Phys. Rev. Lett.* **82**, 1819 (1999).

[41] P. Van Duppen and M. Huyse, *Hyperfine Interact.* **129**, 149 (2000).

[42] K. Van de Vel et al., *Phys. Rev. C* **68**, 054311 (2003).

[43] K. Van de Vel et al., *Eur. Phys. J. A* **24**, 57 (2005).

[44] A. N. Andreyev et al., *Phys. Rev. C* **73**, 044324 (2006).

[45] A. Y. Deo et al., *Phys. Rev. C* **81**, 024322 (2010).

[46] T. Grahn et al., *Phys. Rev. Lett.* **97**, 062501 (2006).

[47] T. Grahn et al., *Phys. Rev. C* **80**, 014323 (2009).

[48] C. Ellegaard et al., *Nucl. Phys. A* **206**, 83 (1973).

[49] T. E. Cocolios et al., *Phys. Rev. Lett.* **106**, 052503 (2011).

[50] M. D. Seliverstov et al., *Phys. Lett. B* **719**, 362 (2013).

[51] W. Borchers et al., *Hyperfine Interactions* **34**, 25 (1987).

[52] T. Hilberath et al., *Zeitschrift für Phys. A* **342**, 1 (1992).

[53] F. Le Blanc, D. Lunney, J. Obert, and J. Oms, *Phys. Rev. C* **60**, 054310 (1999).

[54] J. A. Cizewski and W. Younes, *Zeitschrift für Phys. A* **358**, 133 (1997).

[55] W. Younes and J. Cizewski, *Phys. Rev. C* **55**, 1218 (1997).

[56] A. M. Oros et al., *Nucl. Phys. A* **645**, 107 (1999).

[57] J. Ressler et al., *Phys. Rev. C* **69**, 034317 (2004).

[58] C. De Coster, B. Decroix, and K. Heyde, *Phys. Rev. C* **61**, 067306 (2000).

[59] F. May, V. Pashkevich, and S. Frauendorf, *Phys. Lett. B* **68**, 113 (1977).

[60] Y. Shi, F. R. Xu, H. L. Liu, and P. M. Walker, *Phys. Rev. C* **82**, 044314 (2010).

[61] N. A. Smirnova, P.-H. Heenen, and G. Neyens, *Phys. Lett. B* **569**, 151 (2003).

[62] J. M. Yao, M. Bender, and P.-H. Heenen, *Phys. Rev. C* **87**, 034322 (2013).

[63] K. Alder, A. Bohr, T. Huus, B. Mottelson, and A. Winther, *Rev. Mod. Phys.* **28**, 453 (1956).

[64] K. Alder and A. Winther, *Electromagnetic excitation, Theory of Coulomb excitation with heavy ions*, North-Holland Publishing Company, American Elsevier Publishing Company, 1975.

[65] D. Cline, *Annu. Rev. Nucl. Part. Sci.* **36**, 683 (1986).

[66] S. Wong, *Introductory Nuclear Physics*, Wiley-VCH Verlag GmbH, Weinheim, Germany, second edi edition, 1998.

[67] J. Van de Walle, *Coulomb excitation of neutron rich Zn isotopes*, PhD thesis, KU Leuven, 2006.

[68] E. Segrè, *Nuclei and Particles, An Introduction to Nuclear and Subnuclear Physics*, The Benjamin/Cummings Publishing Company, Inc., second edi edition, 1977.

[69] C. Y. Wu et al., *Nucl. Phys. A* **607**, 178 (1996).

[70] T. Czosnyka, D. Cline, and C. Y. Wu, *Bull. Am. Phys. Soc.* **28**, 745 (1982).

[71] T. Czosnyka, D. Cline, and C. Y. Wu, http://www.slcj.uw.edu.pl/gosia.

[72] L. P. Gaffney et al., *Eur. Phys. J. A* , to be published (2015).

[73] D. Habs et al., *Nucl. Instruments Methods Phys. Res. B* **139**, 128 (1998).

[74] B. A. Marsh et al., *Nucl. Instruments Methods Phys. Res. B* **317**, 550 (2013).

[75] A. Kramida, Y. Ralchenko, J. Raeder, and NIST ASD Team (2013), NIST Atomic Spectra Database (ver. 5.1), 2013.

[76] N. Warr et al., *Eur. Phys. J. A* **49**, 40 (2013).

[77] N. Bree, *Shape coexistence in the neutron-deficient mercury isotopes studied through Coulomb excitation*, PhD thesis, KU Leuven, 2014.

[78] K. Wrzosek-Lipska et al., *Phys. Rev. C* , in preparation (2015).

[79] M. D. Seliverstov et al., *Phys. Rev. C* **89**, 034323 (2014).

[80] F. Iachello and A. Arima, *The Interacting Boson Model*, Cambridge University Press, 1987.

[81] J. Egido and L. Robledo, 10 Angular Momentum Projection and Quadrupole Correlations Effects in Atomic Nuclei, in *Extended Density Functionals in Nuclear Structure Physics*, edited by G. Lalazissis, P. Ring, and D. Vretenar, volume 641 of *Lecture Notes in Physics*, pp. 269–302, Springer Berlin Heidelberg, 2004.

[82] M. Bender, *Eur. Phys. J. Spec. Top.* **156**, 217 (2008).

[83] M. Bender and P.-H. Heenen, *Phys. Rev. C* **78**, 024309 (2008).

[84] L. Próchniak and S. G. Rohoziński, *J. Phys. G Nucl. Part. Phys.* **36**, 123101 (2009).

[85] A. Arima and F. Iachello, *Ann. Phys. (N.Y).* **99**, 253 (1976).

[86] A. Arima and F. Iachello, *Ann. Phys. (N.Y).* **111**, 201 (1978).

[87] A. Arima and F. Iachello, *Ann. Phys. (N.Y).* **123**, 468 (1979).

[88] J. E. García-Ramos and K. Heyde, *Phys. Rev. C* **89**, 014306 (2014).

[89] J. E. García-Ramos, V. Hellemans, and K. Heyde, *Phys. Rev. C* **84**, 014331 (2011).

[90] K. Heyde, C. D. Coster, J. Jolie, and J. L. Wood, *Phys. Rev. C* **46** (1992).

[91] K. Heyde, P. Van Isacker, and J. L. Wood, *Phys. Rev. C* **49** (1994).

[92] T. Otsuka, A. Arima, F. Iachello, and I. Talmi, *Phys. Lett. B* **76**, 139 (1978).

[93] J. E. García-Ramos and K. Heyde, *Private Communication* .

[94] L. Próchniak, *Private Communication* .

[95] E. Otten, Nuclear Radii and Moments of Unstable Isotopes, in *Treatise on Heavy Ion Science*, edited by D. Bromley, pp. 517–638, Springer US, 1989.

[96] K. Kumar, *Phys. Rev. Lett.* **28**, 249 (1972).

[97] K. Wrzosek-Lipska et al., *Phys. Rev. C* **86**, 064305 (2012).

[98] L. P. Gaffney et al., *Phys. Rev. C* **89**, 024307 (2014).

[99] N. Bree et al., *Phys. Rev. Lett.* **112**, 162701 (2014).

[100] M. A. J. Mariscotti, G. Scharff-Goldhaber, and B. Buck, *Phys. Rev.* **178**, 1864 (1969).

[101] P. Van Duppen, M. Huyse, and J. L. Wood, *J. Phys. G* **16**, 441 (1990).

[102] D. A. Fink et al., *Nucl. Instruments Methods Phys. Res. B* **317**, 417 (2013).

[103] M. Lindroos, P. A. Butler, M. Huyse, and K. Riisager, *Nucl. Instruments Methods Phys. Res. B* **266**, 4687 (2008).

[104] R. Catherall et al., *Nucl. Instruments Methods Phys. Res. Sect. B* **317**, 204 (2013).

[105] J. Konki et al., *EPJ Web Conf.* **63**, 01019 (2013).

FACULTY OF SCIENCE
DEPARTMENT OF PHYSICS AND ASTRONOMY
INSTITUTE FOR NUCLEAR AND RADIATION PHYSICS
Celestijnenlaan 200D bus 2418
B-3001 Heverlee